The Synthesis and Characterisation of High Performance Electrode Materials for Li-ion Batteries

Steve Clark
Lincoln College

A thesis submitted for the degree of Doctor of Philosophy

Department of Materials, University of Oxford

Abstract

The Synthesis and Characterisation of High Performance Electrode Materials for Li-ion Batteries

Steve Clark
Lincoln College & Department of Materials, University of Oxford

With the worlds demand for electricity constantly growing, energy storage technologies, and lithium-ion batteries in particular, are becoming increasingly important. One of the most significant issues concerning Li-ion batteries is that of safety. Graphite is the most commonly used anode material, however, due to its very low operating voltage vs Li^+/Li^0, reactive lithium can plate on the electrode surface, this is especially an issue for large batteries for use in electric vehicles. It would be useful to have an anode that operates at a higher voltage than graphite, but not at such a high voltage as to limit the overall potential of the cell.

To this end the focus of this thesis is the development of an anode material that operate at 1 V vs Li^+/Li^0. The lithium metal sulphides have previously demonstrated that they reversibly intercalate lithium at ~ 1 V, but the reported performance is poor. Here $LiVS_2$ is reinvestigated and optimised to display significantly improved electrochemical properties. At a rate of 100 mAg^{-1} a reversible capacity of over 200 $mAhg^{-1}$ is achieved compared to less than 150 $mAhg^{-1}$ previously reported, capacity retention is also considerably enhanced. $LiVS_2$ deintercalates Li^+ at the high voltage of 1.3 V, therefore attention is turned to $LiV_{0.5}Ti_{0.5}S_2$ which intercalates Li^+ at 0.9 V and deintercalation occurs at 0.9 V. The performance of $LiV_{0.5}Ti_{0.5}S_2$ is optimised and the electrochemical process by which $LiV_{0.5}Ti_{0.5}S_2$ operates is fully investigated. $LiV_{0.5}Ti_{0.5}S_2$ displays a low irreversible capacity loss, low polarisation, good rate capabilities and good capacity retention.

As $LiV_{0.5}Ti_{0.5}S_2$ operates at ~ 1 V higher than graphite it is important to match it with a high voltage cathode so the overall potential of the cell is not significantly reduced. The lithium rich mixed metal oxides have been the focus of much research over the last 15 years and here they are investigated using a resorcinol-formaldehyde gel synthesis. $0.5Li_2MnO_3{:}0.5LiNi_{0.5}Mn_{0.5}O_2$ and $0.6Li_2MnO_3{:}0.4Li(Ni_{1/3}Mn_{1/3}Co_{1/3})O_2$ are both successfully synthesised and demonstrate excellent electrochemical performance. The specific capacities and capacity retention of both materials at a rate of 150 mAg^{-1} are excellent and better than virtually all previously reported materials of this type. Neutron diffraction was carried out on both materials to monitor structural changes on cycling.

Finally, $LiV_{0.5}Ti_{0.5}S_2$ and the lithium-rich mixed metal oxides are combined in full 'rocking-chair' lithium-ion cells to successfully show that both materials can be used in practical lithium-ion batteries.

Statement of Originality and Authorship

I declare the content of the D.Phil thesis titled "The synthesis and characterisation of high performance electrode materials for Li-ion batteries" is my own work except for the following portions:

- The neutron diffraction data of $LiVS_2$ and $LiV_{0.5}Ti_{0.5}S_2$, in sections 3.4 and 4.4.2 respectively, was carried out on the Polaris beam line at the ISIS neutron source in Didcot, UK in collaboration with Dr A. Robert Armstrong at the University of St Andrews. The data was collected by both of us while I prepared the samples, carried out the Rietveld structural refinements and interpreted the data.

- The X-ray absorption near edge spectroscopy experiment outlined in section 4.6.3 was carried out at the Diamond Light Source in Didcot, UK in collaboration with Professor Alan Chadwick and co-workers at the University of Kent. They collected and processed the data, while I prepared the samples and interpreted the processed data.

- The neutron diffraction data for $0.5Li_2MnO_3{:}0.5LiNi_{0.5}Mn_{0.5}O_2$ and $0.6Li_2MnO_3{:}0.4Li(Ni_{1/3}Mn_{1/3}Co_{1/3})O_2$, presented in section 5.6, was carried out on the Polaris and Gem beam lines at the ISIS neutron source in Didcot, UK in collaboration with Dr A. Robert Armstrong at the University of St Andrews. I prepared the samples and the data was collected by both of us. Dr A. Robert Armstrong carried out the Rietveld structural refinements on the samples, while the interpretation of the refinements is my own.

Steve Clark

Acknowledgements

I would like to thank the following:

Firstly, Professor Peter Bruce for all of his assistance and guidance over the course of the last 4 years. Without his limitless enthusiasm and patience the work presented in this thesis would not have been possible.

Dr Rob Armstrong for his supervision and help across multiple topics. In particular I would like to thank him for his support in carrying out neutron diffraction experiments and Rietveld refinements.

Dr Paul Adamson and Dr Da Wang for their advice and discussions on the sulphide anode portions of this work.

Dr Mathew Roberts and Dr Nicholas Drewett for their insights and experience on the lithium rich mixed metal oxide cathode section of this work.

All of the other members of the Bruce group for their support and friendship over the last 4 years.

Professor Alan Chadwick and co-workers for carrying out the XANES experiment in Chapter 4.

All of the beam line scientists at ISIS for their assistance in carrying out neutron diffraction experiments.

Table of Contents

Chapter 1: Introduction

1.1 The Need for Energy Storage

The worlds demand for electricity is constantly growing and is predicted to increase by 50% from 2015 to 2040[1], simultaneously, the importance of tackling man-made climate change is now irrefutable. As a result there is increasing focus on clean renewable energy sources. While solar, wind and wave energies are important, they are inherently variable and a range of energy storage technologies will be required for these renewable energy sources to reach their full potential. Within the umbrella of energy storage technologies, batteries are likely to play a vital role.

Batteries may be divided into two classes. Primary batteries convert chemical energy to electrical energy and when they are fully discharged cannot be recharged. Secondary batteries on the other hand, store electricity reversibly and can therefore be recharged.

Lithium-ion batteries are secondary batteries and have a higher specific energy (energy per unit weight) and energy density (energy per unit volume) than other commercial batteries. As a result they have come to dominate the market of portable electronic devices such as mobile phones and laptops. Additionally, lithium-ion batteries are the technology of choice for electric vehicles and, along with redox flow batteries, lithium-ion batteries are of interest for use for grid scale storage. While lithium-ion batteries have advantages compared with other battery technologies, improvements are still required to meet the needs of electric vehicles and for storing energy on the grid. The issue of safety is particularly important and is a major motivation behind this project.

1.2 Principles of lithium-ion batteries

Lithium-ion batteries were first investigated in the 1970s[2], however, it was not until 1991 that the first commercial lithium-ion battery was produced[3]. Rechargeable lithium-ion batteries rely on the reversibility of lithium insertion. During cycling Li-ions move between two different electrodes, this process is accompanied by a flow of electrons through an external circuit. During discharge, Li-ions are extracted from the negative electrode (anode) and move through a Li-ion conducting electrolyte. They then insert into the positive electrode (cathode). Simultaneously, electrons travel through an external circuit producing a current. When an external current is applied to the cell, lithium ions move from the cathode back to the anode, therefore charging the cell and storing energy. When insertion/deinsertion takes place with respect to a layered material it is termed intercalation/deintercalation.

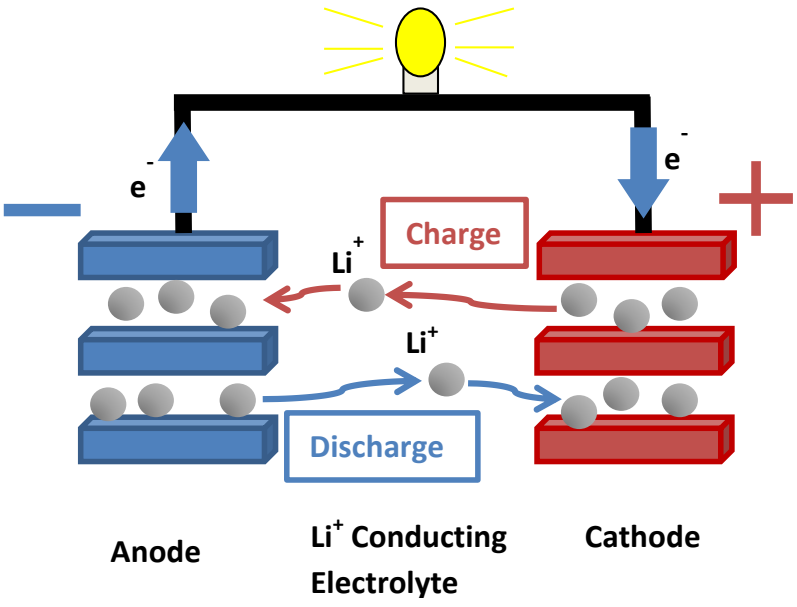

Figure 1.1: Schematic of a lithium-ion battery.

The cathode, anode and electrolyte can all be changed, and there is extensive research in all three areas. This project is concerned with the development of both anode and cathode

materials. An overview of commonly used anode materials is given in Section 1.3 and cathode materials are discussed in Section 1.4. A very brief discussion of electrolytes is included below.

1.2.1 Electrolytes for Li-ion batteries

The two prerequisites for an electrolyte are that it must be a good ionic conductor (> 1 mS cm^{-1}), in order to facilitate the passage of Li^+ from one electrode to another, and also must be an electronic insulator, to force electrons to flow through the external circuit. Other important qualities include[4]:

- Having a wide electrochemical stability window, ideally between 0 – 5 V vs Li^+/Li^0
- Chemically and thermally stable (up to at least 90 ^oC)
- Non-reactive with other cell components
- Low cost
- Safe – low toxicity and flammability

The most commonly used electrolytes are liquid organic electrolytes and these were used for all of the experiments in this thesis. They are made up of a lithium salt (e.g. lithium hexafluorophosphate ($LiPF_6$), lithium perchlorate ($LiClO_4$) or lithium tetrafluoroborate ($LiBF_4$)) dissolved in either a pure or mixture of organic solvents. One of the most widely used solvents, due to its stability against oxidation up to ~ 5 V vs Li^+/Li^0, is propylene carbonate (PC)[5]. However, pure PC electrolytes lead to co-intercalation of solvated lithium at graphite anodes, leading to the destruction of the electrode[6,7]. By contrast ethylene carbonate (EC) is reduced more quickly than PC and forms a solid electrolyte interphase (SEI) layer on the surface of the anode[8], preventing any further solvent co-intercalation. Further discussion of SEI layer formation can be found in 1.3.2. As EC is solid at room temperature it is necessary to blend it with lower melting point solvents such as diethyl carbonate (DEC) and dimethyl carbonate (DMC). Details of the specific electrolytes used can be found in the relevant sections.

1.3 Anode materials for Li-ion batteries

1.3.1 Requirements for a suitable anode

The most obvious candidate for the negative electrode in rechargeable lithium batteries is lithium metal itself. It has a low potential of -3.04 V vs the standard hydrogen electrode (SHE)[2] and a potential of 0 vs Li^+/Li^0. It also has a very low molecular weight of 6.941 g mol^{-1} which results in an excellent theoretical specific capacity of 3860 $mAhg^{-1}$. Due to these reasons initial research in lithium ion batteries in the 1970s used lithium as the anode[2]. Unfortunately, lithium metal anodes have problems with dendrites (finger-like growths of lithium) forming on the surface of the electrode[9]. Dendrites grow upon continuous charging/discharging and can break the separator that divides the anode from the cathode, this leads to the cell failing and in extreme circumstances can result in fire. While this is not an issue when using small amounts of lithium in half-cells in the laboratory it can cause significant hazards in real world applications, therefore it became necessary to investigate other potential anode materials.

The main requirements for anode materials are[10]:

- React with lithium at low voltages vs Li^+/Li^0 to maximise the overall voltage of the battery
- Be able to insert/extract (or otherwise react with see 1.3.3.3/1.3.3.4) lithium in a reversible way that minimises structural change and to do so with fast kinetics
- Have good electrical conductivity to allow fast electrochemical reactions
- Be low cost
- Be non-toxic and environmentally benign
- Easily and reproducibly synthesised with the desired morphology
- Easily fabricated into electrodes

As will be seen in the following sections, many of the most common anode materials struggle to fulfil all of these criteria.

1.3.2 Solid Electrolyte Interphase (SEI) layer formation on anodes

Solid electrolyte interphases were first observed with lithium metal[11] and subsequently with graphite electrodes[12]. SEI layers have since been observed to occur, to at least some degree, on any anode material with all organic electrolytes below 1.0 V vs. lithium[12]. During initial lithium intercalation the organic solvent reductively decomposes on the graphite surface to form a stable surface film which is an electronic insulator but a Li^+ conductor. The formation of the SEI layer results in an irreversible capacity loss on the first cycle as charge is consumed in side reactions that induce the formation of the layer. The amount of irreversible capacity loss is dependent on the thickness of the SEI layer, which in turn is dependent on the operating voltage of the anode. The lower the voltage of the anode is discharged to the larger the irreversible capacity loss. The formation of the SEI layer passivates the surface of the anode and prevents the further reaction and decomposition of solvent molecules[12]. This ensures that the only process carried out on the surface is Li-ion migration. While the formation of the SEI layer is vital for the functioning of organic electrolyte based Li-ion batteries at low voltages, its formation also leads irreversible capacity loss and capacity fade, it is therefore beneficial to form the thinnest SEI layer possible.

1.3.3 Overview of anode materials

1.3.3.1 Graphite and other carbon based anodes

Graphite is by far the most commonly used anode material in lithium ion batteries, principally due to being non-toxic, low cost and operating at a very low voltage of 0.1 V vs Li^+/Li[013-16]. It was first studied in the 1980s and has been used in commercial lithium ion batteries since the

early 1990s. When the battery is charged Li-ions intercalate between layers of graphite and this is reversed during discharge. An additional strength of graphite as an anode material is that this process is very reversible and there is little structural change in the intercalation/deintercalation process. The intercalation/deintercalation can be shown with the following equation:

$$C_6 + Li^+ + e^- \rightleftharpoons LiC_6$$

The intercalation/deintercalation process happens at a very low voltage of approximately 0.1 V vs Li^+/Li^0. As one Li^+ is inserted for every 6 carbon atoms, the theoretical capacity of graphite is 372 $mAhg^{-1}$. The density of graphite varies depending on the sort of graphite used which results in reversible volumetric capacities of 600 – 700 $mAhcm^{-3}$. The low operating voltage results in a maximisation of the battery potential but also leads to an important negative consequence. At voltages so close to 0 V vs Li^+/Li^0 lithium metal can be deposited on the surface of the anode[17-19]. This lithium plating can lead to safety concerns due to the problems with metallic lithium anodes outlined above[20]. This is generally not an issue in relatively small batteries like those seen in portable electronic equipment, however, it can become an issue in larger scale batteries.

While graphite is the most wildly used carbonaceous anode material it is not the only one[21]. Carbonaceous materials capable of reversible Li^+ insertion are split in to two broad classes – graphitic (soft carbons) and non-graphitic (hard carbons). Graphitic carbons are layered materials though while graphite has perfect stacking of graphene layers, graphitic carbons may have structural defects. Non-graphitic carbons are disordered. Hard carbons are a class of materials that are currently of interest due to their large capacities. They are synthesised from organic precursors that char as they undergo pyrolysis. This can be a range of cheap materials like epoxy resins and sugars. There is a larger gap between graphene sheets (0.38 nm as opposed to 0.335 nm for graphite) this results in no volume change in lithium

insertion/extraction and good cyclability. While hard carbons can produce higher capacities than graphite, due to the disordered structure allowing more lithium to be inserted, and have good cyclability, they also have several disadvantages. Hard carbons have a larger irreversible capacity loss on the first discharge and a larger hysteresis in the voltage profile than seen for graphite. This is partly due to the larger active surface area of hard carbons leading to more SEI layer formation[22] and partly due to the exposure of the material to air after the pyrolysis process leading to reactive functional groups on the surface of the hard carbon[23]. The disordered nature of hard carbons also results in them being less dense than graphite and therefore they produce lower volumetric capacities.

1.3.3.2 Titanates

Due to the safety concerns with using graphite, anode materials that operate at higher voltages, and thus avoid Li plating and SEI layer formation, have been explored. The most extensively researched are oxides of titanium because they have the lowest voltage of the light weight transition metal oxides[24]. $Li_4Ti_5O_{12}$[25,26] was first reported to insert lithium in 1989 by K.M Colbow et al. and by the mid-nineties full cells had been reported using $LiCoO_2$ as the cathode. $Li_4Ti_5O_{12}$ has a defect spinel structure. In the regular spinel $LiTi_2O_4$, lithium occupies 1/8 of the tetrahedral holes and titanium 1/2 of the octahedral holes, in $Li_4Ti_5O_{12}$ (alternatively: $Li_{4/3}Ti_{5/3}O_4$) one sixth of the titanium in the octahedral sites has been replaced by lithium[27].

Lithium can be inserted in to the tetrahedral sites to form $Li_7Ti_5O_{12.}$ Insertion takes place at ~ 1.55 V vs Li^+/Li^0 and deinsertion at ~ 1.6 V. While this is lower than insertion/deinsertion potentials seen in oxide cathode materials (see section 1.4.2) it is significantly higher than graphite[28]. Although, this has the advantage of avoiding lithium dendrite formation and also SEI layer formation, resulting in very little irreversible capacity loss on the first cycle, the

higher potential of lithium insertion results in a considerable reduction of the working voltage when used in a full cell.

The theoretical capacity for the reaction:

$$Li_4Ti_5O_{12} + 3Li^+ + 3e^- \rightleftharpoons Li_7Ti_5O_{12}$$

is ~ 175 $mAhg^{-1}$. This process is extremely reversible partly due to the lack of an SEI layer and partly to the fact the insertion occurs with a very small volume expansion. This leads to excellent cyclability which compensates for the modest capacity. While nanosizing and doping $Li_4Ti_5O_{12}$ have resulted in improvements in performance they cannot change the fundamental issues with the high voltage of insertion of Li^+ and the modest capacity. There is also growing concern about the evolution of hydrogen and other gases from $Li_4Ti_5O_{12}$ upon cycling, this is especially an issue at elevated temperatures[29]

A second group of titanates that have been studied is TiO_2[30]. TiO_2 exists as different polymorphs and the electrochemical performance is dependent on the polymorph present. The only polymorphs that reversibly insert lithium as a bulk material are TiO_2-B and anatase, however, other polymorphs also do when nanoscaled[31]. TiO_2-B nanowires show the most promise due to their high theoretical capacities of 335 $mAhg^{-1}$ and reversible electrochemical behaviour[32]. However, like $Li_4Ti_5O_{12}$, insertion of Li^+ is > 1.5 V vs Li^+/Li^0.

To maximise the voltage of full cells and also avoid issues with lithium dendrites and excessive SEI layer formation it would be beneficial to have an anode that operates at a potential between graphite and $Li_4Ti_5O_{12}$.

1.3.3.3 Alloys

While many metals and metalloids can alloy with lithium[33] between 0 V and 1 V vs Li^+/Li^0, silicon is the most extensively studied. Silicon was first investigated in the mid-nineties as an

additive to carbon[34] before being investigated as a material in its own right. Silicon is particularly appealing due to its low cost and high theoretical capacity[35]. Silicon can react with lithium to form the alloy $Li_{4.4}Si$, resulting in the very large theoretical capacity of 4200 $mAhg^{-1}$ – over 10 times that of commercial graphite electrodes.

While silicon certainly has a lot of potential, pure Si anodes are some way from being commercialised[33]. The most significant issue is that the alloying process results in massive volume expansion of ~ 400%. This results in pulverisation of Si particles and subsequently leads to a loss of contact between Si particles and both current collector and conductive carbon additive. For this reason bulk micron sized silicon suffers from massive irreversible capacity on the first cycle (>2000 $mAhg^{-1}$) and constant capacity fade. By limiting the amount of lithium alloyed, therefore restricting the volume change to 100%, and by using nanoparticles and other nanostructured materials much better cycling can be achieved[36,37]. Using a large amount of conducting carbon additive can also help as it can form a buffer that eases the pulverisation and increases electronic conductivity, although this decreases the volumetric capacity. However, even using the above methods silicon still has a large irreversible capacity loss on the first cycle and displays a relatively poor cycling efficiency (discharge capacity/charge capacity).

A second issue with silicon as an anode material is the potentials at which the alloying and de-alloying processes occur. When Si is discharged the lithium alloy begins to be formed at approximately 0.3 V but the process continues to ~0.01 V. The reverse process begins at ~0.2 V and continues to ~0.6 V. This poses several issues, firstly having to cycle to such low voltages leads to large SEI layer formation that is partly responsible for the large irreversible capacity loss on the first cycle. Secondly, the large polarisation (difference between charge and discharge potentials) results in voltage loss in full cells.

Other studied alloys include: Sn, Sb, Al, Bi, P and Mg[33]. The operating voltages and theoretical/reversible capacities of these materials vary but they share many of the problems of silicon, principally the large volume expansion. Tin is the most commonly studied lithium alloy anode after silicon, while it has a lower theoretical capacity (994 $mAhg^{-1}$) it also has a lower volume expansion (260%), this leads to a smaller irreversible capacity loss on the first cycle and improved cycling. Tin anodes have now been commercialised in the Sony Nexeleon battery, however, the negative factors mean that other possible anode materials operating between graphite and $Li_4Ti_5O_{12}$ still need to be explored.

1.3.3.4 Conversion Reactions

Conversion reactions were first reported in the mid-nineties in $LiMVO_4$ systems (M = Co, Ni, Cd, Zn)[38] but there was increased interest following the reporting of conversion reactions in MO systems (M = Co, Ni, Cu, Fe) by J-M Tarascon and co-workers in 2000[39]. Conversion reactions have since been reported for a range of oxides, sulphides, nitrides, fluorides, phosphides and hydrides. In a conversion reaction lithium does not insert into a host lattice but instead the active material (M_xA_y) is electrochemically reduced forming nanoscale metal particles dispersed in an amorphous Li_nA matrix[40]:

$$M_xA_y + nLi^+ + ne^- \rightleftharpoons xM^0 + yLi_nA$$

Depending on the metal and anion present this can be anything from a one electron process to a four electron process. This can lead to far larger capacities than insertion/intercalation reactions, for example the capacities of 1800 $mAhg^{-1}$ and 1200 $mAhg^{-1}$ have been achieved for CoP_3[41] and Co_3O_4[40] respectively. As promising as these materials appear, like the alloys discussed above, conversion reactions face significant challenges. There is a large structural reorganisation during the conversion process, which leads to a large volume change that, like in alloys, results in poor cycling performance and a large coulombic inefficiency on the first

cycle. There is a large voltage hysteresis between discharge and charge which leads to a round-trip energy density loss; also it is often required to discharge to low potentials (< 0.1 V) to achieve large capacities. Additionally, the formation of nanoscale metal particles can lead to safety issues as these materials are often highly flammable.

One of the most promising conversion materials is MgH_2[42]. It has the lowest polarisation of any reported conversion reaction: ~ 0.4 V, with an average potential of ~ 0.5 V vs Li^+/Li^0, and shows a reversible capacity of 1480 $mAhg^{-1}$. Nevertheless, even this highly performing material is beset by significant issues. There is a 30% irreversible capacity loss on the first cycle and capacity fades rapidly until failure after 20 cycles. Constraining the capacity to 520 $mAhg^{-1}$ alleviates the issue of chronic capacity fade but there are still issues with kinetics and cycling can only be achieved at very slow rates.

While conversion reactions and alloys have the potential to produce very large capacities they have fundamental issues that prevent any practical application. Many of these issues are not found in standard intercalation electrodes, therefore an anode that operates with an intercalation mechanism between graphite and $Li_4Ti_5O_{12}$ would be desirable.

1.3.3.5 Organic Systems

In recent years there has been interest in using organic systems as intercalation electrodes. The most promising of these are conjugated dicarboxylate anodes, and more specifically di-lithium terephthalate, $Li_2C_6H_4O_4$[43]. In a battery di-lithium terephthalate reacts reversibly with lithium as shown:

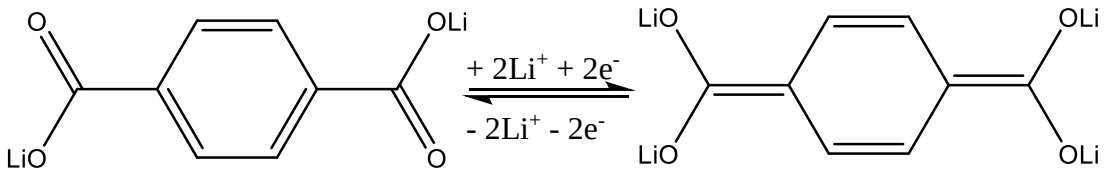

Figure 1.2: Di-lithium terephthalate

Di-lithium terephthalate displays a reversible capacity of 300 $mAhg^{-1}$, which fades to 234 $mAhg^{-1}$ after 50 cycles, with lithium insertion taking place at ~ 0.8 V and extraction at ~ 1.0 V. While specific capacity is not as high as Si or many conversion reactions, it is more impressive than $Li_4Ti_5O_{12}$, but at a potentially more useful voltage. Also, being organic and not containing any transition metals results in di-lithium terephthalate being very cheap to produce. Unsurprisingly, the organic nature of the material is also responsible for several drawbacks. Firstly, as a white solid it has very poor electronic conductivity. To counter this issue each electrode must contain a high proportion of carbon, 30% for $Li_2C_6H_4O_4$ electrodes, and even the recently reported 2,6-Naph$(COOLi)_2$ electrodes contain over 22% carbon[44]. There is also a ~ 30% irreversible capacity loss on the first cycle, some of which is due to the carbon additive. Finally, the low density, 1.6 gcm^{-3}, inherent to these materials[45] results in markedly lower volumetric capacities compared to their inorganic counterparts.

While di-lithium terephthalate shows promise, its organic nature results in several drawbacks and an inorganic material showing similar electrochemical performance would be preferred.

1.3.3.6 $LiMS_2$

Lithium intercalation into metal sulphides has been explored since the origin of Li-ion batteries, indeed in the 1970s, before interest in $LiCoO_2$; sulphides were seen as the most likely materials to be used in commercial Li-ion batteries[46]. Sulphides of the early transition metals, V and Ti, have been of particular interest as both cathode and anode materials[47]. They were initially explored as possible cathode materials by forming MS_2 and inserting lithium to form $LiVS_2$,

however, it was also found that additional lithium could be intercalated to form Li_2MS_2. This process takes place at a lower voltage allowing the use of these systems as anode materials.

$$MS_2 + Li^+ + e^- \rightleftharpoons LiMS_2$$

$$LiMS_2 + Li^+ + e^- \rightleftharpoons Li_2MS_2$$

For both the titanium and vanadium containing materials the first process takes place at ~ 2.5 V vs Li^+/Li^0 which in a modern battery is seen as too low to be a viable cathode material[48], see section 1.4. However, as anode the materials are more interesting. Initial research in the 1970s was hampered by using poor electrolytes[49] and the area was all but forgotten until 2009 when J.B. Goodenough and co-workers re-examined the materials using modern electrolytes[50,51].

$LiTiS_2$ and $LiVS_2$ have the same structure. The $LiMS_2$ structure consists of hexagonal close packed S^{2-} with sheets of octahedral sites alternating between occupancy by Li and M. As all the octahedral sites are occupied, lithium intercalation requires Li^+ to occupy tetrahedral sites that share faces with the Li^+ present in octahedral sites, and is energetically unfavourable. Therefore, when Li^+ is intercalated into the structure all the Li^+ in the octahedral sites are displaced to the neighbouring tetrahedral sites. As there are twice as many tetrahedral sites as octahedral sites this can continue to a theoretical maximum of Li_2MS_2. The crystal structures are shown in the figure below:

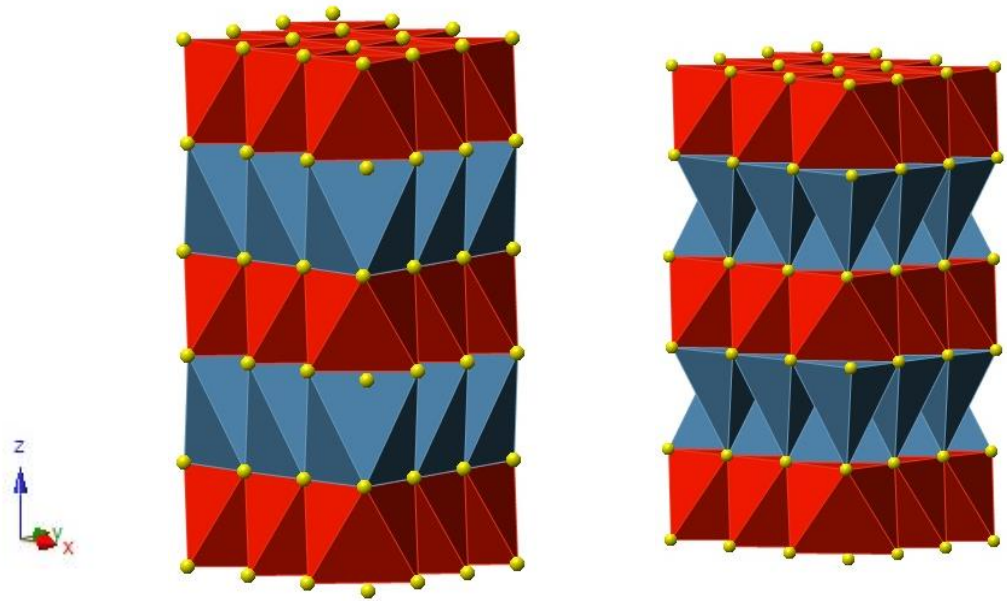

$LiMS_2$ Li_2MS_2

Figure 1.3: Crystal structures of $LiMS_2$ and Li_2MS_2. Sulphur is represented by yellow balls, M octahedra are red and lithium octahedra/tetrahedra are blue.

Lithium intercalates into $LiTiS_2$ at the low voltage of 0.5 V, there is little polarisation and deintercalation occurs at 0.6 V. Like all low voltage anodes there is a large irreversible capacity loss on the first cycle. In work published by Goodenough this is attributed to SEI layer formation[50]. The result of this irreversible capacity loss is a reduction of capacity from ~ 450 $mAhg^{-1}$ on 1st discharge to ~ 200 $mAhg^{-1}$ on 2nd discharge. This is followed by chronic capacity fade, with the capacity being reduced to ~ 100 $mAhg^{-1}$ by cycle 5.

The performance of $LiVS_2$ is somewhat better. Intercalation of Li^+ takes place at ~ 1.0 V and deintercalation at ~ 1.3 V, this results in a polarisation three times that of $LiTiS_2$. As $LiVS_2$ operates at a higher voltage than $LiTiS_2$ there is less SEI layer formation and consequently less irreversible capacity loss on the first cycle, ~70 $mAhg^{-1}$. The theoretical capacity of $LiVS_2$ is 220 $mAhg^{-1}$ and 200 $mAhg^{-1}$ was achieved by Goodenough and co-workers on 2nd discharge. The capacity fade is not as dramatic as $LiTiS_2$ but is more significant than in $Li_4Ti_5O_{12}$, with the loss of 1 $mAhg^{-1}$ per cycle. Published data also shows that capacity drops with increasing

rate: 200mAhg^{-1} at 0.1 C to ~ 100 mAhg^{-1} at C rate. For $LiVS_2$ C-rate is defined as 200 mAg^{-1} since the maximum capacity of the material is roughly 200mAhg^{-1}, see Section 2.5.3 for further discussion. There are also data published on the doped compounds $LiV_{0.9}Cr_{0.1}S_2$ and $LiV_{0.9}Ni_{0.1}S_2$ but neither show improved performance over $LiVS_2$.

While the previously reported performance of $LiVS_2$ is by no means outstanding, it is the most promising published inorganic intercalation anode operating at around 1 V and was thought to show enough potential to warrant further study.

1.3.4 Aims of this Project

The primary aim of this project is the synthesis, characterisation and electrochemical testing of new anode materials for lithium ion batteries. As discussed above there is a need for an anode that operates between graphite and $Li_4Ti_5O_{12}$ in the region of approximately 1 V vs Li^+/Li^0. This will ensure increased safety and minimised irreversible capacity loss compared to graphite but allow for a larger voltage range in a full cell compared to $Li_4Ti_5O_{12}$. As demonstrated by the survey of anode materials currently being researched inorganic intercalation materials have smaller irreversible capacity losses and smaller polarisation compared to alloys and conversion reactions and their higher densities give increased volumetric capacities compared to organic systems.

In Chapter 3 the optimisation of $LiVS_2$ as an anode material is explained. This is developed further in Chapter 4 with the investigation of the solid solution $LiV_{1-x}Ti_xS_2$ in the hopes of combining the cycling performance of $LiVS_2$ with the smaller polarisation and lower voltage of $LiTiS_2$. The optimum $LiV_{1-x}Ti_xS_2$ composition, x = 0.5, is then combined with various cathodes to demonstrate its performance in a working 'rocking-chair' cell. This work can be seen in Chapter 6.

1.4 Cathode materials for Li-ion batteries

While the majority of work in this thesis concerns sulphide anode materials some work has also been carried out on cathode materials. This section will first outline the requirements that a good cathode material will satisfy and then describe the most commonly studied cathode materials. Finally, a material will be chosen to study further and this work will be outlined in Chapter 5 before combining the cathode material with the sulphide anode material in Chapter 6.

1.4.1 Requirements for a suitable cathode

There are several requirements that a material must fulfil before it can be considered as a potential cathode for lithium-ion batteries[52]. Many of these criteria are similar to what was listed for negative electrodes in the previous section and are listed below:

- Contain a easily reducible/oxidised ion, usually a transition metal
- Be able to intercalate/deintercalate lithium reversibly with little or no structural change
- React with lithium with a high free energy of reaction: giving high capacity and high voltage (limited somewhat by the stability of the electrolyte)
- Possess fast reaction kinetics for insertion and removal of Li-ions
- Be a good electrical conductor to allow fast electrochemical reactions
- Be stable to overcharge and overdischarge
- Be low cost
- Be nontoxic and environmentally benign
- Be easily and reproducibly synthesised with the desired morphology
- Be easily fabricated into electrodes

Even more so than previously seen for anode materials, where graphite fulfilled most of the criteria for an anode material, no cathode material fulfils all the above criteria and there is no one size fits all perfect cathode material. The cathode material used in a lithium-ion cell will depend on which of the above requirements is most important to the application the cell is being used for. This has resulted in several different cathode materials being used in commercial lithium-ion batteries.

1.4.2 Overview of cathode materials

While research in anode materials covers a broad range of materials, research in cathode materials is dominated by transition metal oxides. Below some of the most commonly researched classes of cathode material are outlined.

1.4.2.1 Layered $LiMO_2$ systems

In the 1970s, when research in lithium-ion batteries was in its infancy, sulphides were seen as the most likely contenders to be used as the cathode in commercial cells[53]. That all changed with the discovery in 1980 by JB Goodenough and co-workers that **$LiCoO_2$**[54] reversibly deintercalates lithium at ~ 4 V vs Li^+/Li^0. $LiCoO_2$ went on to be used as the cathode in the first commercial lithium-ion batteries in 1991 and is still used in commercial cells today.

$LiCoO_2$ has the α-$NaFeO_2$ structure with R-3m symmetry. It consists of CoO_2 slabs that are made up of edge sharing CoO_6 octahedra with lithium in between the layers[55]. The theoretical capacity for the complete removal of lithium is high at 274 $mAhg^{-1}$. However, in practice it is only possible to remove and reinsert half of the lithium, and the working capacity is ~ 130 $mAhg^{-1}$. This is because a large structural rearrangement occurs upon further extraction of lithium: $LiCoO_2$ has a cubic close packed arrangement of oxygen and in CoO_2 the oxygen is in a hexagonal close packed arrangement. Due to the low working capacity and the relatively high

price and toxicity of cobalt there is interest in other $LiMO_2$ systems. Figure 1.4 below shows the crystal structure of $LiCoO_2$, all other materials in this section are isostructural.

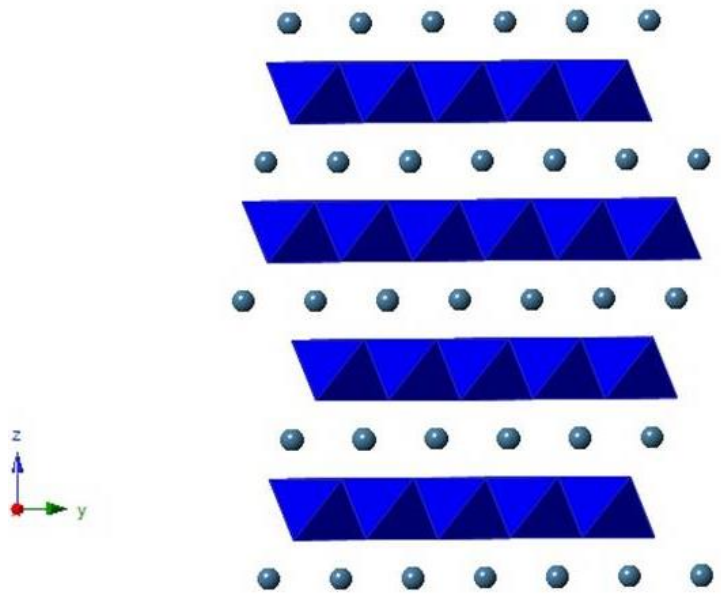

Figure 1.4: Crystal structure of $LiCoO_2$. Lithium are light blue and CoO_6 octahedra are dark blue.

An obvious contender to replace $LiCoO_2$ is the isostructural **$LiNiO_2$**, as nickel is cheaper and less toxic than cobalt[56]. However, $LiNiO_2$ is nickel rich and lithium deficient and actually exists as $Li_{1-x}Ni_{1+x}O_2$. This is due to the similarity in ionic radii between Li^+ and Ni^{2+} (0.76 Å and 0.69 Å respectively), which leads to nickel migration into the lithium layer. The presence of nickel in the lithium layers results in the NiO_2 layers being pinned and a decrease in lithium mobility that in turn leads to poor capacity retention on cycling[57]. $LiNiO_2$ also has issues with safety due to its poor thermal stability, leading to the exothermic release of oxygen at elevated temperatures, this is especially an issue with the delithiated phase[58]. The lack of thermal stability stems from the unstable and oxidising nature of the Ni^{4+} ions.

To overcome the above problems with $LiNiO_2$ the **$LiNi_{1-x}Co_xO_2$** solid solution has also been investigated[59]. Adding nickel increases the capacity and reduces the cost and toxicity compared

to pure $LiCoO_2$. It improves cyclability compared to $LiNiO_2$ because when $x \geq 0.3$ there is no migration of nickel ions to the lithium sites. This is due to the smaller size of the Co^{3+} (0.55 Å) compared to nickel and lithium and also because Co cannot stabilise the tetrahedral sites in which lithium is found.

$LiMnO_2$ is a very appealing cathode material due to manganese being low cost and environmentally benign and $LiMnO_2$ has a high theoretical capacity of 285 $mAhg^{-1}$. However, $LiMnO_2$ is not thermodynamically stable and cannot be synthesised by standard high temperature techniques, instead ion exchange from $NaMnO_2$ and low temperature methods are needed[60]. Unfortunately, the thermodynamic instability of $LiMnO_2$ and high mobility of Mn^{2+} leads to the layered phase gradually converting to the more stable spinel phase ($LiMn_2O_4$) upon cycling, this reduces capacity[61-64].

$LiNi_{0.5}Mn_{0.5}O_2$ is another layered cathode material that has attracted interest[65-67], partly as the high amount of manganese keeps the cost low. The manganese is not electrochemically active and the nickel undergoes a two electron process from Ni^{2+} to Ni^{4+}. This results in $LiNi_{0.5}Mn_{0.5}O_2$ achieving high capacities. It also has excellent thermal stability and good capacity retention. However, it suffers from the mixing of Ni^{2+} and Li^+ that was seen in $LiNiO_2$.

The natural extension of the research discussed above is materials containing nickel, manganese and cobalt[68-71]. The most wildly studied of these materials is **$Li(Ni_{1/3}Mn_{1/3}Co_{1/3})O_2$**[72] (NMC). $Li(Ni_{1/3}Mn_{1/3}Co_{1/3})O_2$ is relatively cheap due to the presence of manganese and displays very good electrochemical properties. It may be cycled to the high voltage of 4.6 V vs Li^+/Li^0 and it can produce capacities as high as 200 $mAhg^{-1}$(the theoretical capacity is 278 $mAhg^{-1}$). NMC has been wildly commercialised.

1.4.2.2 Spinels

Spinels have the composition LiM_2O_4 and belong to the Fd-3m space group. The structure consists of edge sharing MO_6 octahedra with additional M ions in the octahedral sites and lithium ions in the tetrahedral sites. The 3D structure of these materials allows for fast lithium extraction/insertion upon cycling[10]. For most cathode spinel materials M is usually entirely or partly manganese. Figure 1.5 displays the crystal structure of $LiMn_2O_4$, other materials (including the anode $Li_4Ti_5O_{12}$) are isostructural.

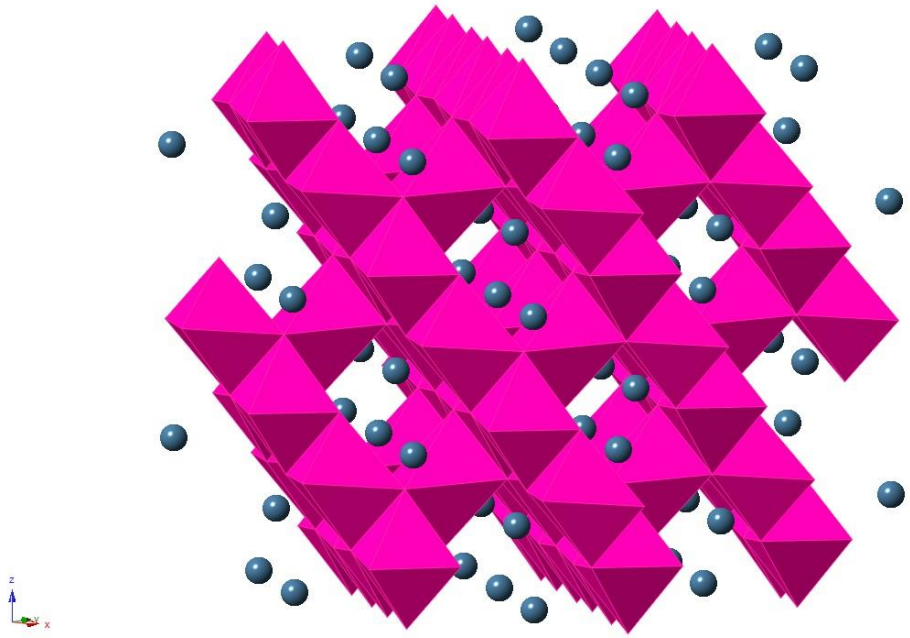

Figure 1.5: Crystal structure of $LiMn_2O_4$. Lithium is represented by the blue spheres and MnO_6 by pink octahedra.

$LiMn_2O_4$ has a modest theoretical capacity of 148 $mAhg^{-1}$ but compensates by being low cost, having low toxicity and being easy to prepare[73-75]. The voltage of lithium insertion and extraction is ~ 4.0 V. Capacity retention is an issue, especially at high temperatures, because of manganese dissolution into the electrolyte. This is due to Mn^{3+} undergoing disproportionation to give Mn^{4+} and the soluble Mn^{2+}. This issue can be somewhat alleviated by synthesising the material with an excess of lithium and forming $Li_{1+x}Mn_{2-x}O_4$ where x is small i.e. 0.05. This

increases the Mn oxidation state and hence the Mn^{3+}/Mn^{4+} ratio and leads to better stability[76]. The lithium rich $LiMn_2O_4$ is currently commercialised for use in electric vehicles.

Another spinel material that has been extensively investigated is the so called 5 volt spinel, **$LiNi_{0.5}Mn_{1.5}O_4$**[77,78]. As the name suggests, extraction/insertion of lithium takes place at almost 5 V vs Li^+/Li^0. The theoretical capacity is virtually the same as for $LiMn_2O_4$ and capacity retention is good[79]. As seen in $LiNi_{0.5}Mn_{0.5}O_2$ both Ni^{4+}/Ni^{3+} and Ni^{3+}/Ni^{2+} redox couples are involved in the electrochemical process. $LiNi_{0.5}Mn_{1.5}O_4$ exists in both ordered and disordered forms[80]. The disordered form is difficult to synthesise but has a greater lithium ion diffusion coefficient that results in better cycling performance. However, conventional electrolytes begin to decompose around 5 V and this limits the use of $LiNi_{0.5}Mn_{1.5}O_4$ in practical applications.

1.4.2.3 Polyoxyanion compounds

First reported in 1997 by J.B. Goodenough and co-workers **$LiFePO_4$** is one of the most extensively studied cathode materials for lithium-ion batteries[81,82]. $LiFePO_4$ has an orthorhombic olivine structure with *Pnma* symmetry. The structure consists of layers of vertices sharing FeO_6 octahedra and PO_4^{3-} tetrahedra that share edges and vertices with the FeO_6 octahedra, this arrangement results in the PO_4^{3-} tetrahedra connecting layers of FeO_6. Li^+ is found on the octahedral sites in the structure. The crystal structure can be seen in the figure below.

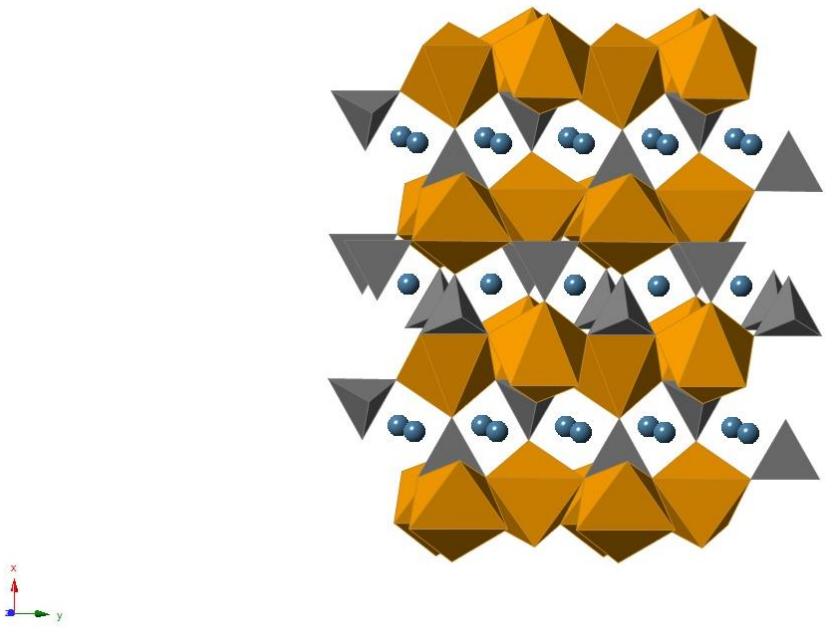

Figure 1.6: Crystal structure of $LiFePO_4$. Lithium is represented by blue spheres, FeO_6 by mustard octahedra and PO_4^{3-} by grey tetrahedra.

The strong P-O bonds that are prevalent across the structure result in the structure being very stable and safe. This structural stability results in virtually no capacity fade on cycling and is one of the biggest strengths of $LiFePO_4$. Other advantages of $LiFePO_4$ include the high natural abundance and low cost of iron, this makes $LiFePO_4$ one of the cheapest cathode materials to synthesise. $LiFePO_4$ is also relatively easy to produce, has a reasonably high theoretical capacity of 170 $mAhg^{-1}$ and is environmentally benign. $LiFePO_4$ also has several significant drawbacks. It has low electronic (10^{-9} Scm^{-1}) and ionic (10^{-5} Scm^{-1}) conductivities that make cycling at room temperature difficult[83,84]. The conductivity can be improved by nanosizing[85] and carbon coating[86] but this leads to an increase in electrochemically inactive material and therefore a reduction in energy density. Another issue is that lithium insertion/extraction takes place at ~ 3.4 V vs Li^+/Li^0, this is up to 1 V lower than the layered and spinel materials described above. This results in a reduction in the voltage of any full cell made with $LiFePO_4$ and limits which anode materials it can be paired with.

A second class of polyoxyanion materials that has garnered interest in recent years are the **Li_2MSiO_4** family of materials, where M = Mn, Fe or Co[87-89]. Li_2MSiO_4 materials can exist as 4 different polymorphs denoted β_{II}, $\gamma_{II.}$ γ_s and γ_o. These structures are made up of a tetragonal arrangement of oxide ions and the cations occupy half of the tetrahedral sites. The cations in the tetrahedral sites can order in different ways, face sharing is always avoided, and this leads to the 4 polymorphs listed above. The particular polymorph formed is dependent on which cations are present and the synthesis conditions.

Interest in Li_2MSiO_4 materials stems from their low cost (Mn and Fe are relatively cheap) and inherent safety (stemming from there high thermal stability due to the strong Si-O bonds. Li_2FeSiO_4 was first investigated as a cathode in 2005[90] and undergoes a 1 electron process that reversibly extracts and reinserts 1 Li^+. This has a theoretical capacity of 166 $mAhg^{-1}$. Li_2MnSiO_4 can theoretically undergo a two electron process that would result in a theoretical capacity of 333 $mAhg^{-1}$ [91]. In practice, however, it appears that only one lithium can be reversibly removed and reinserted. Both Li_2FeSiO_4 and Li_2MnSiO_4 have issues with the voltage they operate at. After the first 2 cycles Li_2FeSiO_4 operated at ~ 2.75 V which is very low for a cathode material. Li_2MnSiO_4 deintercalates lithium at ~ 4 V but the load curve displays very large polarisation. Using a mix of transition metals can alleviate these issues to a certain degree. Additionally, all silicate materials suffer from poor electronic conductivities and like $LiFePO_4$ elevated temperatures, nanosizing and carbon coating are often needed to obtain good cycling performance.

1.4.2.4 Lithium-rich mixed metal oxides

The final class of cathodes considered here are the lithium-rich mixed metal oxides (LR-MMO); these have been subject to an enormous amount of research in the last 15 years due to their high capacities (> 200 $mAhg^{-1}$)[92,93]. These materials are also sometimes referred to as manganese rich metal oxides due to their high manganese content. They can be described as a mixture of

Li_2MnO_3 and $LiMO_2$ and are often denoted in form xLi_2MnO_3:(1-x)$LiMO_2$, where M is usually a mixture of nickel, manganese and cobalt but materials using Cr[94], Al[95], Mg[96] and Fe[97] have been reported. These lithium rich metal oxide materials can be readily synthesised due to the structural similarities between Li_2MnO_3 and $LiMO_2$. This can be easily understood by reformulating Li_2MnO_3 as $Li[Li_{1/3}Mn_{2/3}]O_2$, which is the traditional layered notation, and noting it has the same structure as $LiMO_2$ with 1/3 of the transition metals being replaced by lithium. This similarity of structure and the similar interlayer separation (~ 4.7 Å) allows for the integration of the two materials at an atomic level. The structure of LR-MMOs is complicated and still a subject of much debate, while the X-ray diffraction patterns appear to be single phase[98], there is evidence that material is made of a mixture of Li_2MnO_3 and $LiMO_2$ regions[99-101].

The appeal of this class of materials is that they can achieve high capacities > 220 $mAhg^{-1}$ with good capacity retention, this takes place over a large voltage window: the material is typically cycled between 2 V and 4.8 V vs Li^+/Li^0. The electrochemical process of xLi_2MnO_3:(1-x)$LiMO_2$ has been comprehensively studied and there has been a specific focus on the first charge but there is still much discussion relating to the exact processes taking place. The first charge load curve displays two distinct processes[102]. The first region, up to ~ 4.4 V, corresponds to the oxidation of the transition metals in $LiMO_2$ to M^{4+} [99]. This is demonstrated below by the equation for $Li_{1.2}Mn_{0.54}Ni_{0.13}Co_{0.13}O_2$, oxidation states for the transition metals are in red:

$$Li_{1.2}Mn(\mathbf{+4})_{0.54}Ni(\mathbf{+2})_{0.13}Co(\mathbf{+3})_{0.13}O_2 \rightarrow Li_{0.81}Mn(\mathbf{+4})_{0.54}Ni(\mathbf{+4})_{0.13}Co(\mathbf{+4})_{0.13}O_2 + 0.39Li^+ + 0.39e^-$$

While there is a consensus about the nature of the low voltage plateau, the second plateau, at ~ 4.5 – 4.8 V, is more controversial, and it is not so obvious by which mechanism the lithium extraction takes place. As the manganese in the material is Mn^{4+} and is highly unlikely to form Mn^{5+} the lithium extraction cannot take place via a traditional transition metal redox process.

The high voltage plateau occurs simultaneously with irreversible capacity loss and the most commonly reported mechanism for this 'extra' capacity is that Li^+ is removed simultaneously with oxygen from the lattice, observing the following equation:

$$2O^{2-} + 4Li^+ \rightarrow O_2 + 4e^- + 4Li^{+}$$ [103]

Oxygen gas evolution has been observed via differential electrochemical mass spectrometry[104], however, CO_2 has also been detected leading to proposals concerning reactions involving the formation and decomposition of carbonates[105]. Additionally, surface enhanced Ramen spectroscopy has been used to show the formation of Li_2O during the high voltage plateau[106].

A similar mechanism that has been proposed is the oxygen redox mechanism, where the oxygen loss is charge compensated by a redox process on the oxygen anion[107]. This was suggested due to the fact that following lithium extraction more lithium can be reinserted than would be expected from the redox processes of the transition metals[108]. The oxidation of O^{2-} to O_2^{2-} has been observed for $Li_2Ru_{1-x}Sn_xO_3$ using XPS and EPR[107], and it was speculated that the same process occurred on charge in $Li_{1+x}M_{1-x}O_2$ materials. However, it has recently been demonstrated that Li^+ removal is charge compensated by the formation of localized electron holes on O atoms coordinated by Mn^{4+} and Li^+ ions, and there is no formation O_2^{2-}.[109]

There is also some evidence for a proton exchange mechanism at elevated temperatures[110] that involves the electrochemical activity of Li_2MnO_3 and the exchange of Li^+ by H^+, this leads to the formation of $Li_{0.62}H_{1.29}MnO_{2.95}$[111]. Additionally, it is thought that proton exchange may be responsible for cells demonstrating more capacity than their theoretical capacity[112].

On cycling as Li_2MnO_3 becomes MnO_2 at > 4.5 V the manganese may not be electrochemically active, however, there is some evidence that it is still responsible for high capacities due to lithium migration[100,113-115]. The migration takes place between lithium rich Li_2MnO_3 and lithium deficient $LiMO_2$ – MO_2 areas after lithium has been extracted. The lithium from

Li_2MnO_3 stabilises the MO_2 areas and prevents changes in symmetry and distortion of the crystal structure. In turn this allows for more lithium to be extracted compared to traditional layered materials and higher capacities can be achieved. It has also been suggested that the lithium extraction that coincides with the oxygen loss leads to the lowering of the oxidation states of the transition metals at the end of the first discharge, and this effect results in the high reversible capacity seen in the following cycles[114]. After the initial few cycles, as the manganese regions are 'activated', there is a voltage fade as the manganese process takes place at a lower potential. On extended cycling there is evidence that the material converts to the spinel phase[116-118], this results in even greater voltage fade.

The precise electrochemistry displayed by a material is very dependent on the transition metals found in the $LiMO_2$ component and the ratio of Li_2MnO_3 to $LiMO_2$. Two of the most studied solid solutions are xLi_2MnO_3:(1-x)$LiNi_{0.5}Mn_{0.5}O_2$ and xLi_2MnO_3:(1-x)$Li(Ni_{1/3}Mn_{1/3}Co_{1/3})O_2$ which are the natural extensions of the layered materials $LiNi_{0.5}Mn_{0.5}O_2$ and $Li(Ni_{1/3}Mn_{1/3}Co_{1/3})O_2$ respectively, that were discussed in Section 1.4.2.1. The electrochemistry is also reliant on the synthetic method used to make the material. The first method used to synthesis these materials was hydroxide co-precipitation[119] and it is still the most wildly used. As well as coprecipitation methods a wide range of synthetic techniques have been used to make these types of material, including: sol-gel methods using glycolic acid[120], traditional solid state reactions[121], various types of solution polymerisation reactions[122] and acid leeching of Li_2MnO_3 mixed with metal nitrates[123].

1.4.3 Aim of this project

The ultimate goal of this work is to make a cathode material that performs well and can be used in a full 'rocking-chair' cell with an optimised sulphide material. As sulphides operate at ~ 1 V having a cathode that operates at a high voltage is important to maximise the cell potential. The

lithium-rich mixed metal oxides display the highest capacities of the cathode materials surveyed above and do so at a high voltage. Therefore, the lithium rich mixed metal oxides have been chosen for further investigation.

Previous work by this research group on $Li(Ni_{0.5}Mn_{1.5})O_4$[78] and $LiNi_{1/3}Mn_{1/3}Co_{1/3}O_2$[124] has found that syntheses that involve resorcinol - formaldehyde gels (RF gels) result in materials with excellent cyclability. Chapter 5 will outline the RF-gel synthesis of $0.5Li_2MnO_3{:}0.5LiNi_{0.5}Mn_{0.5}O_2$ and $0.6Li_2MnO_3{:}0.4Li(Ni_{1/3}Mn_{1/3}Co_{1/3})O_2$, which can denoted $Li(Li_{0.17}Ni_{0.25}Mn_{0.58})O_2$ and $Li(Li_{0.2}Ni_{0.13}Mn_{0.54}Co_{0.13})O_2$ respectively. These two compositions were chosen as they are two of the best performing LR-MMO materials. It is hoped that the RF-gel synthesis will result in improved capacity retention compared to previously reported synthetic techniques. More details of the RF-gel synthesis technique are outlined in Chapter 2.

Chapter 5 will also include neutron diffraction experiments that were carried out on $0.5Li_2MnO_3{:}0.5LiNi_{0.5}Mn_{0.5}O_2$ and $0.6Li_2MnO_3{:}0.4Li(Ni_{1/3}Mn_{1/3}Co_{1/3})O_2$ after extended cycling. This work was carried out in collaboration with Dr A.R. Armstrong at the University of St Andrews and was done to gain a better understanding of the structural changes these materials undergo on extended cycling.

1.5 References

1 Pazheri, F. R., Othman, M. F. & Malik, N. H. *Renew. Sust. Energ. Rev.* **31**, 835-845 (2014).
2 Whittingham, M. S. *J. Electrochem. Soc.* **123**, 315-320 (1976).
3 Nagura T. and Tozawa K. *Prog. Batt. Sol. Cells, 1990, 9, 209* (1990).
4 Linden, D. R., T.B.
5 Ossola, F., Pistoia, G., Seeber, R. & Ugo, P. *Electrochim. Acta* **33**, 47-50 (1988).
6 Aurbach, D., Zinigrad, E., Cohen, Y. & Teller, H. *Solid State Ion.* **148**, 405-416 (2002).
7 Arakawa, M. & Yamaki, J. *J. Power Sources* **54**, 250-254 (1995).
8 Aurbach, D., Gofer, Y., Benzion, M. & Aped, P. *J. Electroanal. Chem.* **339**, 451-471 (1992).
9 Kominato, A. *et al. J. Power Sources* **68**, 471-475 (1997).
10 Nitta, N. & Yushin, G. *Part. Part. Syst. Charact.* **31**, 317-336 (2014).
11 Peled, E. *J. Electrochem. Soc.* **126**, 2047-2051 (1979).
12 Verma, P., Maire, P. & Novak, P. *Electrochim. Acta* **55**, 6332-6341 (2010).
13 Guerard, D. & Herold, A. *Carbon* **13**, 337-345 (1975).
14 Sivakkumar, S. R., Nerkar, J. Y. & Pandolfo, A. G. *Electrochim. Acta* **55**, 3330-3335 (2010).
15 Yazami, R. & Touzain, P. *J. Power Sources* **9**, 365-371 (1983).
16 Noel, M. & Suryanarayanan, V. *J. Power Sources* **111**, 193-209 (2002).
17 Zhang, S. S. *J. Power Sources* **161**, 1385-1391 (2006).
18 Smart, M. C. & Ratnakumar, B. V. *J. Electrochem. Soc.* **158**, A379-A389 (2011).
19 Ratnakumar, B. V. & Smart, M. C. *Rechargeable Lithium-Ion Batteries* **25**, 241-252 (2010).
20 Vonsacken, U., Nodwell, E., Sundher, A. & Dahn, J. R. . *J. Power Sources* **54**, 240-245 (1995).
21 Winter, M., Besenhard, J. O., Spahr, M. E. & Novak, P. *Advanced Materials* **10**, 725-763 (1998).
22 Beguin, F. *et al. Carbon* **43**, 2160-2167 (2005).
23 Buiel, E. & Dahn, J. R. *Electrochim. Acta* **45**, 121-130 (1999).
24 Zhu, G. N., Wang, Y. G. & Xia, Y. Y. *Energy Environ. Sci.* **5**, 6652-6667 (2012).
25 Yang, Z. G. *et al. J. Power Sources* **192**, 588-598 (2009).
26 Ferg, E., Gummow, R. J., Dekock, A. & Thackeray, M. M. *J. Electrochem. Soc.* **141**, L147-L150 (1994).
27 Colbow, K. M., Dahn, J. R. & Haering, R. R. *J. Power Sources* **26**, 397-402 (1989).
28 Kavan, L. & Gratzel, M. *Electrochem. Solid State Lett.* **5**, A39-A42 (2002).
29 He, M. L. *et al. J. Electrochem. Soc.* **162**, A870-A876 (2015).
30 Armstrong, A. R., Armstrong, G., Canales, J., Garcia, R. & Bruce, P. G. *Advanced Materials* **17**, 862-+ (2005).
31 Baudrin, E. *et al. Electrochem. Commun.* **9**, 337-342 (2007).
32 Armstrong, A. R., Armstrong, G., Canales, J. & Bruce, P. G. *Angew. Chem.-Int. Edit.* **43**, 2286-2288 (2004).
33 Zhang, W. J. *J. Power Sources* **196**, 13-24 (2011).
34 Wilson, A. M. & Dahn, J. R. *J. Electrochem. Soc.* **142**, 326-332 (1995).
35 Liang, B., Liu, Y. P. & Xu, Y. H. *J. Power Sources* **267**, 469-490 (2014).
36 Graetz, J., Ahn, C. C., Yazami, R. & Fultz, B. *Electrochem. Solid State Lett.* **6**, A194-A197 (2003).
37 Park, M. H. *et al. Nano Lett.* **9**, 3844-3847 (2009).

38 Sigala, C., Guyomard, D., Piffard, Y. & Tournoux, M. *Comptes Rendus De L Academie Des Sciences Serie Ii* **320**, 523-529 (1995).
39 Poizot, P., Laruelle, S., Grugeon, S., Dupont, L. & Tarascon, J. M. *Nature* **407**, 496-499 (2000).
40 Cabana, J., Monconduit, L., Larcher, D. & Palacin, M. R. *Adv. Mater.* **22**, E170-E192 (2010).
41 Pralong, V., Souza, D. C. S., Leung, K. T. & Nazar, L. F. *Electrochem. Commun.* **4**, 516-520 (2002).
42 Oumellal, Y., Rougier, A., Nazri, G. A., Tarascon, J. M. & Aymard, L. *Nat. Mater.* **7**, 916-921 (2008).
43 Armand, M. *et al. Nat. Mater.* **8**, 120-125 (2009).
44 Ogihara, N. *et al. Angew. Chem.-Int. Edit.* **53**, 11467-11472 (2014).
45 Kaduk, J. A. *Acta Crystallogr. Sect. B-Struct. Sci.* **56**, 474-485 (2000).
46 Whittingham, M. S. *Prog. Solid State Chem.* **12**, 41-99 (1978).
47 Murphy, D. W., Cros, C., Disalvo, F. J. & Waszczak, J. V. *Inorg. Chem.* **16**, 3027-3031 (1977).
48 Murphy, D. W., Carides, J. N., Disalvo, F. J., Cros, C. & Waszczak, J. V. *Mater. Res. Bull.* **12**, 825-830 (1977).
49 Murphy, D. W. & Carides, J. N. *J. Electrochem. Soc.* **126**, 349-351 (1979).
50 Kim, Y., Park, K. S., Song, S. H., Han, J. T. & Goodenough, J. B. *J. Electrochem. Soc.* **156**, A703-A708 (2009).
51 Gupta, A., Mullins, C. B. & Goodenough, J. B. *Electrochim. Acta* **78**, 430-433 (2012).
52 Whittingham, M. S. *Chem. Rev.* **104**, 4271-4301 (2004).
53 Vanlaar, B. & Ijdo, D. J. W. *J. Solid State Chem.* **3**, 590-& (1971).
54 Mizushima, K., Jones, P. C., Wiseman, P. J. & Goodenough, J. B. *Mater. Res. Bull.* **15**, 783-789 (1980).
55 Orman, H. J. & Wiseman, P. J. *Acta Crystallogr. Sect. C-Cryst. Struct. Commun.* **40**, 12-14 (1984).
56 Broussely, M. *et al. J. Power Sources* **54**, 109-114 (1995).
57 Rougier, A., Gravereau, P. & Delmas, C. *J. Electrochem. Soc.* **143**, 1168-1175 (1996).
58 Dahn, J. R., Fuller, E. W., Obrovac, M. & Vonsacken, U. *Solid State Ion.* **69**, 265-270 (1994).
59 Zhecheva, E. & Stoyanova, R. *Solid State Ion.* **66**, 143-149 (1993).
60 Bruce, P. G., Armstrong, A. R. & Gitzendanner, R. L. *J. Mater. Chem.* **9**, 193-198 (1999).
61 Shao-Horn, Y. *et al. J. Electrochem. Soc.* **146**, 2404-2412 (1999).
62 Armstrong, A. R., Paterson, A. J., Dupre, N., Grey, C. P. & Bruce, P. G. *Chem. Mat.* **19**, 1016-1023 (2007).
63 Armstrong, A. R., Dupre, N., Paterson, A. J., Grey, C. P. & Bruce, P. G. *Chem. Mat.* **16**, 3106-3118 (2004).
64 Paterson, A. J., Armstrong, A. R. & Bruce, P. G. *J. Electrochem. Soc.* **151**, A1552-A1558, doi:10.1149/1.1786074 (2004).
65 Ohzuku, T. & Makimura, Y. *Chem. Lett.*, 744-745 (2001).
66 Cushing, B. L. & Goodenough, J. B. *Solid State Sci.* **4**, 1487-1493 (2002).
67 Makimura, Y. & Ohzuku, T. *J. Power Sources* **119**, 156-160 (2003).
68 Yabuuchi, N. & Ohzuku, T. *J. Power Sources* **119**, 171-174 (2003).
69 Liu, Z. L., Yu, A. S. & Lee, J. Y. *J. Power Sources* **81**, 416-419 (1999).
70 Chen, Y., Wang, G. X., Konstantinov, K., Liu, H. K. & Dou, S. *J. Power Sources* **119**, 184-188 (2003).

71 Lu, Z. H., MacNeil, D. D. & Dahn, J. R. *Electrochem. Solid State Lett.* **4**, A200-A203 (2001).
72 Belharouak, I., Sun, Y. K., Liu, J. & Amine, K. *J. Power Sources* **123**, 247-252 (2003).
73 Tarascon, J. M., Wang, E., Shokoohi, F. K., McKinnon, W. R. & Colson, S. *J. Electrochem. Soc.* **138**, 2859-2864 (1991).
74 Tarascon, J. M. *et al. J. Electrochem. Soc.* **141**, 1421-1431 (1994).
75 Shin, Y. J. & Manthiram, A. *J. Electrochem. Soc.* **151**, A204-A208 (2004).
76 Gummow, R. J., Dekock, A. & Thackeray, M. M. *Solid State Ion.* **69**, 59-67 (1994).
77 Amine, K., Tukamoto, H., Yasuda, H. & Fujita, Y. *J. Power Sources* **68**, 604-608 (1997).
78 Shaju, K. M. & Bruce, P. G. *Dalton Trans.*, 5471-5475 (2008).
79 Lee, Y. S., Sun, Y. K., Ota, S., Miyashita, T. & Yoshi, M. *Electrochem. Commun.* **4**, 989-994 (2002).
80 Santhanam, R. & Rambabu, B. *J. Power Sources* **195**, 5442-5451 (2010).
81 Padhi, A. K., Nanjundaswamy, K. S., Masquelier, C., Okada, S. & Goodenough, J. B. *J. Electrochem. Soc.* **144**, 1609-1613 (1997).
82 Huang, H., Yin, S. C. & Nazar, L. F. *Electrochem. Solid State Lett.* **4**, A170-A172 (2001).
83 Delacourt, C. *et al. J. Electrochem. Soc.* **152**, A913-A921 (2005).
84 Morgan, D., Van der Ven, A. & Ceder, G. *Electrochem. Solid State Lett.* **7**, A30-A32 (2004).
85 Chung, S. Y., Bloking, J. T. & Chiang, Y. M. *Nat. Mater.* **1**, 123-128 (2002).
86 Prosini, P. P., Zane, D. & Pasquali, M. *Electrochim. Acta* **46**, 3517-3523 (2001).
87 Lyness, C., Delobel, B., Armstrong, A. R. & Bruce, P. G. *Chem. Commun.*, 4890-4892 (2007).
88 Islam, M. S. *et al. J. Mater. Chem.* **21**, 9811-9818 (2011).
89 Gong, Z. L. & Yang, Y. *Energy Environ. Sci.* **4**, 3223-3242 (2011).
90 Nyten, A., Abouimrane, A., Armand, M., Gustafsson, T. & Thomas, J. O. *Electrochem. Commun.* **7**, 156-160 (2005).
91 Dominko, R. *et al. Electrochem. Commun.* **8**, 217-222 (2006).
92 Kim, H. J., Jung, H. G., Scrosati, B. & Sun, Y. K. *J. Power Sources* **203**, 115-120 (2012).
93 Numata, K., Sakaki, C. & Yamanaka, S. *Solid State Ionics* **117**, 257-263 (1999).
94 Jiao, L. F. *et al. J. Power Sources* **167**, 178-184 (2007).
95 Park, S. H. & Sun, Y. K. *J. Power Sources* **119**, 161-165, doi:10.1016/s0378-7753(03)00171-x (2003).
96 Lee, C. W., Sun, Y. K. & Prakash, J. *Electrochim. Acta* **49**, 4425-4432 (2004).
97 Kikkawa, J. *et al. J. Appl. Phys.* **103** (2008).
98 Park, K. S., Cho, M. H., Jin, S. J., Song, C. H. & Nahm, K. S. . *J. Power Sources* **146**, 281-286 (2005).
99 Lu, Z. H., Chen, Z. H. & Dahn, J. R. *Chem. Mater.* **15**, 3214-3220 (2003).
100 Thackeray, M. M., Johnson, C. S., Vaughey, J. T., Li, N. & Hackney, S. A. *J. Mater. Chem.* **15**, 2257-2267 (2005).
101 Yu, X. Q. *et al. Adv. Energy Mater.* **4**, 11 (2014).
102 Wu, Y. & Manthiram, A. *Electrochem. Solid State Lett.* **9**, A221-A224 (2006).
103 Johnson, C. S. *et al. Electrochem. Commun.* **6**, 1085-1091 (2004).
104 Armstrong, A. R. *et al. J. Am. Chem. Soc.* **128**, 8694-8698 (2006).
105 Castel, E., Berg, E. J., El Kazzi, M., Novak, P. & Villevieille, C. *Chem. Mat.* **26**, 5051-5057 (2014).

106 Hy, S., Felix, F., Rick, J., Su, W. N. & Hwang, B. J. *J. Am. Chem. Soc.* **136**, 999-1007 (2014).
107 Sathiya, M. *et al. Nat. Mater.* **12**, 827-835 (2013).
108 Koga, H. *et al. J. Phys. Chem. C* **118**, 5700-5709 (2014).
109 Luo, K. *et al. Nat. Chem.* ***8,*** *423-430 (2016)*
110 Thackeray, M. M. *et al. J. Mater. Chem.* **17**, 3112-3125 (2007).
111 Robertson, A. D. & Bruce, P. G. *Chem. Commun. (Cambridge, U. K.)*, 2790-2791 (2002).
112 Li, B. J., Wang, Q. B., Zhang, Y., Song, Z. S. & Yang, D. M. *Int. J. Electrochem. Sci.* **8**, 5396-5406 (2013).
113 Ates, M. N. *et al. J. Electrochem. Soc.* **161**, A290-A301 (2014).
114 Johnson, C. S., Li, N. C., Lefief, C. & Thackeray, M. M. *Electrochem. Commun.* **9**, 787-795 (2007).
115 Yu, C. *et al. Electrochim. Acta* **81**, 283-291 (2012).
116 Lu, Z. H., Beaulieu, L. Y., Donaberger, R. A., Thomas, C. L. & Dahn, J. R. *J. Electrochem. Soc.* **149**, A778-A791 (2002).
117 Kikkawa, J. *et al. Electrochem. Solid State Lett.* **11**, A183-A186 (2008).
118 Gu, M. *et al. ACS Nano* **7**, 760-767 (2013).
119 Lu, Z. H., MacNeil, D. D. & Dahn, J. R. *Electrochem. Solid State Lett.* **4**, A191-A194 (2001).
120 Sun, Y. K., Shin, S. S. & Oh, I. H. *J. Appl. Electrochem.* **32**, 1053-1056 (2002).
121 Zhang, L. Q. *et al. Mater. Lett.* **58**, 3197-3200 (2004).
122 Xu, H. Y., Wang, Q. Y. & Chen, C. H. *J. Solid State Electrochem.* **12**, 1173-1178 (2008).
123 Croy, J. R. *et al. J. Electrochem. Soc.* **159**, A781-A790 (2012).
124 Shaju, K. M. & Bruce, P. G. *Adv. Mater.* **18**, 2330-+ (2006).

Chapter 2: Experimental Methods and Theory

2.1 Synthesis Techniques

2.1.1 Sealed Tube Reactions

All of the sulphide anode materials discussed in Chapters 3 and 4 were synthesised in evacuated sealed glass tubes. As the tubes were heated to temperatures of 700 ^{o}C and over the tubes were made from fused silica which has a melting point of ~ 1200 ^{o}C. The use of sealed tubes is a common way for synthesising sulphides as they are often air and moisture sensitive. Additionally, there must be no oxygen present when the reaction takes place to form the required sulphide, and the use of evacuated sealed tubes achieves this. Lithium reacts with fused silica; therefore it was necessary to place the reagents in a carbon crucible.

As reagents were air and moisture sensitive they were stored in an argon filled glove box. Appropriate stoichiometric amounts of reagents: lithium sulphide (Li_2S, Aldrich 99.98%), sulphur (S, Aldrich 99.998%) and transition metal powders (V, Aldrich 99.9%, and/or Ti, Aldrich 99.9%), were ground together using an agate pestle and mortar. Grinding creates a homogeneous mixture of reactants and reduces particle size, which increases the reaction rate. The reactants were then placed in a carbon crucible and this was then placed in a fused silica tube that had been sealed at one end. A tap was attached to the un-sealed end of the tube, it was subsequently removed from the glove box and attached to an Edwards T-Station 75 turbo pump and evacuated. When the pressure reached ~ 8 x 10^{-5} mbar the tube was sealed using an oxygen-methane blow torch. The sealed tube was then heated in a Lenton ECF chamber furnace. As sulphur sublimes at ~ 100 ^{o}C at the low pressure found in the sealed tube, all reactions were solid-gas reactions. Due to the gaseous sulphur several safety measures had to be in place to ensure the tubes did not burst due to a build-up of pressure. First, only moderate amounts of reactants (~ 0.5g) were placed in each tube, and secondly, a slow heating rate was used. Details

of specific temperatures and heating rates used are discussed on the relevant sections in Chapters 3 and 4. On completion of the heating cycle, sealed tubes were transferred into an argon filled glove box and carefully opened using a glass-cutting knife.

2.1.2 Resorcinol - Formaldehyde gel synthesis

The lithium-rich mixed metal oxide cathode materials discussed in Chapter 5 were synthesised using a resorcinol-formaldehyde gel (RF-gel) synthesis. The key to this synthesis is the fact that when mixed and heated, resorcinol (1,3-dihydroxybeneze) and formaldehyde gel together to form an aerogel[1] (a synthetic light weight material based on a gel where the liquid component has been replaced by a gas). Aerogels have many useful properties including low density and low thermal conductivity The aerogel properties of RF-gels have seen them used in a wide range of applications, including as low thermal conducting materials[2] and gas filters[3]. More recently their ability to control the morphology of mesoporous carbon has also been observed[4,5]. It has been demonstrated in previous work by this research group that R-F gels can be used to form high performance cathode materials. The materials synthesised in the past include $Li(Ni_{0.5}Mn_{1.5})O_4$[6] and $LiNi_{1/3}Mn_{1/3}Co_{1/3}O_2$[7].

In the gelation process the RF-gel is formed by base catalysed polymerisation of resorcinol with formaldehyde. The resorcinol acts as the monomer unit and adds formaldehyde in the 2, 4 and 6 ring positions, positions 1 and 3 are already occupied by hydroxyl groups – which increase the reactivity of the monomer[1]. The substituted resorcinol units agglomerate together to form clusters in solution. Li_2CO_3 was used as the catalyst, this ensures that the solution is basic and also controls the cluster size[1]. The $–CH_2OH$ groups on the surface of the clusters lead to further reaction and ultimately polymerisation. After polymerisation is complete the solution in the pores of the gel (water) is replaced by CO_2 in the drying process and the Aerogel is formed[1].

One of the advantages of the RF-gel synthesis is its one-pot nature and the relatively quick reaction time. A general synthesis is outlined below; specifics are covered in the appropriate sections in Chapter 5. Appropriate stoichiometric ratios of metal compounds (e.g. acetates or nitrates, all Aldrich) are dissolved in distilled water. In a separate beaker resorcinol (Aldrich 99.0%) and lithium carbonate (Aldrich, 99.997%) are dissolved in a formaldehyde-water solution (Aldrich, 37 wt. %). When the solids in both beakers are dissolved the contents are combined and stirred at 60 ^{o}C. As heating the formaldehyde solution can result in evaporation of formaldehyde, which is toxic, all reactions should take place in a fume hood. Heating the mixture results in the formation of a resorcinol-formaldehyde solution, this contains chelated dissolved metal particles. Once the gel has formed it is dried overnight at 90 ^{o}C to remove any residual formaldehyde. The gel is subsequently calcined at 200 ^{o}C, this results in the burning off of the organic framework and the gel is reduced to a dark powder. The final heating step, details of which can be found in Chapter 5, results in the desired lithium-rich mixed metal oxide.

The structure of the RF-gel, and therefore the morphology and properties of the metal oxide product, is strongly dependent on the ratios of resorcinol to formaldehyde (R/F), catalyst (R/C) and water (R/W). The final heating step also has an impact on the electrochemical properties of the material.

2.2 Diffraction Techniques

2.2.1 Powder X-ray Diffraction

Powder X-ray diffraction (PXRD) is the technique most commonly used to structurally characterise solid state materials. It is a none-destructive technique that is capable of obtaining qualitative and quantitative phase analysis data. The general principle of the technique is that a monochromatic beam of X-rays is focused on and diffracted from a sample. How the X-rays are diffracted can be analysed to give information about the crystal structure of the sample.

All of the X-ray diffraction carried out in this thesis was performed using a laboratory X-ray diffractometer, as opposed to a synchrotron source. X-rays are formed by striking a metal anode (generally copper, iron or molybdenum) with electrons. This is done by heating a tungsten filament under vacuum, which produces electrons, and ensuring there is a potential difference between the filament and the anode target, which accelerates the electrons into the metal anode. The most intense lines of X-ray radiation emitted from the metal anode are due to the $2p \rightarrow 1s$ transition, this is labelled Kα. X-ray diffractometers use monochromators to filter out other transitions (e.g. $3p \rightarrow 1s$) and this ensures the beam is monochromatic. The identity of the metal used as the anode has an effect on the wavelength of X-ray produced. Copper is the most commonly used anode source, due to the high intensity X-rays it produces, however, Cu $K\alpha_1$ (λ = 1.5405 Å) can excite the electrons in manganese and iron which results in fluorescence and subsequently a high background in the diffraction pattern. For samples that include manganese and iron it can be beneficial to use a X-ray source like Fe $K\alpha_1$ (λ = 1.9360 Å), which produces X-rays with a longer wavelength but does not have issues with fluorescence for these elements, even though it is a less intense X-ray source than copper.

The monochromatic X-ray beam interacts with the electrons in the sample and is diffracted. The diffracted X-rays are scattered from an atomic plane in the material and the resulting diffracted radiation can interfere either constructively or destructively. This is dependent on the phase shift between the two waves and this phenomenon is only possible if the incident beam's wavelength of the X-ray radiation is of the same order of magnitude as the inter-atomic distances within the crystal to study (e.g. ~ 1 Å).

Each plane has a unique angle at which the X-ray beam will interfere constructively. These must satisfy Bragg's law:

$$n\lambda = 2d \sin\theta \qquad 2.1$$

Equation 2.1: Bragg's Law - n = an integer, λ = wavelength of incident radiation, d = distance between planes of atoms and θ = angle of incidence.

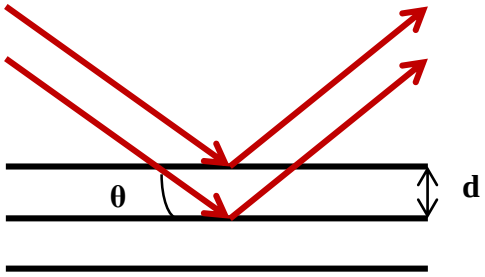

Figure 2.1: Schematic demonstrating Bragg's Law

The angles that satisfy the Bragg equation vary as a function of the crystal structure of the material analysed and in the interplanar distance d. The diffraction of the beam results in concentric rings of varying intensities which can be sampled to produce the peaks seen in X-ray diffraction patterns. The angle at which the reflections occur can be used to extract information on the unit cell parameters. The intensity of the peaks allows information about the unit cell composition to be determined. As the X-ray beam is diffracted by electrons the strength of scattering from a particular element is highly dependent on the number of electrons in that element. This makes it challenging to ascertain information about the position and occupancy of light elements like lithium.

X-ray diffraction measurements on the lithium sulphide materials detailed in Chapters 3 and 4 were carried out on a Stoe STADI/P diffractometer with a CuKα_1 radiation source. As the sulphide materials are air sensitive, samples were loaded into capillaries in an argon filled glove box; the capillaries were then sealed with silicone rubber. The measurements were run with a Debye-Scherrer setup. While routine measurements could be carried out in 90 minutes, to improve the signal to noise ratio, overnight measurements were required for better quality data used for structural refinements.

Measurements on the lithium-rich mixed metal oxides outlined in Chapter 5 were performed on a Stoe STADI/P instrument with an iron radiation source. This is because the mixed metal oxides contained manganese and cobalt, both of which fluoresce when measurements are conducted using a copper source. Samples were not air-sensitive so were handled under ambient atmosphere, a small amount of material was placed between two pieces of polyethylene sheet and sealed with vacuum grease.

2.2.2 Neutron diffraction

Neutrons are uncharged subatomic particles with a mass of 1.66×10^{-27} kg. They can be used as an alternative to X-ray radiation for diffraction experiments because they have a wavelength between 0.5 and 3 Å, depending on the energy of the neutron, similar to the interlayer separation in solid state materials. Unlike X-rays, neutrons do not interact with the electron cloud of each atom, but instead interact with the atomic nuclei. While the X-ray scattering cross-section of an atom was proportional to the number of electrons in an atom, there is no correlation between neutron scattering and atomic number. This gives neutron diffraction several advantages over X-ray diffraction. Firstly, it allows for the detection of light elements like hydrogen and lithium that are virtually invisible to X-rays. Secondly, it is possible to distinguish between atoms that have a similar number of electrons, e.g. Ni^{2+} and Co^{2+}. Finally different isotopes of the same metal, e.g. Ni^{58} and Ni^{60}, have differing neutron scattering factors and can be differentiated. The precise factors that govern the neutron scattering factor are complicated and are beyond the scope of this thesis. Neutron beams are of a lower intensity compared to X-ray beams and therefore larger amounts of materials are needed for measurements.

All the neutron measurements in this thesis were conducted at the ISIS facility at the Rutherford Appleton Laboratory (RAL) in Didcot, UK. The ISIS facility is a spallation source. This involves the firing of high-energy protons at a heavy-metal target (e.g. tungsten) and the protons

hit the nuclei and eject high-energy neutrons. The neutrons are actually too high energy to be used and need to be slowed down by a moderating material (e.g. liquid methane, water, hydrogen). Different moderating materials produce different distributions of wavelengths and this property can be used for various applications. The beam of high energy protons is pulsed and this results in the beam of neutrons produced also being a series of discrete pulses. This can be exploited by measuring the wavelength by time-of-flight techniques, thus avoiding the wastage incurred by selecting individual wavelengths with a monochromator. Different d-spacings are measured at constant θ. To ensure the highest possible count rate there are several banks of detectors at various angles around the sample to allow access to a large number of possible d-spacings.

Room temperature time-of-flight powder neutron diffraction data is presented in Chapters 3, 4 and 5. The data presented in Chapters 3 and 4 was collected using the POLARIS high-intensity, medium resolution instrument at ISIS. Half of the data presented in Chapter 5 was also collected on POLARIS, while the other half was collected using the GEM high-intensity, medium resolution instrument.

Samples were packed into 2 mm quartz capillaries, as most of the samples were air-sensitive they were prepared in an argon filled glove box and sealed with silicone rubber. Capillaries were filled with ~ 4 cm of material as that is the height of the neutron beam at ISIS. The capillaries were then lowered into the beam and measurements would typically take 4 – 5 hours, depending on how strongly the material scattered the neutron beam.

2.2.3 Rietveld Refinements

The major limitation of powder X-ray diffraction and powder neutron diffraction is the compression of 3-dimensional data into 1-dimension. This results in a loss of information due to the overlapping of *hkl* reflections with the same d-spacing. Rietveld refinement is a method

of fitting powder diffraction data to a particular structural model to correct for this issue[8]. The Rietveld profile refinements shown in Chapters 3 and 4 were performed using the GSAS[9] suite of programmes and the EXPGUI[10] interface. The refinements of the neutron diffraction data presented in Chapter 5 were carried out by Dr. A.R. Armstrong at the University of St Andrews using TOPAS Academic[11].

The refinement method consists of comparing the experimental data to a given structural model. International tables (e.g. Inorganic Crystal Structure Database - ICSD) are generally used to give the values for the reference model. Parameters provided from the tables are optimised until the calculated pattern fits with the experimental data, by changing the atomic positions, thermal constants, occupancies, lattice parameters and peak profile parameters using a non-linear least squares technique, the equation of which is:

$$S = \sum_i w_i \left(y_i(obs) - y_i(calc)\right)^2 \qquad 2.2$$

Equation 2.2: The non-linear least squares technique - S = difference between observed and calculated intensities, w_i = weighting factor, $y_i(obs)$ = observed intensity of the data at the ith step and $y_i(calc)$ = calculated intensity at the ith step of the model.

This allows for the accurate determination of these parameters and also the percentage of different phases present in a solid solution.

One of the atomic parameters refined is the thermal parameter of each atom. The Debye-Waller factor, B_{iso}, is used to determine the atomic displacement and describes the thermal motion of each atom. B_{iso} is related to another thermal parameter U_{iso} by the following equation:

$$B_{iso} = 8\pi^2 \langle {U_{iso}}^2 \rangle \qquad 2.3$$

Equation 2.3: The relationship between the the Debye-Waller factor, B_{iso}, and U_{iso}.

The thermal parameter reported is dependent on the software used to carry out the refinement: GSAS gives the thermal parameter in terms of U_{iso}, while TOPAS gives it in terms of B_{iso}.

The refinement software minimises the value of S (equation 2.2) and the fit between model and experiment is monitored with a number of parameters. R_p is the profile factor, R_{wp} is the weighted profile factor (calculated from the Bragg contribution to the diffraction pattern) and χ^2 is a universal 'goodness of fit' parameter. The parameters are defined mathematically in the equations below, the terms defined in Equation 2.2 are not defined again here:

$$R_p = \frac{\sum_i |y_i(obs) - y_i(calc)|}{\sum_i y_i(obs)} \qquad 2.4$$

Equation 2.4: The Profile Factor, R_p.

$$R_{wp} = \left(\frac{\sum_i w_i \left(y_i(obs) - y_i(calc)\right)^2}{\sum_i w_i y_i(obs)^2} \right)^{\frac{1}{2}} = \left(\frac{S}{\sum_i w_i y_i(obs)^2} \right)^{\frac{1}{2}} \qquad 2.5$$

Equation 2.5: The Weighted Profile Factor, R_{wp}.

$$\chi^2 = \frac{\sum_i w_i \left(y_i(obs) - y_i(calc)\right)^2}{N - V + C} = \frac{S}{N - V + C} \qquad 2.6$$

Equation 2.6: Universal 'goodness of fit' Parameter, χ^2 - N = number of observations, V = number of independent variable and C = number of constraints.

The difference between the calculated model and experimental data is also compared visually using a difference curve plotted below the x-axis.

2.3 Scanning Electron Microscopy

Scanning Electron Microscopy (SEM) is a technique used to observe the morphology of materials on the nanometre and micrometre scales. The method allows for observations of particle size and shape, surface features and structure, and the porosity of the material.

An electron beam is accelerated across a potential difference and focused on the surface of the sample. Typically the electron beam is emitted from a tungsten filament cathode, a lanthanum

hexaboride (LaB_6) wire, or a field emission gun (a type of electron gun where an emitter is held at a negative potential relative to a nearby electrode and the potential difference at the emitters surface leads to field electron emission). The images used in this thesis were collected using a field emission gun, which produces a smaller diameter beam with greater current density compared to traditional tungsten or LaB_6 sources, this results in superior image quality.

When the electron beam interacts with the sample, electrons and electromagnetic radiation are emitted and they are detected by an analyser. The emitted electrons consist of several different kinds of electron: backscattered primary electrons, auger electrons and secondary electrons formed in multiple inelastic scattering processes. Secondary electrons make up the vast majority of the emitted electrons and are the electrons used to form the images in the SEM images used in this thesis. When the secondary electrons reach the detector a current is produced and recorded. The current is plotted against the probe position on the surface of the sample and an image is produced. The contrast in the resultant image is dependent on multiple factors but the most significant is the surface morphology, therefore the image produced can be considered a direct image of the surface structure.

SEM images in the following chapters were carried out using a Carl Zeiss Merlin FEG instrument. Samples were loaded on to aluminium SEM stubs using copper tape. For air sensitive samples this was carried out in an argon filled glove-box and they were then transported to the instrument under an argon atmosphere and quickly purged into the instrument.

2.4 X-ray Absorption Near Edge Spectroscopy

In X-ray absorption near edge spectroscopy (XANES) X-ray radiation is used to monitor the excitation of core level electron in a sample. This electron is excited to a higher electronic state below the ionisation threshold or emitted as a photoelectron, either way an excited state is

formed. The excited state then relaxes by filling the core hole by an Auger process or by capture of an electron from another shell followed by emission of a fluorescent photon. Different core electrons have discrete binding energies, therefore different energy X-rays are needed to excite the electron. A plot of X-ray absorbance as a function of energy can be formed for a specific element. A generic example of this can be seen in the figure below.

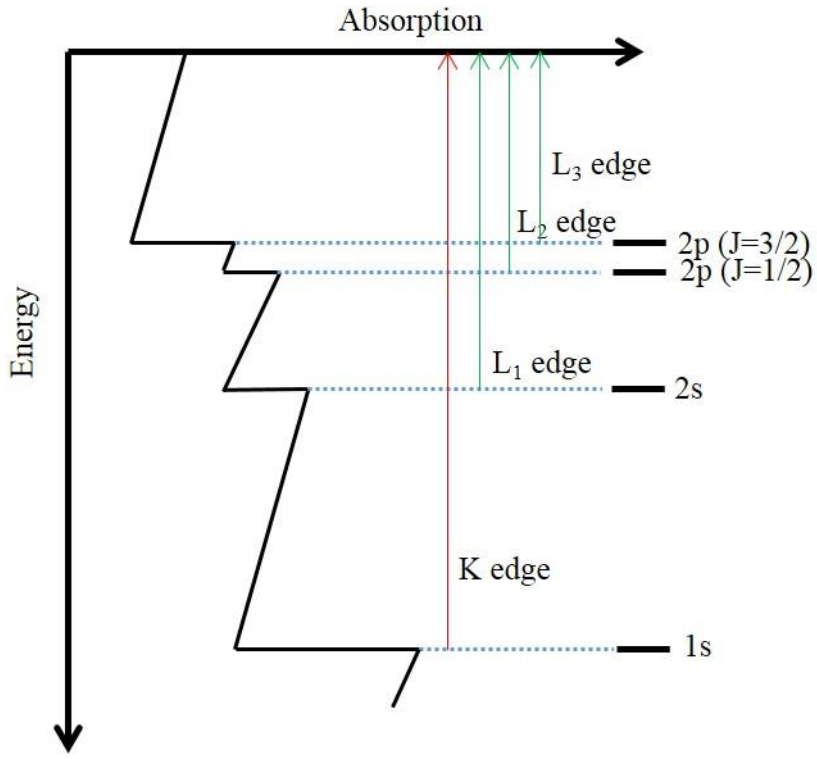

Figure 2.2: Schematic of an X-ray absorption spectrum.

When a core electron is excited an 'edge' appears in the X-ray absorption spectrum at a characteristic energy that corresponds to the element that is excited. The name the absorption edge is given depends on the principle quantum number of the excited electron, e.g. the K edge corresponds to n = 1 and the L edge corresponds to n = 2.

In reality the absorption edges are not just an abrupt increase in absorption energy seen in Figure 2.2 but have a much more complex structure that can be analysed to give more information about the analysed material. Figure 2.3 gives a more detailed schematic of a generic K edge.

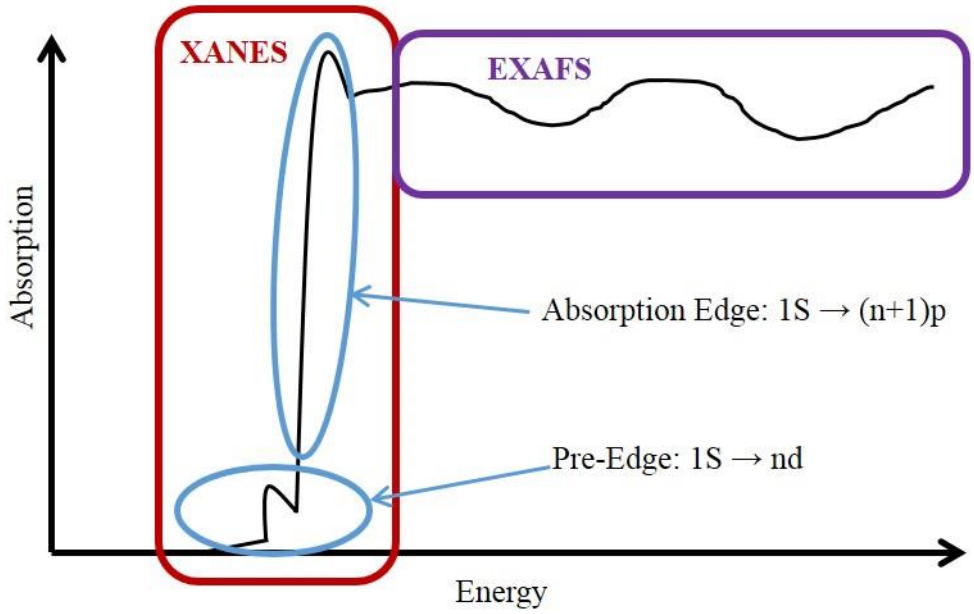

Figure 2.3: Schematic of generic K edge showing XANES and EXAFS regions.

The structure and features in the vicinity of the absorption edge (generally 50 eV) is the X-ray Absorption Near Edge Structure (XANES) and the region after this is the Extended X-ray Absorption Fine Structure (EXAFS). XANES directly monitors the angular momentum of the unoccupied electronic states and must obey the electric dipole selection rules: $\Delta l = +/- 1$, $\Delta j = +/- 1$ and $\Delta s = 0$. The weak transitions below the absorption edge are referred to as pre-edge structures and are due to mixing of p and d orbitals and therefore formally forbidden transitions may be observed. The oscillating appearance of the EXAFS region is due to constructive and destructive interference between the outgoing and back-scattered photoelectron waves.

XANES and EXAFS can be used to understand many structural properties of a material. The energy of the edge is dependent on the oxidation state of the element tested. The edge shifts to higher energy as the oxidation state is increased. The pre-edge region contains information concerning the local geometry around the absorbing element and features after the edge contain information on the atomic position of neighbouring atoms. Unlike X-ray photoelectron spectroscopy (XPS), which only gives information on the surface of the sample, XANES gives information on the bulk of the sample. This is especially useful for analysis of cycled battery

material when the surface of the electrode may be covered with an SEI-layer that obscures the electrode from XPS analysis.

The XANES experiment detailed in Chapter 4 was carried out at the Diamond Light Source at the Rutherford Appleton Laboratory (RAL) in Didcot, UK. The experiment was run by and the data processed by Professor A.V. Chadwick and co-workers at the University of Kent and is concerned with the K edge of vanadium and titanium.

2.5 Electrochemistry

2.5.1 Electrode Fabrication

The electrodes fabricated over the course of this project consisted of three components: the active material being electrochemically tested, a carbon additive used to increase the conductivity of the electrode and a binder used to help keep the electrode together on cycling. The carbon additive used is Super S carbon which has a density of 0.16 gcc^{-1} and an average particle size of 45 nm. Kynar Flex 2801, a copolymer based on polyvinylidene fluoride (PVDF), is the binder used. The ratio of these three components varies depending on the identity of the active material and is covered in the individual results chapters.

Two different methods of electrode fabrication will be discussed in the following chapters. The first method is to use pellet electrodes. The active material and carbon additive are ground together using an agate pestle and mortar. When sufficiently mixed the binding agent is added to the mixture and also ground together. A small amount of mixed material was then pressed into a pellet using a die set. Pellet electrodes were typically 0.2 mm thick.

The second method of electrode fabrication is to cast the electrode on to metal foil. Active material, carbon and binder are mixed and placed in a glass vial with a magnetic stirring bar. Dry tetrahydrofuran (THF) is added and the resultant mixture stirred, this dissolves the Kynar binder and forms a slurry. The metal foil is pre-treated by first having its surface roughened (by

using a clean scouring pad) and then a pre-casting layer of binder in THF is applied using a doctor blade. The pre-treatment helps to ensure good adhesion between the metal foil and the electrode. After the pre-casting layer is dry the prepared slurry is cast on the foil using a doctor blade. Once the casting has been performed the foil is left to dry in ambient atmosphere and then dried under vacuum overnight. Once the electrodes are dry they are punched out of the foil using a hand punch. Anode materials were cast on copper foil, while cathode materials were cast on aluminium foil. The use of aluminium foil is preferable as it is thicker and easier to handle, but also lighter, which reduces the weight of a cell – an important commercial consideration. However, it is electrochemically active at low voltages vs lithium and therefore cannot be used for anode materials.

Cast electrodes are thinner (typically 0.1 mm) and this tends to result in superior electrochemical performance compared to pellet electrodes. Pellet electrodes use more material and are therefore useful when 'post-mortem' analysis is necessary. If the material was air-sensitive both of the above procedures were carried out in an argon filled glove-box.

2.5.2 Cell fabrication

2.5.2.1 Coin Cells

The vast majority of the electrochemical data presented in the coming chapters was collected using coin cells. The process of coin cell assembly was the same regardless which of the two methods of electrode preparation discussed above were used. Coin cells were assembled from CR2325 coin cell parts that were purchased from the National Research Council of Canada and cells parts were pressed together using a hydraulic argon press in an argon filled glove-box. The figure below depicts a typical coin cell, for half-cells the counter electrode is lithium foil and for full-cells it is a cathode material, see Chapter 6 for more details.

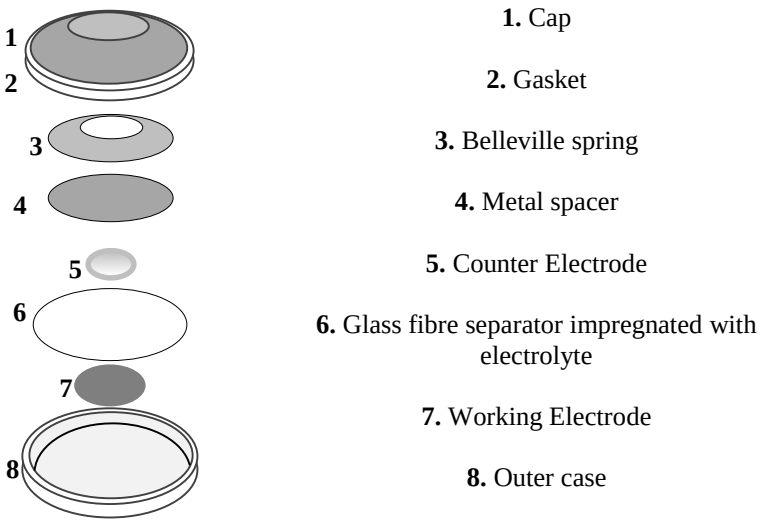

Figure 2.4: Schematic of the components of a coin cell.

2.5.2.2 Three electrode Swagelok Cells

Three electrode cells contain a reference electrode as well as a working and counter electrode. In the experiments carried out in Chapter 6 lithium was used as the reference, a sulphide anode material as the working electrode and an oxide cathode material as the counter. This allows for the voltage of both the anode and cathode to be monitored relative to lithium independently of each other. This is useful for full-cells, as in a two electrode system the observed voltage is the combination of the anode and cathode and it is not always clear what voltage the individual electrodes are operating at. Customised Swagelok parts were used so that at one end of the cell the reference electrode was placed next to the working electrode.

2.5.3 Important electrochemical terminology

Over the course of this thesis different electrochemical terms are used. The following section gives a brief overview of the most common terms.

In a rechargeable electrochemical cell chemical energy, the Gibbs energy corresponding to the cell reaction, is converted into electrical energy during discharge and subsequently converted back again when the cell is charged. The relationship between the electrical charge passed and

the chemical reactants in a reversible electrochemical reaction of form Ox + ne^- ⇌ Red, is governed by **Faraday's Law**:

$$Q = zF\frac{m}{M} \qquad 2.7$$

Equation 2.7: Faraday's Law – Q: the total electric charge passed (Ah), z: the number of electrons, F: the Faraday constant (96487 $Cmol^{-1}$/26.8 $Ahmol^{-1}$), m: mass of material involved in the electrochemical process (g) and M: molecular weight of the material ($gmol^{-1}$).

In an electrochemical cell a **potential difference** is observed between the anode and cathode immersed in the same electrolyte. The potential difference can be defined by the following equation:

$$\Delta E = -\frac{\Delta G}{nF} \qquad 2.8$$

Equation 2.8: Potential difference – ΔE: equilibrium potential difference, ΔG: change in Gibbs free energy for the overall cell reaction, n: number of electrons involved in the process and F: the Faraday constant (96487 $Cmol^{-1}$)

The amount of electrical charge that a battery can store is termed its capacity. The **theoretical capacity** for an electrode material can be calculated using Equation 2.9:

$$Q_{th} = \frac{nF}{3.6M} \qquad 2.9$$

Equation 2.9: Theoretical capacity – Q_{th}: theoretical capacity ($mAhg^{-1}$), n: n: number of electrons involved in the process and F: the Faraday constant (96487 $Cmol^{-1}$) and M: molecular mass ($gmol^{-1}$). Dividing by 3.6 convert to the commonly used units of $mAhg^{-1}$.

The above equation demonstrates that capacity is increased by increasing the number of electrons taking part in the electrochemical process and by reducing the molecular mass of the electrode material.

Due to practical considerations the theoretical capacity is virtually never obtained. The observed capacity is termed the **specific capacity** and represents the quantity of charge involved in the electrochemical reaction per mass unit:

$$Q_{sp} = \frac{It}{m} \qquad 2.10$$

Equation 2.10: Specific capacity – Q_{sp}: Specific capacity ($mAhg^{-1}$), I: current passed (mA), t: charging/discharging time (h) and m: mass of active material participating in the reaction (g).

The reversibility of a material can be described by its **coulombic efficiency**. It represents the ratio of the charge capacity and the discharge capacity and if this is 1 the process is completely reversible.

The **capacity retention** (also called cyclability) of a battery describes the loss of capacity on cycling. It is usually stated as a function of a certain number of cycles, by comparing the value of discharge capacity after n cycles and the value obtained at the first cycle.

For many applications it is desirable for a battery to charge and discharge quickly. **Cycling rate** can be expressed two ways: in terms of charge stored/released per unit mass ($mA\ g^{-1}$) or as a measure of the rate at which a battery is discharged relative to its maximum capacity (C-rate). C-rate is inversely proportional to the time taken for the cell to fully charge/discharge, i.e. C-rate indicates 1 hour, a rate of 2 C indicates 0.5 hours and a rate of C/5 indicates 5 hours.

2.5.4 Galvanostatic Cycling

Galvanostatic cycling was used for all electrochemical measurements in this thesis. Galvanostatic measurements are carried out by applying a constant current to a battery and measuring its response in terms of potential as a function of time. Upper and lower potential cut-offs are selected and used as the limits of the measurement and the cell will cycle between these limits a predetermined number of times.

When a positive current is applied the potential of the cell increases and it is being charged. Inside the cell the working electrode is oxidised and lithium ions are extracted, this continues until the upper voltage cut-off is reached. The reverse process then takes place as a negative current is applied and the working electrode is reduced and the cell potential decreases until

reaching the lower voltage cut-off. The data produced from this process is plotted as the variation of the potential (V) and either time (hours) or specific capacity ($mAhg^{-1}$, calculated using Equation 2.10 above), and is generally referred to as a load curve. The charge and discharge curves should be symmetrical and stackable when the process is fully reversible, however, in reality this is virtually never the case. This is due to a variety of factors, including Ohmic loss (a voltage decrease due to the resistance of cell components), the work function at the solid electrolyte interface and the resistance to ion transfer through the electrolyte. The result is a difference between the potential of charge and discharge; this is termed the polarisation of the cell.

It is possible to infer the mechanism of lithium intercalation/deintercalation from the shape of the load curve produced. This is done by applying Gibbs' phase equation:

$$f = C - P + 2 \qquad 2.11$$

Equation 2.11: Gibb's phase equation – f: number of degrees of freedom, C: number of independent components and P: number of separate phases

Many intercalation reactions can be considered as a binary system (C = 2), consisting of the lithium rich and lithium poor components. Therefore, if intercalation occurs via a two phase mechanism (P = 2) the number of degrees of freedom, f, will be zero, and all variables (including voltage) will be fixed. This results in the voltage being constant for the intercalation/deintercalation process and a flat plateau is produced in the load curve. However, if the electrochemical process occurs via a single phase mechanism (P = 1) there is now a degree of freedom and the potential of intercalation may vary and a sloping voltage profile (pseudo-plateau) is observed in the load curve.

The profiles of curves obtained by galvanostatic measurements give information on what reactions are occurring; each plateau or pseudo-plateau corresponds to a reaction step. The determination of the potential at which a plateau takes place at is not always clear. This can be

remedied by plotting the derivative of the curves, giving a differential capacity plot. Each reaction now corresponds to a peak in a plot, like in cyclic voltammetry. This allows easy comparison between different cycle numbers of a battery, or between different materials. The equation used to calculate the derivative curves is

$$\frac{\delta Q}{\delta E} = \lim_{n \to 0} \frac{Q(a+n) - Q(a)}{E(a+n) - E(a)} \qquad 2.12$$

Equation 2.12: Equation to calculate derivative curves – Q: specific capacity and E: potential.

2.6 References

1 Pekala, R. W. *J. Mater. Sci.* **24**, 3221-3227 (1989).
2 Pekala, R. W., Alviso, C. T., Lu, X., Gross, J. & Fricke, J. *J. Non-Cryst. Solids* **188**, 34-40 (1995).
3 Kong, F. M., Lemay, J. D., Hulsey, S. S., Alviso, C. T. & Pekala, R. W. *J. Mater. Res.* **8**, 3100-3105 (1993).
4 Lu, A. H., Hao, G. P., Sun, Q., Zhang, X. Q. & Li, W. C. *Macromol. Chem. Phys.* **213**, 1107-1131 (2012).
5 Al-Muhtaseb, S. A. & Ritter, J. A. *Adv. Mater.* **15**, 101-+ (2003).
6 Shaju, K. M. & Bruce, P. G. *Dalton Trans.*, 5471-5475 (2008).
7 Shaju, K. M. & Bruce, P. G. *Adv. Mater.* **18**, 2330-+ (2006).
8 Rietveld, H. M. *J. Appl. Crystallogr.* **2**, 65-& (1969).
9 Larson, A. C. & Von Dreele, R. B. (2000).
10 Toby, B. H. *J. Appl. Crystallogr.* **34**, 210-213 (2001).
11 Coelho, A. A. *J. Appl. Crystallogr.* **33**, 899-908 (2000).

Chapter 3: $LiVS_2$ as an Anode Material for Lithium-ion Batteries

3.1 Introduction

This chapter is concerned with $LiVS_2$ as a potential anode material for Li-ion batteries.

As discussed in Section 1.3 there is a need for an anode material that operates at potentials between those of graphite (~ 0.1 V vs Li^+/Li^0) and $Li_4Ti_5O_{12}$ (~ 1.6 V vs Li^+/Li^0) at approximately 1 V. Graphite has issues with safety[1-3] due to lithium plating on the electrode surface and $Li_4Ti_5O_{12}$ has a high voltage for lithium deinsertion which compromises cell potential in full cells[4]. There is also growing concern about $Li_4Ti_5O_{12}$ relating to gas evolution at elevated temperatures[5]. $LiVS_2$ on the other hand intercalates lithium at ~ 1.0 V vs Li^+/Li^0 making it of interest as a 1 volt intercalation anode[6].

However, the previously reported performance of $LiVS_2$ is poor[7,8]. At a slow rate of 15 mAg^{-1} intercalation of Li^+ takes place at ~ 1.0 V and deintercalation at ~ 1.3 V, i.e. a polarisation of ~ 0.3 V. Despite operating at the limit of where electrolyte reduction begins $LiVS_2$ still displays a first cycle irreversible capacity loss of ~70 $mAhg^{-1}$, roughly 30% of the theoretical capacity – 220 $mAhg^{-1}$. A capacity of 200 $mAhg^{-1}$ was reported by J.B. Goodenough and co-workers reported on the 2nd discharge. However, a capacity fade of over 1 $mAhg^{-1}$ per cycle was observed, significantly more than seen in $Li_4Ti_5O_{12}$ electrodes. Published data also shows that capacity drops very significantly with increasing rate: 200$mAhg^{-1}$ at 0.1 C to ~ 100 $mAhg^{-1}$ at C rate.

Over the course of this chapter previously reported work on $LiVS_2$ will be reproduced and optimised to judge if $LiVS_2$ has a future as an anode material.

3.2 Synthesis

$LiVS_2$ was synthesised via the sealed tube method outlined in Section 2.1.1. This is a standard method of synthesising sulphides[9] and was how this material had previously been synthesised by J.B. Goodenough and co-workers[8]. Stoichiometric amounts of lithium sulphide (Li_2S), sulphur (S) and vanadium metal (V) were placed in a sealed silica tube. The tube was heated at a ramp rate of 1 $^oC\ min^{-1}$ to 750 ^oC and held there for 3 days. The reaction was then cooled to 300 ^oC at a rate of 1.5 $^oC\ min^{-1}$ and then removed from the furnace. Heating times of less than 3 days resulted in peak splitting in X-ray powder diffraction pattern that implied a non-pure phase material. No change in either PXRD or electrochemical performance was observed by repeated heating so only one firing sequence was performed. $LiVS_2$ is moisture sensitive and was handled in an argon filled glovebox at all times.

3.3 Powder X-ray Diffraction (PXRD)

Powder X-ray diffraction was carried out using a Stoe STADI/P diffractometer with a Cu $K\alpha_1$ X-ray source operating in capillary mode as $LiVS_2$ is air sensitive. As can be seen in Figure 3.1, excellent agreement was found between synthesised samples and data from the literature.

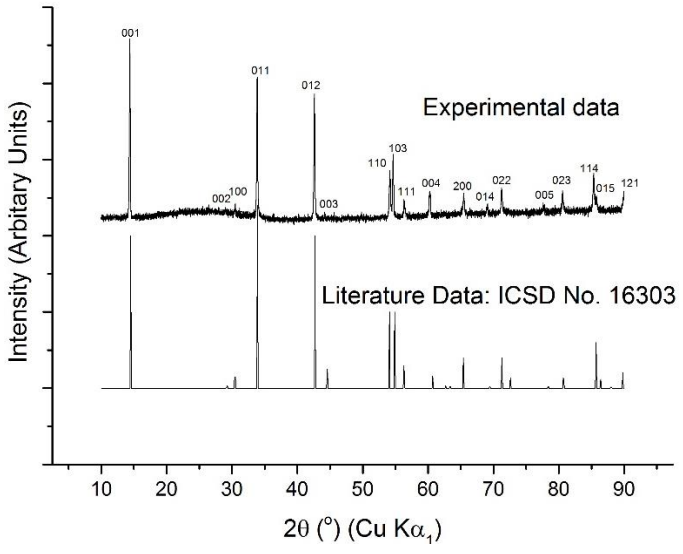

Figure 3.1: Comparison of PXRD pattern for synthesised $LiVS_2$ and data from the literature[10].

The small halo feature seen between 20° and 30° is due to the amorphous glass capillary. There are some slight differences between the intensities in the diffraction pattern of the synthesised sample and the previously reported diffraction pattern. This could possibly be due to different amounts of lithium occupancy in the system. While the material is usually denoted as stoichiometric $LiVS_2$ it is always found to be slightly lithium deficient, and the magnitude of this deficiency can vary depending on synthetic conditions. The data in the ICSD database used in Figure 3.1 is from the 1970s and was produced from a sample that was synthesised by heating V_2O_5 and Li_2CO_3 under a flowing atmosphere of H_2S, no details about lithium occupancy are given in the paper[10]. Goodenough and co-workers estimated the composition to be $Li_{0.8}VS_2$ and $Li_{0.85}VS_2$ in different publications; in both cases this was inferred from the electrochemistry[7,8]. However, given the negligible X-ray scattering power of lithium it is unlikely that small difference in lithium occupancy would be observable in the X-ray diffraction patterns. An alternative explanation for the difference in peak intensities between the literature and the data presented here is preferred orientation. $LiVS_2$ is a layered material (Section 1.3.3.6) and preferred orientation is often observed in X-ray diffraction patterns of layered materials[11]. When the X-ray sample is prepared layered materials tend to stack along the c-axis and this can increase the intensities of (00L) reflections relative to other reflections. The precise amount of preferred ordination will vary from sample to sample and therefore small discrepancies in peak intensities will be observed.

In order to confirm that the synthesised material was pure phase and to obtain accurate lattice parameters the PXRD patterns were refined using the Rietveld method. The literature structure of $LiVS_2$ was used as the starting model and the model was refined against the data giving a good agreement of $\chi^2 = 1.075$. The difference plot and tables can be seen below:

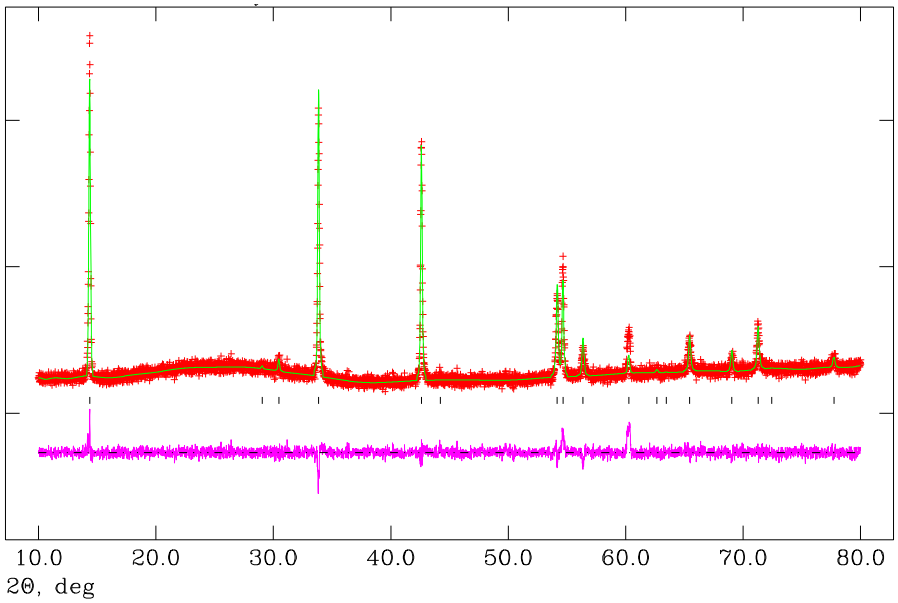

Figure 3.2: Difference plot for Rietveld refinement of PXRD pattern of $LiVS_2$

$LiVS_2$: Space Group		P -3 m 1
Lattice Parameters -	**a**	3.3822(8) Å
	c	6.1373(2) Å
Refinement parameters -	χ^2	1.075
	wR_p	8.52%
	R_p	6.66%

Atom	X	Y	Z	Site Multiplicity	Fractional Occupancy	U_{iso} (Fixed)
Li	0	0	0.5	1	1	0.02
V	0	0	0	1	1	0.02
S	0.3333	0.6666	0.2163(5)	2	1	0.02

Table 3.1: Refinement parameters of PXRD pattern for $LiVS_2$

The refined lattice parameters are in excellent agreement with the literature value of **a** = 3.381 Å and **c** = 6.139 Å. The difference between the experimental data and the model may be due to the occupancy of lithium. In the refinement model this has been fixed as 1, this is because lithium is only a weak scatterer of X-rays (see Section 2.2) and the occupancy could not be accurately refined. As it is very difficult to refine accurate thermal parameters from X-ray data, especially without going to very high angles that were not possible using capillary mode, so the U_{iso} parameters were fixed at a sensible value. In order to obtain an accurate refined occupancy of lithium and thermal parameters powder neutron diffraction was used.

3.4 Neutron Diffraction

Powder neutron diffraction was carried out on the Polaris beamline at the ISIS facility at the Rutherford Appleton Laboratories in Didcot, UK. Figure 3.3 shows the Rietveld refinement difference plot for bank 5 and Table 3.2 shows the refinement parameters.

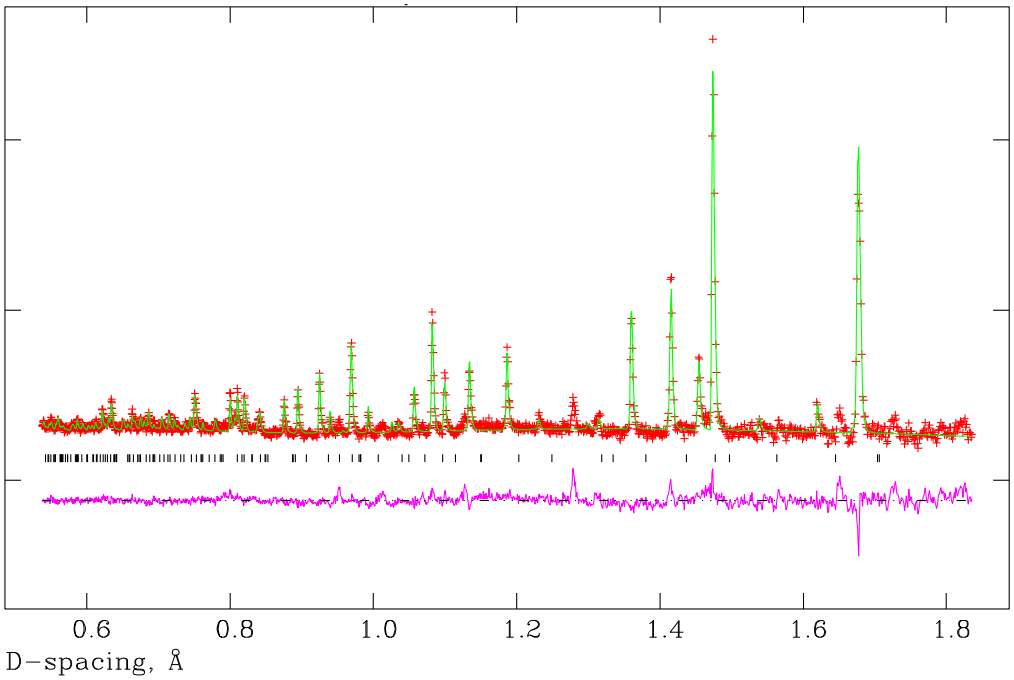

Figure 3.3: Difference plot for Rietveld refinement of PND pattern of $LiVS_2$

$LiVS_2$: Space Group		P -3 m 1
Lattice Parameters -	**a**	3.3566(2) Å
	c	6.1515(4) Å
Refinement parameters -	χ^2	1.163
	wR_p	5.76%
	R_p	6.42%

Atom	X	Y	Z	Site Multiplicity	Fractional Occupancy	U_{iso}
Li	0	0	0.5	1	0.90(5)	0.024(2)
V	0	0	0	1	1	0.001(3)
S	0.3333	0.6666	0.2305(4)	2	1	0.0056(4)

Table 3.2: Refinement parameters of PND pattern for $LiVS_2$

On the whole there is good agreement between the X-ray and neutron data. The primary differences are the neutron data has a slightly smaller **a** lattice parameter and slightly larger **c** lattice parameter, as well as a small difference in the position of the sulphur atoms. These differences could be due to the more accurate nature of neutron diffraction or due to small

differences in different synthesised samples. The neutron sample appears to have extra peaks at ~ 1.28 Å and 1.65 Å, these correspond to a small amount of unreacted Li_2S starting material not detected by X-ray diffraction. The lithium content was refined to be $Li_{0.9}$ which is higher than previously derived electrochemically[7].

3.5 Electrochemistry

Electrochemical measurements were performed in coin cells as described in Section 2.5. Both cast and pelletised electrodes have been used, and the ratio of active material : Super S carbon conductive additive : Kynar 2801 Binder used in electrode fabrication has been explored, both are discussed below. The electrolyte used has also been investigated. For comparison with previously published data cells were initially cycled between 2.2 and 0.8 V vs Li^+/Li^0.

Figure 3.4 below shows the load curves of the 1st, 2nd, 5th and 10th cycles of $LiVS_2$ at the rates of 15 mAg^{-1} and 100 mAg^{-1}. Electrodes consisted of ratio 80 : 10 : 10 by weight of active material : Super S carbon conductive additive : Kynar 2801 Binder, and LP 30, 1 M $LiPF_6$ in 1 : 1 v/v EC : DMC (BASF), was used as the electrolyte .

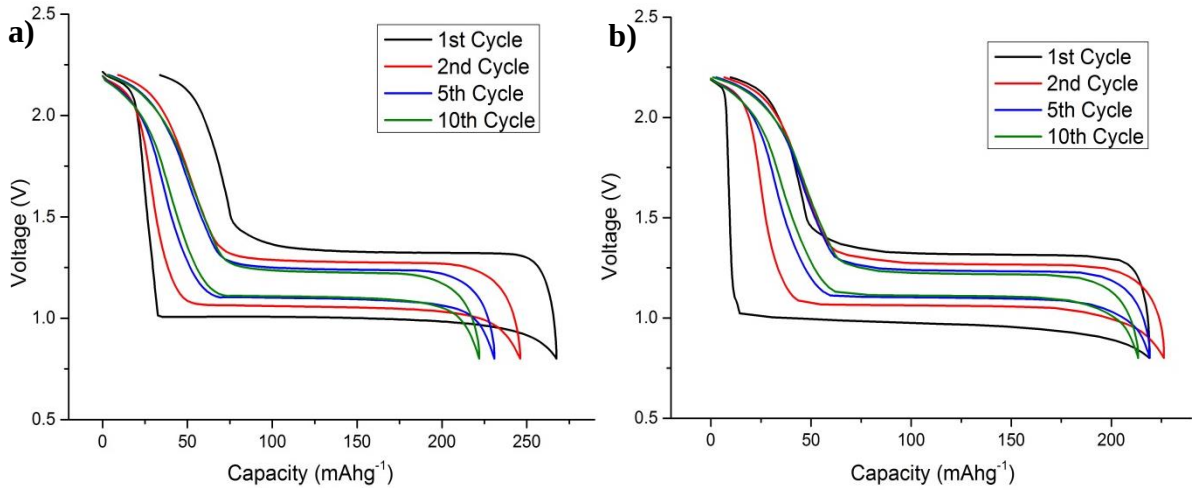

Figure 3.4: Load curves of the 1st, 2nd, 5th and 10th cycle of $LiVS_2$ at a) 15 mAg^{-1} and b)100 mAg^{-1}.

Like previously produced $LiVS_2$, these samples are slightly lithium deficient, as demonstrated by the presence of the plateau at ~ 2.1 V on the 1st discharge, corresponding to the V^{3+}/V^{4+} redox couple and the lithium deficient material becoming stoichiometric. However, the material synthesised here is not as lithium deficient as those reported previously. The 2.1 V plateau is only 15 – 25 $mAhg^{-1}$, depending on sample, which corresponds to $Li_{0.93}VS_2$ – $Li_{0.89}VS_2$, a significantly higher lithium content than the lithium occupancy of 0.8 seen previously[7]. This lithium content derived electrochemically is in excellent agreement with the value refined from the neutron diffraction data in Section 3.4.

Figure 3.4a shows that, at a slow rate of 15 mAg^{-1} (approximately C/15) the plateau corresponding to the first discharge (interaction of Li^+) is at 1.00 V and the first charge plateau (deintercalation of Li^+) is at 1.33 V, resulting in a polarisation of 0.33 V. Polarisation decreases on the second cycle as the voltage for intercalation rises to 1.05 V and the voltage for deintercalation decreases to 1.27 V. This change in voltage continues for the first few cycles, until on the 10th cycle the voltages for intercalation and deintercalation stabilise at 1.10 V and 1.22 V respectively, reducing polarisation to 0.12V. This is all in excellent agreement with previously reported work on $LiVS_2$[7].

The phenomenon of the polarisation decreasing on the first few cycles is not observed in other common two phase electrode materials like $Li_4Ti_5O_{12}$ and $LiFePO_4$[12]. Goodenough and co-workers speculated that the stabilisation of the intercalation voltage is due to the introduction of Li into the tetrahedral sites lowering the energy of the M(III)/M(II) couple by 0.1 V[8]. However, such a large change in polarisation was not observed for $LiTiS_2$ which operates by an identical mechanism[7]. It is possible that formation of the Li_2VS_2 phase introduces defects into the structure. On subsequent cycles these defects result in additional nucleation sites for formation of the Li_2VS_2 phase and the potential for intercalation/deintercalation is altered. Another possible reason for the change is due to the presence of trimers of vanadium in

$LiVS_2$[13,14] that need to be broken when lithium intercalates into the structure and V^{3+} becomes V^{2+}. It is possible that when the lithium deintercalates and the vanadium is oxidised to +3 again the trimers are not reformed to such a degree and after 10 cycles they appear to not be formed at all. Without the need to break or form vanadium trimers the intercalation and deintercalation processes are more similar and the polarisation is reduced. The presence of vanadium trimers has previously been observed by electron diffraction and is connected to the transition to a valence bond state insulator at 305 K, discussion of which is beyond the scope of this thesis[14].

At the faster rate of 100 mAg^{-1} the load curve looks similar, with one significant difference. The plateau corresponding to the first insertion of Li^+ is at a lower voltage (~ 0.95 V) and slopes down, resulting in incomplete insertion of Li^+ and a lower discharge capacity. As the voltage rises on the subsequent cycle more Li^+ is inserted and the capacity on the second cycle is larger than the first. As the rate is increased further this effect is exacerbated and it can take multiple cycles before the maximum capacity is achieved. By the 10^{th} cycle the load curves at different rates look virtually identical apart from differing capacities.

After 5 cycles a significant portion of capacity on both intercalation and deintercalation is above their respective plateaus. This sloping region appears to be fully reversible and could possibly be due to the presence of a single phase solid solution process, however, no solid solution region was observed in X-ray diffraction patterns.

At both rates there is only a small irreversible capacity loss on the first cycle, as would be expected from an anode that operates at this voltage: 0.8 V vs Li^+/Li^0, where only a small amount of SEI layer is expected to form[15]. The irreversible capacity loss is smaller than previously reported samples, partly due to the smaller high voltage plateau on the first discharge, and partly due to the smaller amount of carbon additive used in electrode fabrication. The 10% carbon used here is half the 20% used by Goodenough and co-workers. It is important

to remember that any SEI layer formation will take place on both the active material and the carbon additive. While the carbon additive may make up a small percentage of the weight of the composite electrode, the Super S carbon (or any other carbon additive) has a much higher surface area than the sulphide active material and consequently a substantial amount of SEI layer formation takes place on the carbon surface. Therefore reducing the carbon amount from the 20% previously reported to the 10% results in a significant reduction in the first cycle irreversible capacity loss. $LiVS_2$ is a black/dark grey colour so should be expected to have reasonable electrical conductivity, however, it has been demonstrated previously $LiVS_2$ is an insulator at room temperature[14]. Lowering the amount of carbon additive below 10% resulted in low capacities and the cell failing after several cycles due to loss of electrical conductivity between the electrode and the current collector. This can be seen in Figure 3.5 which shows the charge and discharge capacities of $LiVS_2$ electrodes using various amounts of Super S carbon additive. The Kynar binder amount was fixed at 10%, pellet electrodes were used and the electrolyte was 1 M $LiPF_6$ in 1 : 1 v/v EC : DMC (BASF).

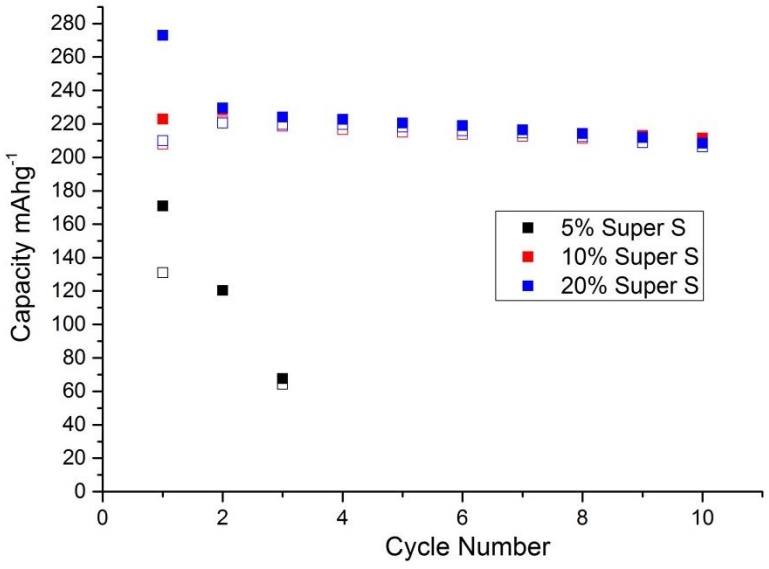

Figure 3.5: Variation of capacity with cycle number for $LiVS_2$ using various amounts of Super S carbon. Cells were cycled between 2.2 V and 0.8 V. Closed squares correspond to intercalation and open squares to deintercalation.

Figure 3.5 confirms that increase in the amount of carbon from 10% to 20% increases the irreversible capacity loss. There is also a slight increase in capacity fade when using 20% carbon. As no advantage was observed in using more than 10% carbon and using less than 10% carbon lead to the cell failing a ratio of 80 : 10 : 10 by weight of active material : Super S carbon conductive additive : Kynar 2801 Binder is used in all of the following electrochemical measurements.

The data on the electrochemical performance of $LiVS_2$ reported previously were obtained using LP40 (1 M $LiPF_6$ in 1 : 1 v/v EC : DEC) as the electrolyte[8]. A brief survey of electrolytes, and electrolyte additives, was conducted to ascertain if this was the best choice of electrolyte for future work, this can be seen in Figure 3.6 below. Figure 3.6 uses several abbreviations, these are: LP 30 = (1 M $LiPF_6$ in 1 : 1 v/v EC : DMC), LP40 = (1 M $LiPF_6$ in 1 : 1 v/v EC : DEC), VC = vinylene carbonate, FEC = fluoroethylene carbonate, PC = propylene carbonate and LiBOB = Lithium bis(oxalato)borate. For comparison with previously published work, pelletised electrodes and a slow rate of 15 mAg^{-1} were used to collect the data.

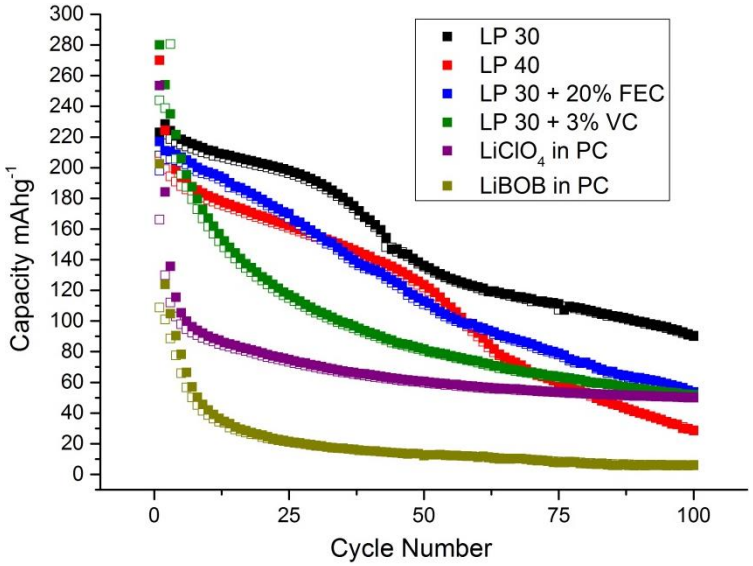

Figure 3.6: Comparison of different electrolytes for cycling of $LiVS_2$. Pellet electrodes were cycled between 2.2 V and 0.8 V at a rate of 15 mAg^{-1}. Closed squares correspond to intercalation and open squares to deintercalation.

Of the electrolytes tested LP 30 (1 M $LiPF_6$ in 1 : 1 v/v EC : DMC) was found to give the best performance. Cells constructed with LP30 show a clear improvement over those constructed with LP40 (1 M $LiPF_6$ in 1 : 1 v/v EC : DEC). The reason for this is not immediately clear. While SEI layer formation only becomes a major issue at voltages lower than the 0.8 V that these cells were cycled at it has been previously demonstrated that SEI layers do format higher voltages[15]. Presumably DEC and DMC react differently with the electrode and form SEI layers on the surface of the electrode which have different passivating effects. One piece of evidence for this is that cells using LP40 show a larger irreversible capacity on the first cycle – indicative of increased electrolyte decomposition/SEI layer formation

The addition of the electrolyte additives vinylene carbonate (VC)[16] and fluoroethylene carbonate (FEC)[17] to LP30 and LP40 have been found to improve the performance of several anode materials, however, this was not the case here where they both had a negative effect. This is not completely surprising as previously VC and FEC have been shown to improve graphite and silicon anodes that operate at lower voltages and it appears that they have much reduced effect on higher voltage anodes like $Li_4Ti_5O_{12}$[18]. One of the benefits of electrolyte additives is that they suppress side reactions and therefore reduce capacity loss[19]. It is possible that the side reactions that VC and FEC suppress take place at less than 0.8 V and therefore there is no benefit of using them with a $LiVS_2$ anode. There are no obvious differences in the load curves of the cells containing either of the additive and further work is needed to identify why there is a reduction in capacity retention when either if the additives are used.

The poor performance of $LiClO_4$ in PC could be due to issues involving co-intercalation of solvated lithium as seen in graphite and discussed in Section 1.2.1. This may also be an issue for the LiBOB (Lithium bis(oxalato)borate) containing electrolyte, however, its performance is even worse. The load curve of cells constructed using LiBOB in PC as the electrolyte show an additional plateau at 1.75 V and increased polarisation indicating a side reaction with the

electrolyte and possibly increased electrolyte decomposition. By using LP30 instead of LP40 there is an improvement in capacity and capacity retention compared to previously reported work and all the following electrochemical data presented for $LiVS_2$ were collected using LP30 as the electrolyte.

Previous work on $LiVS_2$ was carried out using electrodes that were pressed into pellets[8]. Cast electrodes have several advantages over pelletised electrodes. Firstly, they are thinner therefore kinetic issues of lithium ions moving though the electrode are reduced, particularly at higher rates of intercalation; this is a well-known issue in electrode fabrication[20]. It should be noted that the loading of the cast electrodes was 6 – 8 $mgcm^{-2}$ and therefore the electrodes were not unrealistically thin. Secondly, as the electrode is cast onto a current collector it is less likely to detach up on cycling due to electrochemical grinding. Lastly, it is a more accurate measure of the performance of a battery material as it is closer to how the electrodes of commercial lithium-ion batteries are made. Figure 3.7 below compares the cycling performance of pellet and cast electrodes at the rates of 15 mAg^{-1} and 100 mAg^{-1}. No differences were observed in the shape of the load curves between the two processing techniques and the fundamental electrochemical processes appear to be identical.

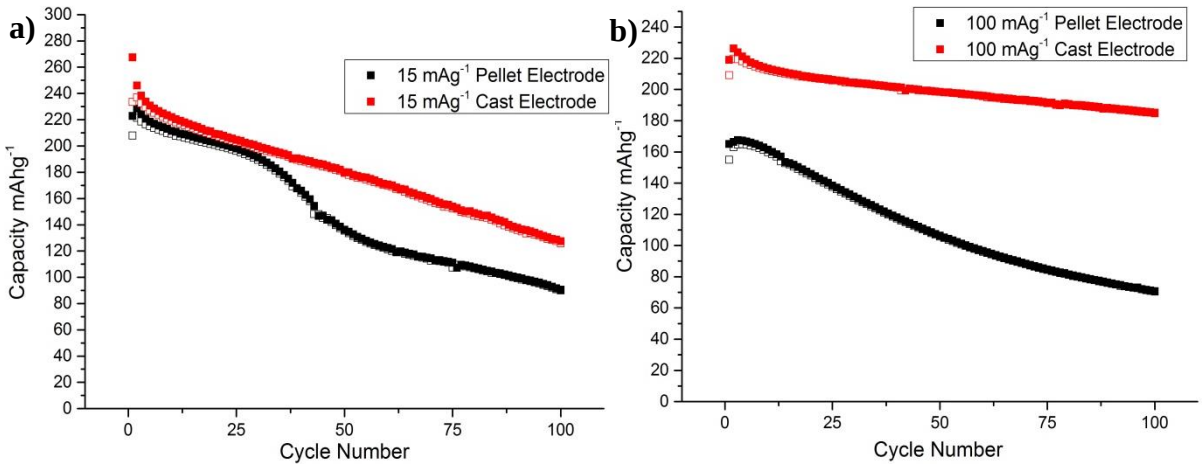

Figure 3.7 Comparison between pelletised electrodes and cast electrodes at, a) 15 mAg^{-1} and b) 100 mAg^{-1}. Cells were cycled between 2.2 V and 0.8 V. Closed squares correspond to intercalation and open squares to deintercalation.

At a slow rate of 15 mAg^{-1}, the difference between cast and pelletised electrodes is fairly small for ~ 30 cycles, at which point the pelletised electrode fades at a greater rate. This implies that pellet electrodes are degraded by electrochemical grinding on extended cycling. By contrast, there is a large difference in performance between the two processing techniques at the faster rate of 100 mAg^{-1}: implying that the insertion of Li^+ into pellets is kinetically limited by Li^+ migration through the electrode. The performance seen from the pellet electrodes is consistent with the previously reported performance of $LiVS_2$ by Goodenough. Due to the considerably improved performance seen by using cast electrodes, all electrochemical measurements in the remainder of this chapter were conducted using cast electrodes.

The above data shows that by optimising the amount of carbon additive, the electrolyte and the electrode fabrication technique the performance of $LiVS_2$ can be substantially improved compared to what has been previously reported. The rate performance of $LiVS_2$ can now be analysed in more depth. Figure 3.8 below shows the performance of $LiVS_2$ at 15 mAg^{-1}, 100 mAg^{-1} and 200 mAg^{-1}.

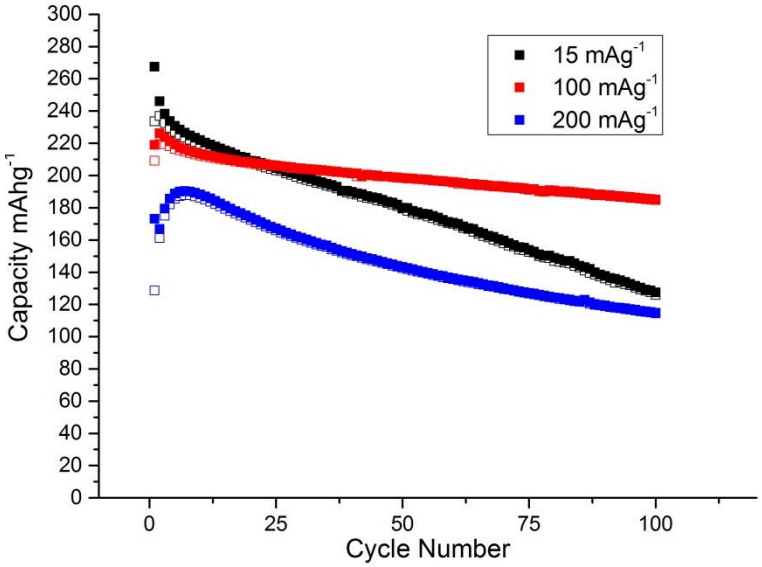

Figure 3.8: Variation of capacity with cycle number for $LiVS_2$ at various rates. Cells were cycled between 2.2 V and 0.8 V. Closed squares correspond to intercalation and open squares to deintercalation.

At a slow rate of 15 mA g^{-1} the first discharge capacity is ~ 270 $mAhg^{-1}$ and there is an irreversible capacity loss of ~ 25 $mAhg^{-1}$ on the first cycle. This is followed by a continuous capacity fade of ~ 1.2 $mAhg^{-1}$ per cycle for 100 cycles. At the intermediate rate of 100 mAg^{-1} the first discharge capacity is lower at ~ 220 $mAhg^{-1}$ and the second cycle has a higher discharge capacity (225 $mAhg^{-1}$), this is due to a rising of the discharge plateau as discussed above. Capacity fade is ~ 0.4 $mAhg^{-1}$ per cycle, one third the amount seen at the slower rate. At the fast rate of 200 mAg^{-1} it ~ 10 cycles before the maximum capacity of 190 $mAhg^{-1}$ is achieved and capacity fade is ~ 0.78 $mAhg^{-1}$ per cycle.

As the rate is increased from 15 mAg^{-1} to 100 mAg^{-1} the initial capacity falls and capacity retention increases. The first of these two occurrences is very common among battery materials and can be explained by kinetics; at faster rates it is simply not possible to insert/remove all the Li^+ needed to form Li_2VS_2 and therefore the absolute capacity is reduced. The reason for the improved capacity retention is less clear but it could possibly be due to the kinetics of SEI layer formation. At slower rates the material spends more time, in absolute terms, at low voltages and therefore there is an increase in side reactions and electrolyte decomposition, which subsequently leads to an escalation in SEI layer formation. Build-up of the SEI layer leads to less lithium intercalating into the structure and consequently more capacity fade. Impedance spectroscopy could be carried out in the future to see if this is the case.

When the rate is increased from 100 mAg^{-1} to 200 mAg^{-1} the maximum capacity is reduced and the number of cycles required to achieve it is increased. The need for several cycles before the maximum capacity is achieved is due to capacity being "cut-off" on discharge due to the larger polarisation at higher rates as discussed above. By the time the maximum capacity has been achieved there has been several cycles where additional SEI layer formation may have taken place and this could be one of the reasons why the maximum capacity is less than seen for 100 mAg^{-1}. This process can be circumvented by doing one cycle at a slow rate of 15 mAg^{-1} before

increasing the rate, this is often referred to cycling conditioning and is a common technique for cycling electrodes at high rates. Figure 3.9 below shows one initial cycle at 15 mAg^{-1} followed by 200 cycles at 200 mAg^{-1}.

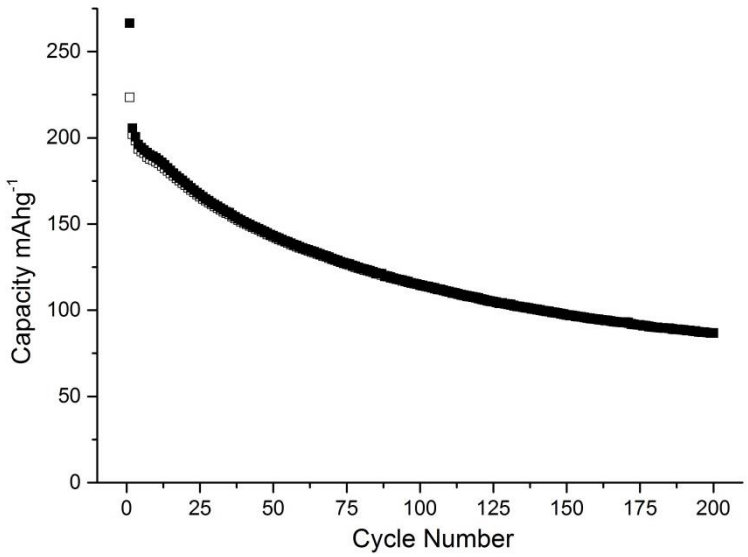

Figure 3.9: Variation of capacity with cycle number for $LiVS_2$ at 200 mAg^{-1} after 1 cycle at 15 mAg^{-1}. Cells were cycled between 2.2 V and 0.8 V. Closed squares correspond to intercalation and open squares to deintercalation.

While the data in Figure 3.9 show a large irreversible capacity loss on the first cycle due to the change in rate, it subsequently shows capacity retention consistent with the 200 mAg^{-1} data presented in Figure 3.8. The maximum capacity displayed at 200 mAg^{-1} is 205 $mAhg^{-1}$, still less than that seen at 100 mAg^{-1}, presumably due to the kinetics issues discussed above. The capacity fade at 200 mAg^{-1} is large than seen at 100 mAg^{-1}. This is often observed for electrode materials at fast rates and relates to the expansion of the electrode. When lithium is inserted in to the electrode it expands (~ 23%) and the morphology changes. At high rates, due to kinetics, the lithium rich phase is concentrated at the anode/electrolyte interface and not the anode/current collector interface. The size gradient across the electrode leads to the breaking up of the electrode and consequently capacity fade.

The rate data displayed above indicates that the performance of the $LiVS_2$ electrodes presented here are far superior to previously published work. However, the voltage range used is an issue

as it includes the high voltage plateau at ~ 2.1 V. This corresponds to the $V^{3+/4+}$ redox process not the $V^{2+/3+}$ redox process that is involved in formation of Li_2VS_2. To correct for this, cycling data was collected by cycling between 0.8 V and 1.8 V vs Li^+.

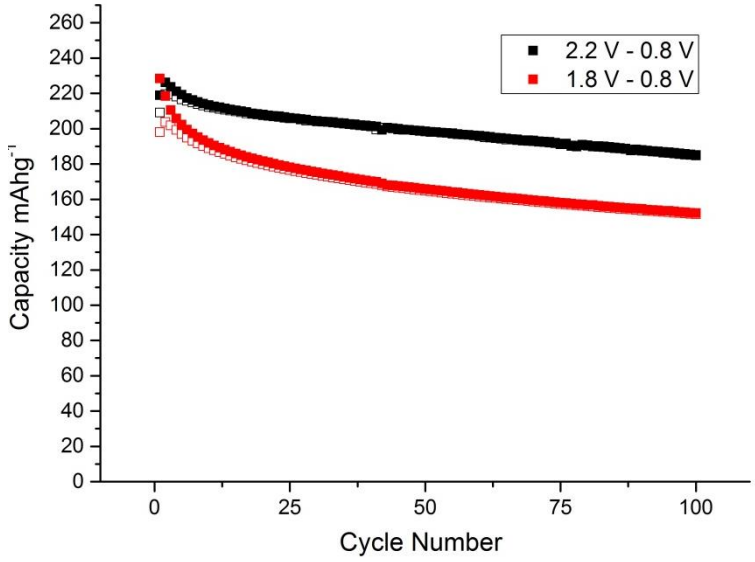

Figure 3.10: Variation of capacity with cycle number for $LiVS_2$ at different voltage cut offs, cells were cycled at a rate of 100 mAg^{-1} for 100 cycles. Closed squares correspond to intercalation and open squares to deintercalation.

Figure 3.10 shows data collected at 100 mAg^{-1} for upper voltage cut offs of 2.2 V and 1.8 V. When the upper voltage cut-off is reduced to 1.8 V there is a drop in capacity as the upper voltage plateau, contributing ~ 30 $mAhg^{-1}$ on the second cycle and onwards (Figure 3.4), is no longer present past the first discharge. The fact that the plateau is still present on the first discharge - unavoidable as the open circuit voltage (OCV) is 2.2 V - leads to an increased irreversible capacity loss on the first cycle. While the above observations are expected it is initially more surprising that lowering the voltage cut off leads to increased capacity fade. The reason for this can be seen in the load curve of $LiVS_2$. As $LiVS_2$ cycles a decreasing amount of capacity comes from the main low voltage plateau and the high voltage plateau and sloping region between the plateaus becomes more significant, this can be seen in Figure 3.11 below.

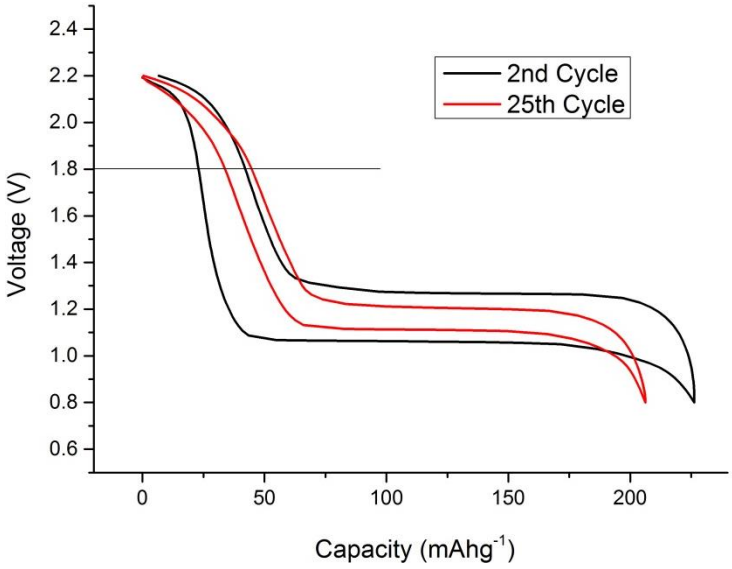

Figure 3.11: Load curves of the 2nd and 25th cycle of $LiVS_2$ at 100 mAg^{-1}. Voltage lost above the 1.8 V cut off is indicated.

As the above figure shows, if the voltage were limited to 1.8 V the 25th cycle would lose a much larger percentage of its capacity than the 2nd cycle, this leads to increased capacity loss as the voltage cut off is reduced. Reducing the voltage cut-off to lower voltages would intensify this effect further.

Some work has also been conducted on optimising the lower voltage cut-off. As moving to a lower voltage cut-off would increase SEI layer formation and irreversible capacity loss (as discussed above) it was decided to raise the lower voltage to 0.9 V in the hope of reducing capacity fade on cycling. The data for this can be seen Figure 3.12.

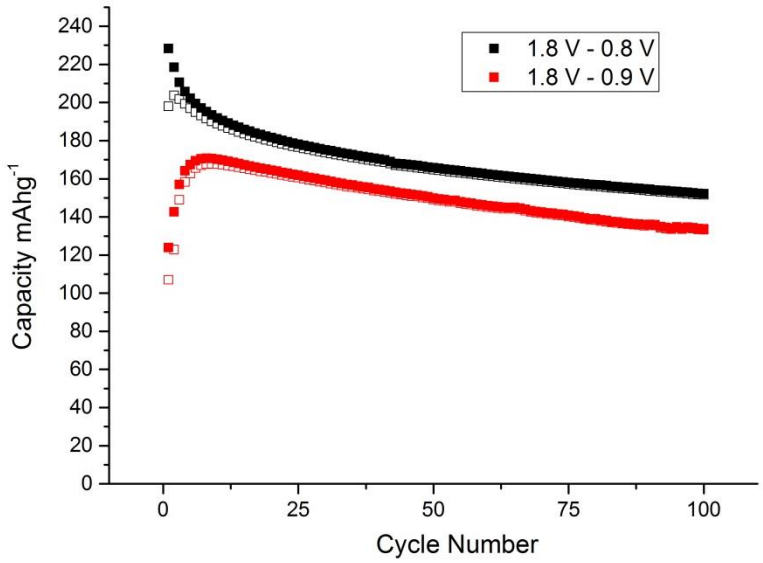

Figure 3.12: Variation of capacity with cycle number for $LiVS_2$ at different voltage cut offs, cells were cycled for 100 cycles at a rate of 100 mAg^{-1}. Closed squares correspond to intercalation and open squares to deintercalation.

As the data above shows 0.9 V is not an appropriate voltage cut off as too much capacity is delivered below this potential, especially on the first cycle, and the capacity of the cell is compromised to an unreasonable degree. Additionally, there is no apparent improvement in capacity retention by using the higher cut-off. Consequently, 0.8 V is the optimum low voltage cut-off for $LiVS_2$.

3.6 Scanning Electron Microscopy

Scanning electron microscopy (SEM) was carried out on pristine $LiVS_2$ and on electrodes that had been cycled. SEM was carried out using a Carl Zeiss Merlin instrument as described in Chapter 2. For ease of sample preparation pellet electrodes were used to collect images of cycled material. To make the comparison between pristine material and cycled material as easy and relevant as possible the pristine uncycled material was also mixed with Super S carbon and Kynar binder, pressed in to a pellet and placed in to a coin cell. SEM images are shown in Figure 3.13 below.

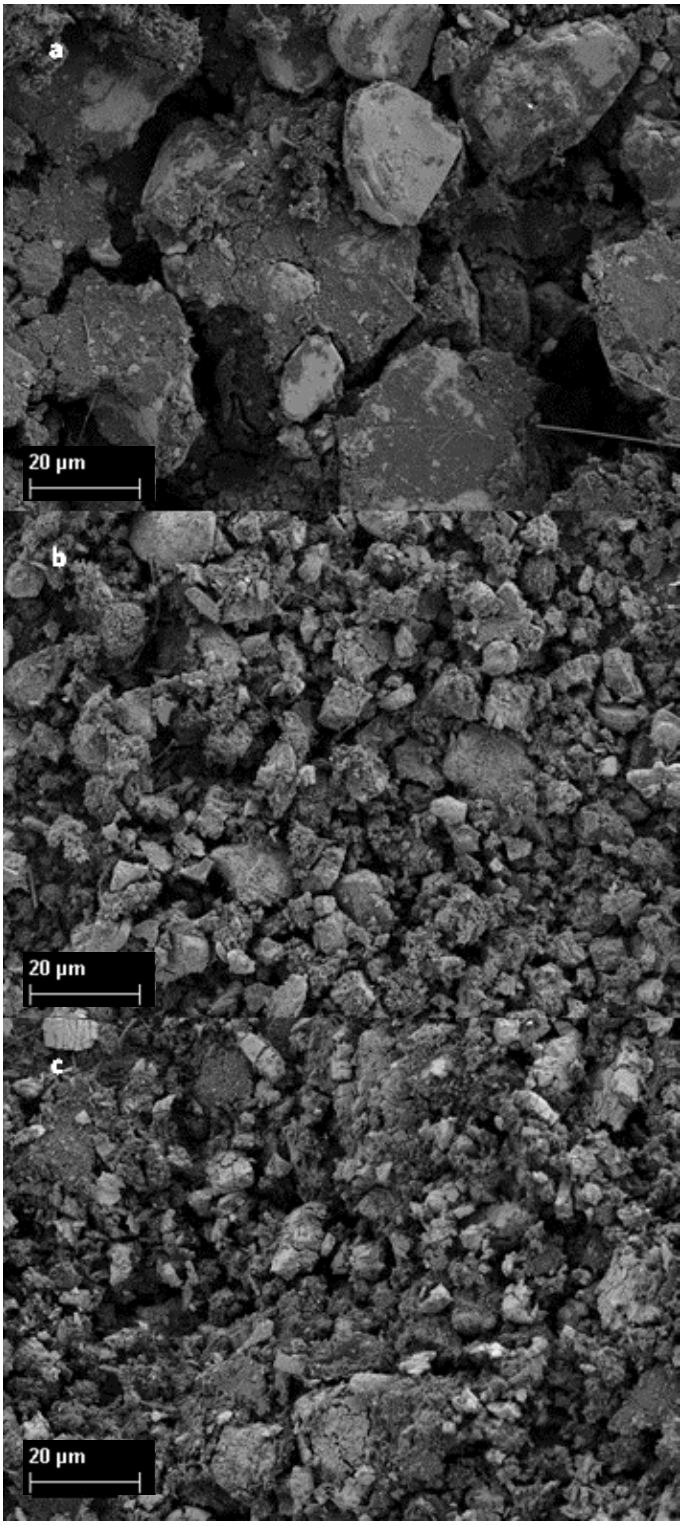

Figure 3.13: SEM images of $LiVS_2$, a) pristine uncycled material, b) after 1 cycle, c) after 10 cycles. The scale bar is 20 µm.

The large particles in the SEM images above are $LiVS_2$ and the small dark particles are the Super S carbon additive. The long thin features visible in the bottom right of Figure 3.13a are the remains of a glass fibre separator used in the coin cell. The images show that pristine

samples of $LiVS_2$ are made up of large particles that are 20 – 50 μm in diameter. On the first cycle these break up to form particles that are approximately 10 μm in diameter. There is very little if any change in particle size on subsequent cycling. The large change in particle size on the first cycle mirrors the large change in polarisation also seen after the first cycle. That there is little change in particle size on subsequent cycling is expected due to the good cycling performance of the material. Future work could focus on reducing the particle size of the pristine material, either through a change in the synthesis procedure or via ball milling.

3.7 Summary and Conclusions

$LiVS_2$ has been successfully synthesised, characterised and tested electrochemically. The same synthetic technique previously used by Goodenough and co-workers was used, however, it was found that only one heating cycle was required to obtain the target material. The synthesised materials had higher lithium contents than previously reported samples but were otherwise structurally the same, as confirmed by PXRD and neutron diffraction. The higher lithium content led to a smaller irreversible capacity loss on the first discharge, as the high voltage plateau was less significant.

The electrochemical performance of $LiVS_2$ has been optimised by reducing the amount of carbon used in electrode fabrication, changing the electrolyte from LP 40 to LP 30 and by casting the electrodes as opposed to palletising. These changes improve absolute capacity, irreversible capacity loss and capacity fade compared to previously reported data. At a rate of 200 mAg^{-1} (C-rate) a capacity of 190 $mAhg^{-1}$ was achieved, this is compared to ~ 100 $mAhg^{-1}$ that had been previously reported[8], a near 100% improvement. Capacity fade has been reduced from over 1 $mAhg^{-1}$ per cycle to less than 0.5 $mAhg^{-1}$ at C/2, and the irreversible capacity loss has been reduced from 70 $mAhg^{-1}$ to virtually nothing.

While cycling between 2.2 V and 0.8 V produced the best cycling performance, using an upper voltage cut-off of 1.8 V gives a more accurate depiction of the performance of $LiVS_2$ as an anode material and still produces far superior electrochemistry compared to what had been previously reported. At a rate of 100 mAg^{-1} the capacity is over 200 $mAhg^{-1}$ compared to less than 150 $mAhg^{-1}$ previously reported by Goodenough and co-workers, this is coupled with superior capacity retention.

This work demonstrates for the first time that lithium metal sulphides can be viable anode materials for use in lithium-ion batteries. However, the operating voltage, inherent to the material, is relatively close to that of $Li_4Ti_5O_{12}$ and it is not a true one volt anode. Additionally, there is a large structural change on the first cycle, as seen electrochemically and via SEM, which leads to a large polarisation on the first cycle and the performance at higher rates is poor. The following chapter will investigate the solid solution $LiV_{1-x}Ti_xS_2$ with the aim of addressing these issues.

3.8 References

1 Zhang, S. S. *J. Power Sources* **161**, 1385-1391 (2006).
2 Smart, M. C. & Ratnakumar, B. V. *J. Electrochem. Soc.* **158**, A379-A389 (2011).
3 Ratnakumar, B. V. & Smart, M. C. *Rechargeable Lithium-Ion Batteries* **25**, 241-252 (2010).
4 Colbow, K. M., Dahn, J. R. & Haering, R. R. *J. Power Sources* **26**, 397-402 (1989).
5 He, M. L. *et al. J. Electrochem. Soc.* **162**, A870-A876 (2015).
6 Goodenough, J. B. & Park, K. S. *J. Am. Chem. Soc.* **135**, 1167-1176 (2013).
7 Kim, Y., Park, K. S., Song, S. H., Han, J. T. & Goodenough, J. B. *J. Electrochem. Soc.* **156**, A703-A708 (2009).
8 Gupta, A., Mullins, C. B. & Goodenough, J. B. *Electrochim. Acta* **78**, 430-433 (2012).
9 Wiegers, G. A. *Prog. Solid State Chem.* **24**, 1-139 (1996).
10 Vanlaar, B. & Ijdo, D. J. W. *J. Solid State Chem.* **3**, 590-& (1971).
11 Jarvinen, M., Merisalo, M., Pesonen, A. & Inkinen, O. *J. Appl. Crystallogr.* **3**, 313-& (1970).
12 Li, D. & Zhou, H. S. *Mater. Today* **17**, 451-463 (2014).
13 Guo, Y., Zhang, G. R., Zhang, X. L., Jia, T. & Zeng, Z. *J. Appl. Phys.* **109**, 3 (2011).
14 Katayama, N. *et al. Phys. Rev. Lett.* **103**, 4 (2009).
15 Verma, P., Maire, P. & Novak, P. *Electrochim. Acta* **55**, 6332-6341 (2010).
16 Aurbach, D. *et al. Electrochim. Acta* **47**, 1423-1439 (2002).
17 Choi, N. S. *et al. J. Power Sources* **161**, 1254-1259 (2006).
18 El Ouatani, L., Dedryvere, R., Siret, C., Biensan, P. & Gonbeau, D. *J. Electrochem. Soc.* **156**, A468-A477 (2009).
19 Aurbach D., Gamolsky K., Markovsky B., Gofer Y., Schmidt M., Heider U., Electrochimica Acta, 47, 1423 (2002).
20 Rui, Z., Jie, L. & Junjie, G. *Appl. Energy* **139**, 220-229 (2015).

Chapter 4: $LiV_{1-x}Ti_xS_2$ solid solution system as an anode material for Lithium-ion Batteries

4.1 Introduction

In the previous chapter it was demonstrated that $LiVS_2$ can achieve a level of performance higher than had previously been reported and should be considered of interest as a potential anode material for lithium-ion batteries. However, it is not a true one volt anode and it would be beneficial to lower the operating voltage so that deintercalation of Li^+, the potential of the anode during discharge when used in a full cell, takes place under 1 V vs Li^+/Li^0. This would maximise the cell potential while still ensuring a buffer before lithium plating occurs.

As discussed in Section 1.3.3.6 $LiTiS_2$ has a deintercalation voltage of 0.6 V vs Li^+/Li^0 but has very poor electrochemical performance[1]. It was speculated that the addition of Ti to $LiVS_2$ would lower the operating voltage, due to the lower effective nuclear charge and hence higher energy d-states[2], while still maintaining the superior performance of $LiVS_2$. It has been previously demonstrated by J.B. Goodenough and co-workers that $LiV_{0.7}Ti_{0.3}S_2$ can be synthesised and cycled as a cathode material[2], however, the $LiV_{1-x}Ti_xS_2$ solid solution has never been investigated as an anode.

In this chapter the various members of the $LiV_{1-x}Ti_xS_2$ solid solution have been synthesised and electrochemically tested as anode materials. The most promising composition has been identified and has been optimised, both synthetically and electrochemically, and its structure has been characterised by X-ray and neutron refinement. This is followed by in depth analysis of the electrochemical process the material undergoes and investigation of the SEI layer which

forms on cycling has been investigated. At the conclusion of the chapter the performance of the material is evaluated compared to $LiVS_2$ and other anode materials.

4.2 Overview of the $LiV_{1-x}Ti_xS_2$ solid solution

4.2.1 Synthesis

Various compositions of the $LiV_{1-x}Ti_xS_2$ solid solution were synthesised following the same general procedure as $LiVS_2$. Stoichiometric amounts of lithium sulphide (Li_2S), sulphur (S), titanium metal (Ti) and vanadium metal (V) were placed in a sealed silica tube. While pure phase $LiVS_2$ and $LiTiS_2$ could be achieved at a temperature of 750 ^oC, materials containing both transition metals required the higher temperature of 850 ^oC, otherwise evidence of $LiVS_2$ and $LiTiS_2$ could be observed in X-ray diffraction patterns. Presumably, this was due to inadequate diffusion of the transition metals at the lower temperature leading to $LiVS_2$ and $LiTiS_2$ rich areas of material. The ramp rate (1 $^oC\ min^{-1}$) and length of heating used (3 days) were the same across the series. If this class of material were ever to be commercialised work would have to be done on trying to reduce the length of the heating process.

It was found that for compositions with more than 20% Ti the temperature that the reaction was quenched at was important. When the $LiVS_2$ procedure was followed, cooling to 300 ^oC at a rate of 1.5 $^oC\ min^{-1}$ and then removed from the furnace, a mixture of different phases was observed. The first phase was the desired hexagonal close packed (IT) phase and the second was the cubic close packed (3R) phase. Co-existence of the two phases has been previously reported in the $LiTi_{1-y}Ni_yS_2$ solid solution[3]. When the $LiVS_2$ procedure was used the amount of the two phases would vary considerably from sample to sample. To help ensure the product was the desired phase it was necessary to quench the reaction directly after the heating step at 850 ^oC. This indicates that the hcp phase is stabilised at high temperatures and the ccp phase by lower temperatures. Even quenching from 850 ^oC would occasionally lead to a small amount

of ccp phase being present – presumably due to the quenching not being quick enough. It is possible that the stability of the two phases is very sensitive to lithium content, with increased lithium content promoting the ccp phase. At higher temperatures there is greater evaporation of lithium and therefore the lithium content of the sulphide will be reduced, this appears to stabilise the hcp phase.

Samples containing even a small amount of the cubic phase displayed considerably inferior electrochemical performance, this can be rationalised by considering that the Li_2MS_2 phase is a hcp phase and converting from a ccp phase to a hcp phase requires a greater structural organisation than a hcp to hcp transition. All the data in this chapter is from materials that are the pure IT hcp phase. Like $LiVS_2$, no advantage was observed by having multiple heating cycles. Figure 4.1 below shows two XRD patterns of $LiV_{0.5}Ti_{0.5}S_2$, one pure IT phase and one a mixture of phases.

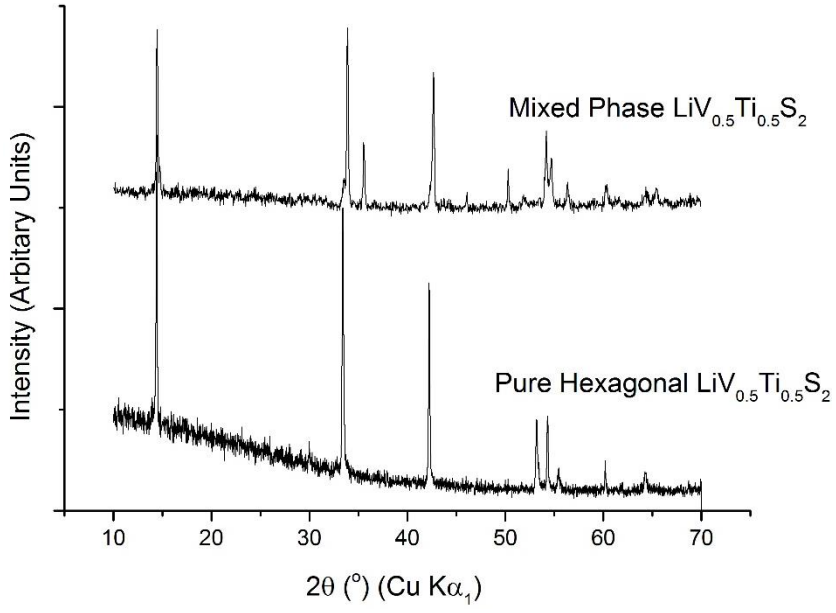

Figure 4.1: X-ray diffraction patterns of different phases of $LiV_{0.5}Ti_{0.5}S_2$.

While many compositions from the $LiV_{1-x}Ti_xS_2$ solid solution were successfully synthesised the rest of Section 4.2 will focus on $LiVS_2$, $LiV_{0.75}Ti_{0.25}S_2$, $LiV_{0.5}Ti_{0.5}S_2$, $LiV_{0.25}Ti_{0.75}S_2$ and $LiTiS_2$. Important structural and electrochemical changes across the series changed linearly

with increasing titanium content and the selection of these five compositions allows for trends to be seen across the series without figures becoming unnecessarily cluttered.

4.2.2 Structural changes across the $LiV_{1-x}Ti_xS_2$ solid solution

X-ray diffraction was carried out on compositions from the $LiV_{1-x}Ti_xS_2$ solid solution to make sure samples were pure phase and to observe any changes across the series. Powder X-ray diffraction was carried out using a Stoe STADI/P diffractometer using Cu $K\alpha_1$ radiation, as all members of the $LiV_{1-x}Ti_xS_2$ solid solution were presumed to be air sensitive, samples were run in capillaries. Figure 4.2 below shows the X-ray diffraction patterns for $LiVS_2$, $LiV_{0.75}Ti_{0.25}S_2$, $LiV_{0.5}Ti_{0.5}S_2$, $LiV_{0.25}Ti_{0.75}S_2$ and $LiTiS_2$.

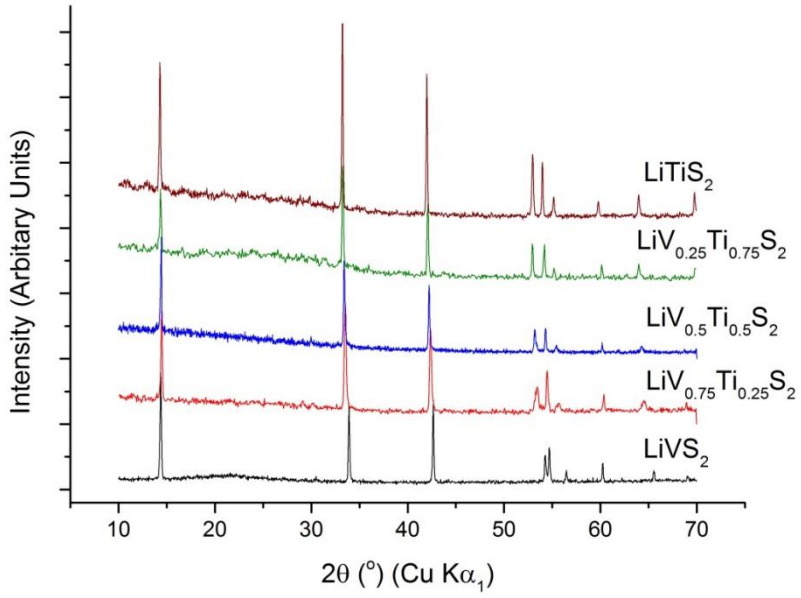

Figure 4.2: X-ray diffraction patterns from various compositions across the $LiV_{1-x}Ti_xS_2$ solid solution.

As can be seen in the figure above there is very little structural change across the series. This shows that all compositions of the $LiV_{1-x}Ti_xS_2$ solid solution have the same layered structure that was detailed in Section 1.3.3.6. As seen in X-ray diffraction patterns of $LiVS_2$ there is an increase in background noise at low angles because of the signal from the glass capillary.

The change in lattice parameters is roughly linear across the series, however, there is a larger change in the **a** parameter when titanium is first introduced into the system. There is a slight increase in both **a** and **c** as Ti^{3+} has a slightly larger ionic radii than V^{3+}. It is unclear if the larger change seen between $LiVS_2$ and $LiV_{0.75}Ti_{0.25}S_2$ and the subsequent changes is due to a small structural modification necessary to accommodate the larger Ti^{3+} or due to the $LiV_{0.75}Ti_{0.25}S_2$ sample containing more than anticipated amount of titanium. The lattice parameters of synthesised $LiV_{0.75}Ti_{0.25}S_2$ and $LiTiS_2$ are in agreement with literature values of $LiV_{0.7}Ti_{0.3}S_2$ and $LiTiS_2$ respectively. The change in lattice parameters across the series can be seen in Figure 4.3 below:

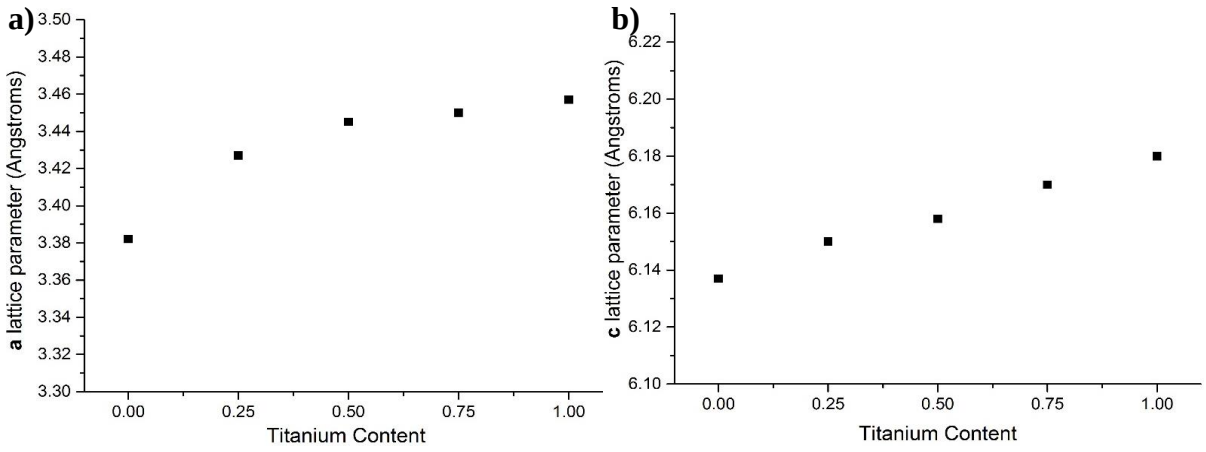

Figure 4.3: Lattice parameters across the series, a) a parameter and b) c parameter.

4.2.3 Electrochemistry

Electrochemical measurements were performed in coin cells as described in Section 2.7. After the optimisation work carried out on $LiVS_2$, cast electrodes were used and LP30 was used as the electrolyte. Electrodes were fabricated using the ratio 80 : 10 : 10 by weight of active material : Super S carbon conductive additive : Kynar 2801 Binder. As can be seen in the load curves below, increasing the amount of titanium lowered the voltage at which lithium

intercalates/deintercalates, therefore the lower voltage cut-off needed to be changed. Figure 4.4, shows the 1st cycle and 5th cycle for $LiVS_2$, $LiV_{0.75}Ti_{0.25}S_2$, $LiV_{0.5}Ti_{0.5}S_2$, $LiV_{0.25}Ti_{0.75}S_2$ and $LiTiS_2$. All data was collected at a slow rate of 15 mAg^{-1} and an upper voltage limit of 2.2 V was used.

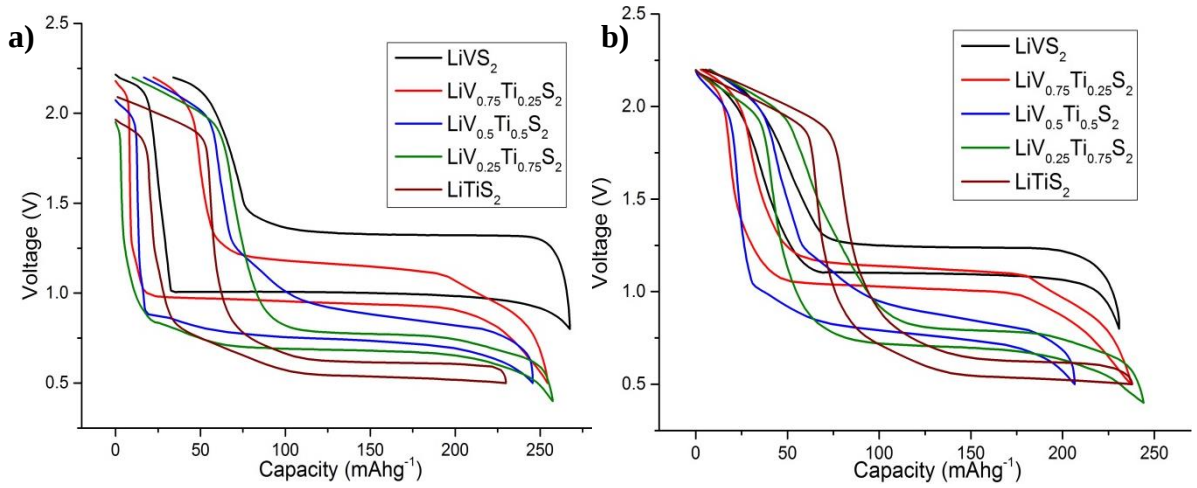

Figure 4.4: Load curves of various compositions across the $LiV_{1-x}Ti_xS_2$ solid solution, measurements made at a rate of 15 mA g^{-1}, a) 1st cycle and b) 5th cycle.

Several tends can be observed from the data in the Figure above. Firstly, as the titanium content is increased the voltage of both intercalation and deintercalation is decreased in a roughly linear manner. The first composition with the majority of the capacity associated with intercalation and deintercalation to be below 1 V vs Li^+/Li^0 is $LiV_{0.5}Ti_{0.5}S_2$. Table 4.1 below shows the voltage at the mid-point of the charge plateau on the 1st and 5th cycles across the series.

Composition	1st Charge Voltage (V)	5th Charge Voltage (V)
$LiVS_2$	1.33	1.24
$LiV_{0.75}Ti_{0.25}S_2$	1.16	1.15
$LiV_{0.5}Ti_{0.5}S_2$	0.91	0.93
$LiV_{0.25}Ti_{0.75}S_2$	0.78	0.80
$LiTiS_2$	0.62	0.62

Table 4.1: Voltage at the mid-point of the charge plateau on the 1st and 5th cycles across the series

On the first discharge $LiV_{0.5}Ti_{0.5}S_2$, $LiV_{0.25}Ti_{0.75}S_2$ and $LiTiS_2$ all have plateaus that begin at around 0.8 V, this is in line with where SEI layer formation begins on carbon and other anode materials[4]. The plateaus of $LiV_{0.5}Ti_{0.5}S_2$ and $LiV_{0.25}Ti_{0.75}S_2$ both have features (pseudo-

plateaus) for the first ~ 30 $mAhg^{-1}$ that this feature is at roughly 0.8 V indicates that SEI layer formation and lithium insertion happen at the same or similar voltages. When $LiTiS_2$ is reached there are now two distinct plateaus, the first is associated with SEI layer formation (and is irreversible) and the second is due to lithium insertion[1].

There is a decrease in polarisation with increasing titanium content. This may be due to the disruption of the vanadium trimers discussed in Section 3.5. The decrease in vanadium trimers may also be responsible for the load curves of high titanium content materials changing less on cycling – while $LiVS_2$ has a large decrease in polarisation over the first 5 cycles, $LiV_{0.25}Ti_{0.75}S_2$ and $LiTiS_2$ show virtually no change at all. Alternatively, the increase in titanium could lead to an increase in defects in the $LiMS_2$ structure. These defects could subsequently result in additional nucleation sites for formation of the Li_2MS_2 phase on the first cycle therefore there is less resistance to the intercalation process and polarisation is smaller.

Cycling data was collected across the series at a rate of 100 mAg^{-1}. All cells had an upper voltage cut-off of 2.2 V, the lower voltage cut-offs were: 0.8 V for $LiVS_2$, 0.7 V for $LiV_{0.75}Ti_{0.25}S_2$ and 0.5 V for $LiV_{0.5}Ti_{0.5}S_2$, $LiV_{0.25}Ti_{0.75}S_2$ and $LiTiS_2$.

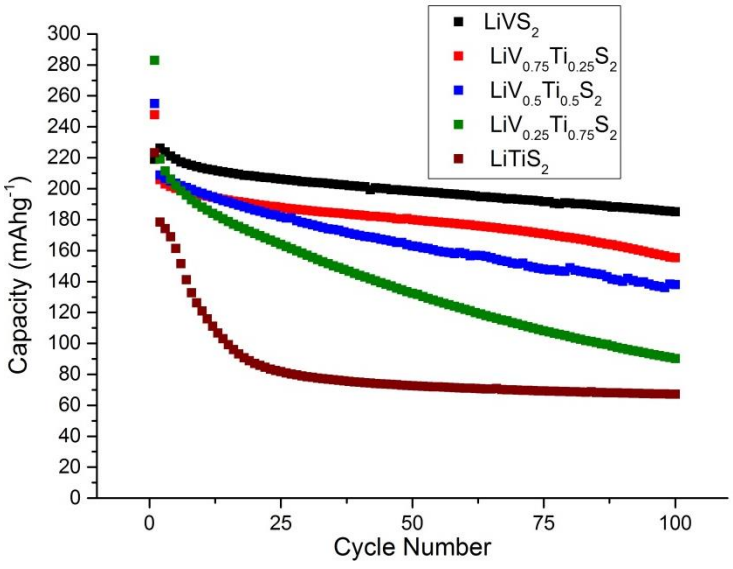

Figure 4.5: Discharge capacities of various compositions across the $LiV_{1-x}Ti_xS_2$ solid solution, cells were cycled at a rate of 100 mA g^{-1}.

As is clearly apparent in Figure 4.5 increasing titanium leads to a significant drop in the cyclability of the material. The very poor performance of $LiTiS_2$ is broadly consistent with the data previously reported by Goodenough[1]. The major difference is the much smaller irreversible capacity loss in the material reported here, this is due to only 10% carbon additive being used as opposed to the 20% by Goodenough. $LiV_{0.25}Ti_{0.75}S_2$ appears promising for the first few cycles; however, it has poor capacity retention. Out of the titanium containing compounds shown only $LiV_{0.75}Ti_{0.25}S_2$ and $LiV_{0.5}Ti_{0.5}S_2$ display anything approaching acceptable capacity retention.

4.2.4 Summary and Conclusion

Compositions across the $LiV_{1-x}Ti_xS_2$ solid solution have been synthesised and tested electrochemically. Synthesis was complicated by the presence of a second phase and a higher heating and quenching temperature were required to obtain pure phase materials with increased reliability. There are no significant structural changes across the series: only a small increase in lattice parameters with increasing Ti content.

As the amount of vanadium is reduced the voltages for intercalation and deintercalation decrease and polarisation is also reduced. However, these trends coincide with an increase in capacity fade. The chronic capacity fade found in compositions with high titanium contents results in them not being suitable anode materials for lithium-ion batteries.

Further work in this chapter will focus on $LiV_{0.5}Ti_{0.5}S_2$. This composition was chosen for more in depth analysis as it is the material with the lowest titanium content to have the majority of the deintercalation potential under 1 V vs Li^+/Li^0. This was therefore thought to be the best compromise between operating voltage and capacity fade.

4.3 Optimisation of $LiV_{0.5}Ti_{0.5}S_2$

Before detailed characterisation and electrochemical measurements were carried out on $LiV_{0.5}Ti_{0.5}S_2$ the synthesis and cycling conditions were optimised. While synthesis at 850 ^oC could produce a pure phase material it was found that increasing the synthesis temperature improved the electrochemical performance. Heating temperatures were explored between 850 ^oC and 1150 ^oC at 50 ^oC increments, heating above 1150 ^oC risked melting the silica tube. The optimum heating temperature was found to be 1050 ^oC. The ramp rate, 1 $^oC\ min^{-1}$, and length of heating, 3 days, were the same as the synthesis discussed above. The sealed silica tubes were quenched in air at 1050 ^oC; this resulted in no sign of the ccp 3R phase in any sample.

Figure 4.6 shows the difference in cycling performance between $LiV_{0.5}Ti_{0.5}S_2$ synthesised at 850 ^oC and 1050 ^oC at a rate of 100 mAg^{-1}. The material synthesised at 850 ^oC was cycled between 1.8 V and 0.5 V, while the material synthesised at 1050 ^oC was cycled between 1.8 V and 0.6 V, the reason for this difference is discussed below

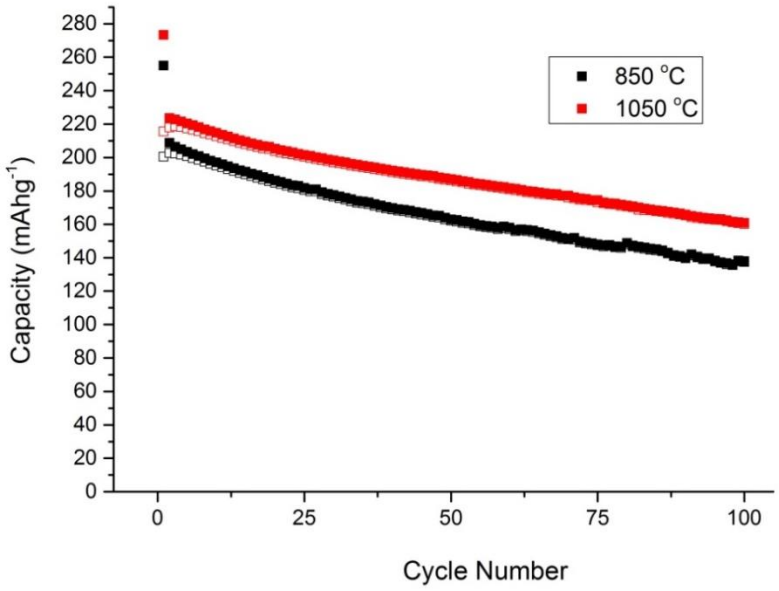

Figure 4.6: Variation of capacity with cycle number for $LiV_{0.5}Ti_{0.5}S_2$ at different synthesis temperatures. Cells were cycled at a rate of 100 mAg^{-1}. Closed squares correspond to intercalation and open squares to deintercalation.

As Figure 4.6 demonstrates $LiV_{0.5}Ti_{0.5}S_2$ synthesised at 1050 ^oC shows higher capacities and improved capacity retention compared to samples synthesised at 850 ^oC at a rate of 100 mAg^{-1}. The samples synthesised at 1050 ^oC show a peak reversible capacity of 220 $mAhg^{-1}$, 99% of the theoretical capacity of 222 mAh^{-1}.

To investigate the reason for the improvement in performance between materials synthesised at 850 ^oC and 1050 ^oC the XRD patterns and electrochemical load curves of the two materials are compared below. Figure 4.7 shows the X-ray diffraction pattern of $LiV_{0.5}Ti_{0.5}S_2$ after synthesis at 850 ^oC and 1050 ^oC.

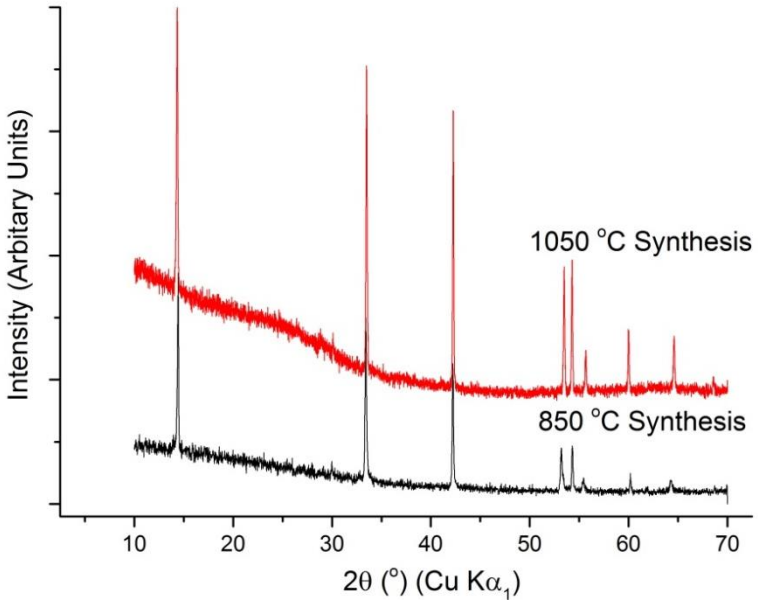

Figure 4.7: X-ray diffraction patterns of $LiV_{0.5}Ti_{0.5}S_2$ at different synthesis temperatures.

There is virtually no difference in the XRD patterns $LiV_{0.5}Ti_{0.5}S_2$ at the two synthesis temperatures. Synthesis at the higher temperature results in a more crystalline material, however, the positions and relative peak intensities appear to be unchanged. This suggests that while the change in synthesis temperature may affect cycling performance it does not change the fundamental crystal structure of $LiV_{0.5}Ti_{0.5}S_2$.

Figure 4.8 below shows the 1st and 5th cycle load curves at the two different synthesis temperatures.

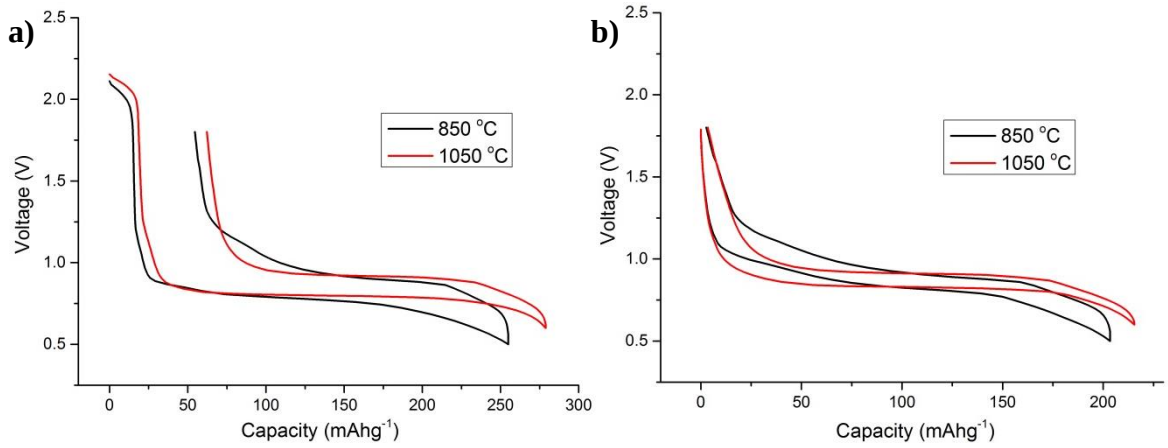

Figure 4.8: Load curves of $LiV_{0.5}Ti_{0.5}S_2$ synthesised at 850 °C and 1050 °C, measurements were collected at a rate of 100 mA g^{-1}, a) 1st cycle and b) 5th cycle

There is a small increase in the capacity of the high voltage plateau in the sample synthesised at 1050 °C. This is consistent with the higher temperature being used leading to increased evaporation of lithium. This could be seen when the reactions were removed from the furnace, as tubes heated at the higher temperature showed increased evidence of reaction between the silica walls and lithium. Samples synthesised using the different heating temperatures have approximately the same polarisation and both see a small reduction in polarisation between the first cycle and 5th cycle.

While the potentials of lithium intercalation and deintercalation are roughly consistent between the heating temperatures, the main voltage plateaus of the material synthesised at 850 °C is more "sloping" in appearance, particularly after the first cycle (Figure 4.8b). This possibly indicates that at this heating temperature the Ti and V were not homogeneously dispersed throughout the material and this leads to areas that are vanadium rich and areas that are titanium rich. This subsequently results in the vanadium rich regions behaving like $LiVS_2$ and shifting the potential of intercalation/deintercalation to higher voltages and the titanium rich areas doing the reverse and moving the potential of intercalation/deintercalation to lower voltages. The combined result of these two effects is the "sloping" plateau seen in samples synthesised at 850 °C. At higher synthesis temperatures diffusion of starting materials is easier and the materials

synthesised at 1050 ^{o}C have a much flatter plateau, possibly due to better distribution of vanadium and titanium, which results in virtually all of the capacity for charge and discharge occurring below 1 V and above 0.6 V vs Li^{+}/Li^{0}. Materials synthesised at both temperatures have the same initial intercalation voltage on the first cycle, possibly due to issues involving SEI layer formation.

Capacity retention is superior for samples synthesised at 1050 ^{o}C for two reasons, firstly, due to the flatter plateau, the material spends less time at low voltages and there is less SEI layer formation on the surface of the electrode. The second reason is that as virtually all of the discharge capacity occurs above 0.6 V, this allows for the use of a voltage cut-off of 0.6 V for samples synthesised at 1050 ^{o}C as opposed to the 0.5 V cut-off required by a 850 ^{o}C synthesis temperature. Figure 4.9 below shows capacity vs cycle number plots of two $LiV_{0.5}Ti_{0.5}S_2$ samples synthesised at 1050 ^{o}C but using different voltage cut-offs.

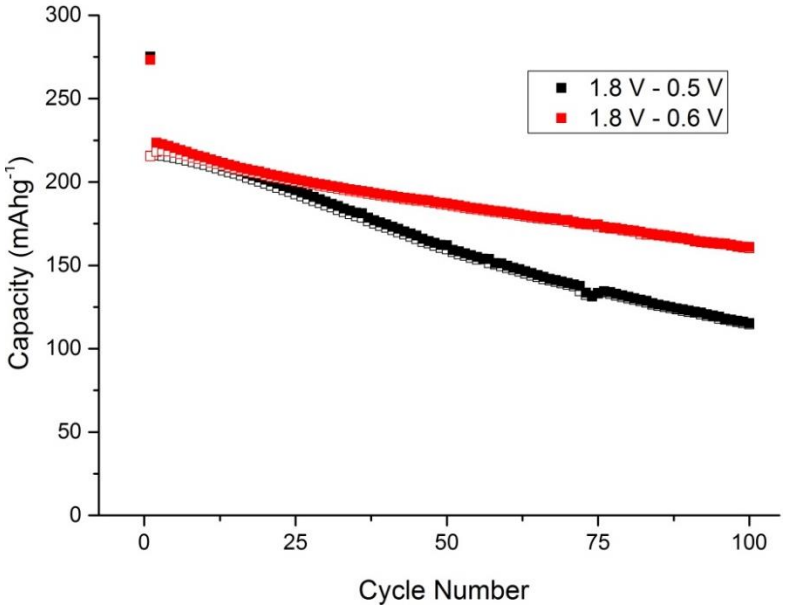

Figure 4.9: Variation of capacity with cycle number for $LiV_{0.5}Ti_{0.5}S_2$ using different voltage limits. Cells were cycled at a rate of 100 mA g^{-1}. Closed squares correspond to intercalation and open squares to deintercalation.

As Figure 4.9 clearly depicts the two lower voltage cut-offs have the same absolute capacity and capacity retention for the first 20 cycles, at which point the sample with the 0.5 V cut-off

fades at a significantly quicker rate. This is most likely due to an increased build up in SEI layer on the surface of the active material at the lower voltage. Increasing the lower voltage cut-off further to 0.7 V was not practical as too much intercalation of lithium, and hence capacity, took place below 0.7 V. Like $LiVS_2$ discussed in Chapter 3, lowering the upper voltage cut-off below 1.8 V leads to decreased capacity retention, therefore the optimum voltage range for $LiV_{0.5}Ti_{0.5}S_2$ is 1.8 V – 0.6 V.

4.4 Characterisation of $LiV_{0.5}Ti_{0.5}S_2$

4.4.1 X-ray Diffraction

Now that the synthesis and cycling conditions of $LiV_{0.5}Ti_{0.5}S_2$ have been optimised attention can be turned to characterising the structure of the material. This was first done by powder X-ray diffraction, the Rietveld difference plot and refinement tables can be seen below.

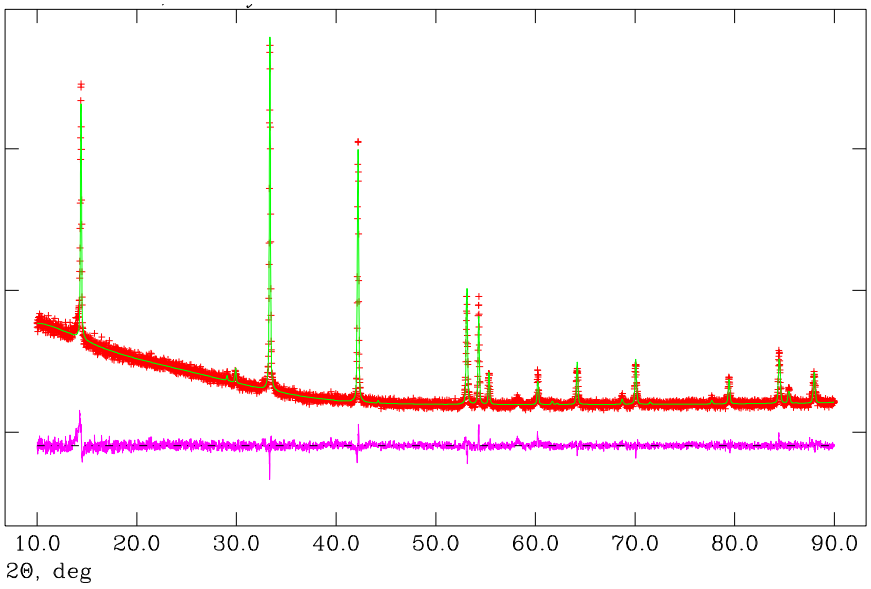

Figure 4.10: Difference plot for Rietveld refinement of PXRD pattern of $LiV_{0.5}Ti_{0.5}S_2$.

$LiV_{0.5}Ti_{0.5}S_2$: Space Group		P -3 m 1
Lattice Parameters -	**a**	3.4450(1) Å
	c	6.1582(4) Å
Refinement parameters -	χ^2	1.165
	wR_p	6.03%
	R_p	4.68%

Atom	X	Y	Z	Site Multiplicity	Fractional Occupancy	U_{iso} (Fixed)
Li	0	0	0.5	1	1	0.02
V/Ti	0	0	0	1	0.5/0.5	0.02
S	0.3333	0.6666	0.235(3)	2	1	0.02

Table 4.2: Refinement parameters of PXRD pattern for $LiV_{0.5}Ti_{0.5}S_2$.

The structure of $LiVS_2$ with expanded lattice parameters, see Table 3.1, was used as the starting model and the model was refined against the data giving a good agreement of $\chi^2 = 1.165$. The occupancies of lithium, titanium and vanadium were not refined. Like in $LiVS_2$ the thermal parameters were not refined. The X-ray diffraction data confirms that $LiV_{0.5}Ti_{0.5}S_2$ adopts the same structure as $LiVS_2$, with expanded **a** and **c** lattice parameters. X-ray diffraction carried out on cycled material is outlined in Section 4.6.

4.4.2 Neutron Diffraction

To obtain accurate values for lithium, titanium and vanadium occupancy, as well as thermal parameters, powder neutron diffraction was carried out, the Rietveld difference plot for bank 5 and refinement tables can be seen below.

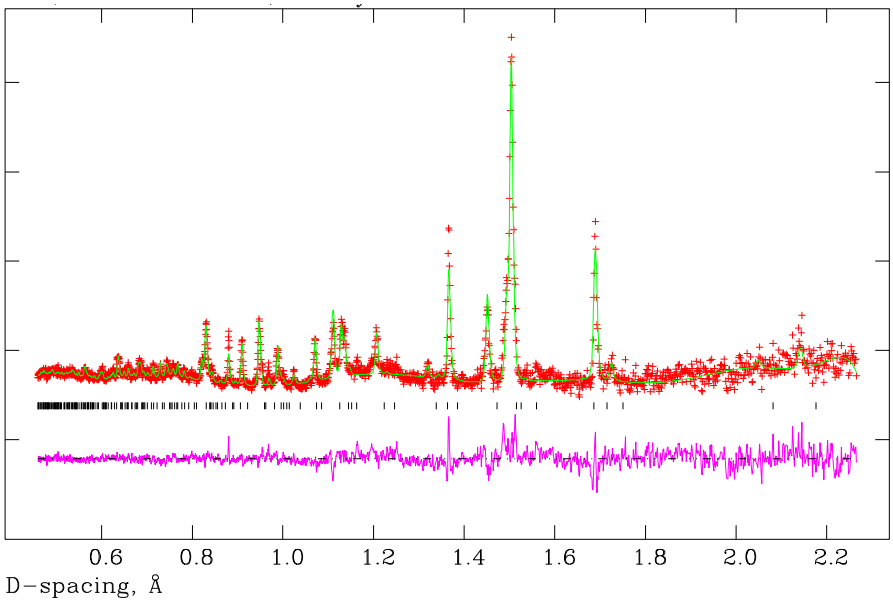

Figure 4.11: Difference plot for Rietveld refinement of PND pattern of $LiV_{0.5}Ti_{0.5}S_2$.

$LiV_{0.5}Ti_{0.5}S_2$: Space Group		P -3 m 1
Lattice Parameters -	**a**	3.4476(4) Å
	c	6.1523(9) Å
Refinement parameters -	χ^2	1.047
	wR_p	5.43%
	R_p	7.02%

Atom	X	Y	Z	Site Multiplicity	Fractional Occupancy	U_{iso}
Li	0	0	0.5	1	0.92(3)	0.023(2)
V/Ti	0	0	0	1	0.51/0.49(2)	0.013(1)
S	0.3333	0.6666	0.2322(5)	2	1	0.0088(4)

Table 4.3: Refinement parameters of PND pattern for $LiV_{0.5}Ti_{0.5}S_2$.

As expected there is very good agreement between the neutron and X-ray data. On first glance it appears there are issues with the difference curve in Figure 4.11, however, on closer inspection it is clear these are due to the background which is uneven due to the quartz capillary. The titanium – vanadium ratio was found to be 50/50 within the error of the refinement. ICP could be carried out in the future to confirm this and to accurately find the lithium content. The thermal parameters of lithium and sulphur are similar to the values seen in the neutron refinement of $LiVS_2$ in Chapter 3, however, the transition metals values differ considerably. A possible explanation for this is that vanadium does not scatter neutrons so is effectively

"invisible" in neutron diffraction; this results in the thermal parameter for vanadium being inaccurate. In the refinement of $LiV_{0.5}Ti_{0.5}S_2$, as vanadium and titanium share a site, they were presumed to have the same thermal parameter and as titanium does scatter neutrons the thermal parameter will be more accurate.

4.5 Electrochemical performance of optimised $LiV_{0.5}Ti_{0.5}S_2$

$LiV_{0.5}Ti_{0.5}S_2$ has now been optimised and structurally characterised. While the electrochemical performance of $LiV_{0.5}Ti_{0.5}S_2$ was touched upon in Section 4.3, it will now be analysed in greater depth. Load curves for the 1st, 2nd, 5th and 10th cycles for $LiV_{0.5}Ti_{0.5}S_2$ at a rate of 100 mAg^{-1} are presented on Figure 4.12.

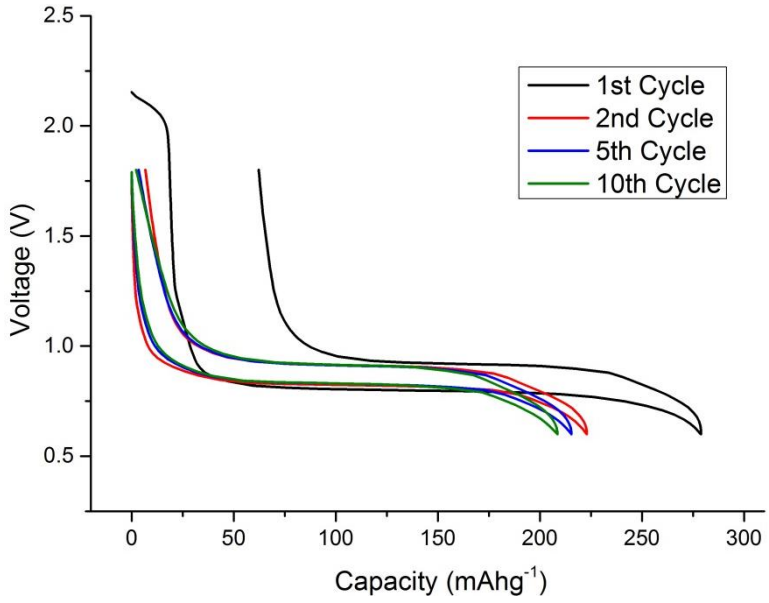

Figure 4.12: Load curves of the 1st, 2nd, 5th and 10th cycle of $LiV_{0.5}Ti_{0.5}S_2$ at a rate of 100 mAg^{-1}.

The data for 100 mAg^{-1} are presented here as it is the standard rate used in many of the comparisons that follow in this chapter. The differences in the electrochemistry at slower and faster rates are discussed below.

The general appearance of the $LiV_{0.5}Ti_{0.5}S_2$ load curves is similar to those of $LiVS_2$. There is a high voltage plateau at ~ 2.1 V due to the $M^{4+/3+}$ redox couple as the material is slightly lithium

deficient. This plateau "contributes" ~20 $mAhg^{-1}$ of capacity which infers that the stoichiometry of the material is $Li_{0.91}V_{0.5}Ti_{0.5}S_2$, this is in very good agreement with the neutron refinement data in the section above. In contrast to $LiVS_2$, there is only a small change in operating voltage between 1st cycle and subsequent cycles. This may be due to the lack of vanadium trimers, and their break-up, in $LiV_{0.5}Ti_{0.5}S_2$ compared to $LiVS_2$. On the first cycle intercalation occurs at 0.8 V and deintercalation at 0.92 V. On the second cycle intercalation occurs at 0.82 V and deintercalation at 0.91 V and it does not change from these values on further cycling. At slower rates the voltages of intercalation and deintercalation are at slightly lower voltages but the polarisation settles at ~ 0.09 V after the first cycle in all cases. Unlike, $LiVS_2$ increasing the rate to 100 mAg^{-1} does not lead to a more "sloping" plateau and increased polarisation but this is observed at rates of 200 mAg^{-1} and above.

An irreversible capacity loss of 42 $mAhg^{-1}$ is observed on the first cycle, more than is observed for $LiVS_2$ at the same rate. The difference is due to $LiV_{0.5}Ti_{0.5}S_2$ having to operate at a lower voltage, this in turn results in more SEI layer formation. At the slower rate of 50 mAg^{-1} the irreversible capacity loss is slightly larger, due to increased SEI layer formation from being at low voltages for a greater absolute period of time on the first discharge. SEI layer formation will be discussed in more detail in the following section.

The performance of $LiV_{0.5}Ti_{0.5}S_2$ at various rates is presented in Figure 3.13. All cells were cycled between 1.8 V and 0.6 V.

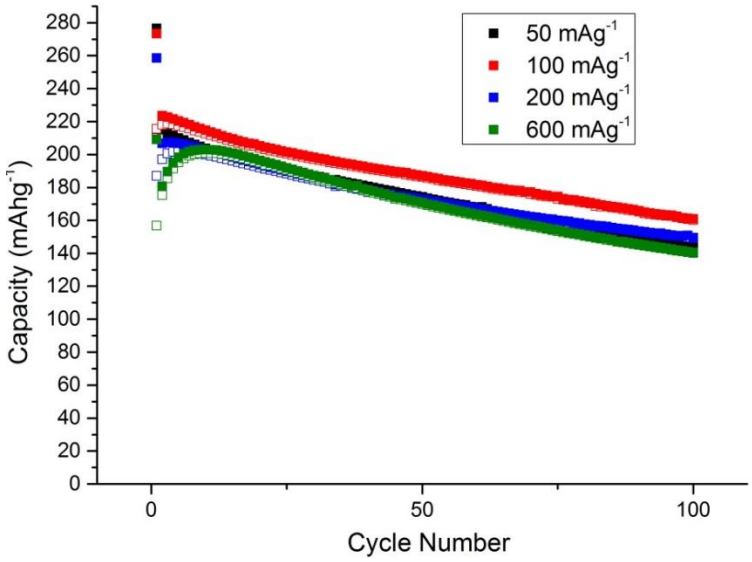

Figure 4.13: Variation of capacity with cycle number for $LiV_{0.5}Ti_{0.5}S_2$ at various rates of charge/discharge. Closed squares correspond to intercalation and open squares to deintercalation.

As can be seen in Figure 3.13, at the slow rate of 50 mAg^{-1} $LiV_{0.5}Ti_{0.5}S_2$ displays a reversible capacity of 212 $mAhg^{-1}$ with a capacity loss of 0.68 $mAhg^{-1}$ per cycle. When the rate is increased to 100 mAg^{-1} the reversible capacity increases to 220 $mAhg^{-1}$ (99% the theoretical capacity) and the capacity loss is reduced to 0.60 $mAhg^{-1}$ per cycle. As noted above, at the slower rate of 50 mAg^{-1} there is a slightly larger first cycle irreversible capacity compared to 100 mAg^{-1} due to increased SEI layer formation/electrolyte decomposition. This increased SEI layer formation is also responsible for the increase in capacity fade at the slower rate, this was also seen for $LiVS_2$ in the previous chapter. The lower absolute capacity is also presumably due to this as the thicker layer formed on first discharge leads to less lithium insertion/extraction on subsequent cycles.

When the rate is increased past 100 mAg^{-1} there is excellent retention of the maximum capacity achieved, with the peak reversible discharge capacity being ~ 205 $mAhg^{-1}$ at 200 mAg^{-1} (taken as C-rate for this material) and ~ 200 $mAhg^{-1}$ at 600 mAg^{-1}. As seen for $LiVS_2$ due to increased polarisation at higher rates cutting off capacity on the first discharge it takes multiple cycles for electrodes operating at fast rates to achieve their peak capacity. However, the effect is not as

severe as $LiVS_2$ and rates of up to 600 mAg^{-1} can be used without a slow rate "breaking in" cycle (as opposed to only 200 mAg^{-1} for $LiVS_2$). The capacity loss at C-rate is virtually the same as C/2, ~ 0.62 $mAhg^{-1}$ per cycle, but this increases slightly at 3C to ~ 0.7 $mAhg^{-1}$ per cycle.

While the performance of $LiV_{0.5}Ti_{0.5}S_2$ is good there is a steady capacity fade at all rates. Figure 4.14 shows the change of the voltage profile on cycling to look for possible explanations for the capacity fade. The load curves of the 2nd and 50th cycles are compared below in Figure 4.14a, while the differential capacity plots of the 20th, 40th, 60th, 80th and 100th cycles are presented in Figure 4.14.b.

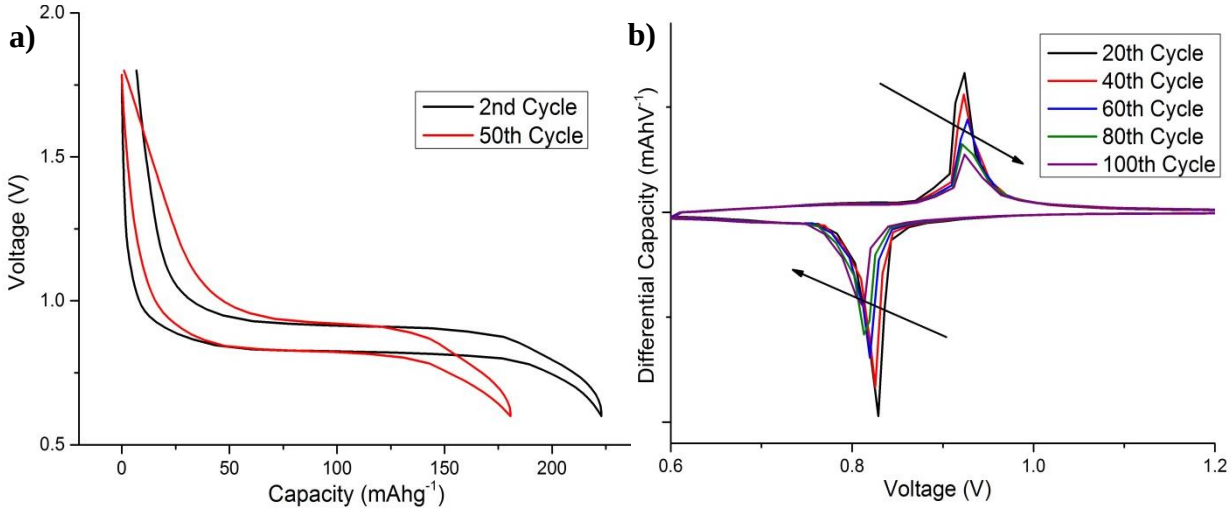

Figure 4.14: a) Load curves of the 2nd and 50th cycle and b) differential capacity plots of the 20th, 40th, 60th, 80th and 100th cycles of $LiV_{0.5}Ti_{0.5}S_2$ at a rate of 100 mAg^{-1}.

The general shape of the load curve is the same after 50 cycles but there are several significant differences. Most notably at the end of charge there is rise in the voltage and there is a significant sloping region that covers the final~ 60 $mAhg^{-1}$, this increases gradually over the course of cycling. The rise in voltage combined with the same voltage cut-off results in slightly less capacity on the charge curve than the discharge curve every cycle. Therefore slightly less lithium deintercalates than intercalates every cycle and this leads to the capacity fade. The reason for the rise in voltage is probably due to a small amount of SEI layer formation/electrolyte decomposition every cycle. The differential capacity plot, Figure 4.14b,

shows that there is a gradual increase in polarization over the course of cycling; this also suggests an increase in the SEI layer on the electrode surface. As the rate of charge/discharge is increased there is also a growth in the rate of polarisation increase. This leads to the increased capacity fade seen for the cells cycled at 600 mAg^{-1}, Figure 4.13, as an increasing amount of capacity is "cut-off" by the 0.6 V limit. The growth in the rate of polarisation increase at higher rates could be related to increased electrochemical grinding at higher rates. As the electrode is broken up there is an increase surface area and therefore an increase in the SEI layer. It is possible that future optimisation of the electrolyte can produce an electrolyte that does not create a SEI layer on every cycle and therefore limits the capacity loss.

Now that the electrochemical performance of $LiV_{0.5}Ti_{0.5}S_2$ has been documented, its performance can be compared to $LiVS_2$. As has been covered extensively above the polarisation in $LiV_{0.5}Ti_{0.5}S_2$ is much lower than $LiVS_2$ and lithium intercalation/deintercalation takes place at lower voltages. Figure 4.15 below shows the cycling performance of $LiV_{0.5}Ti_{0.5}S_2$ and $LiVS_2$ at 100 mAg^{-1} and 200 mAg^{-1}.

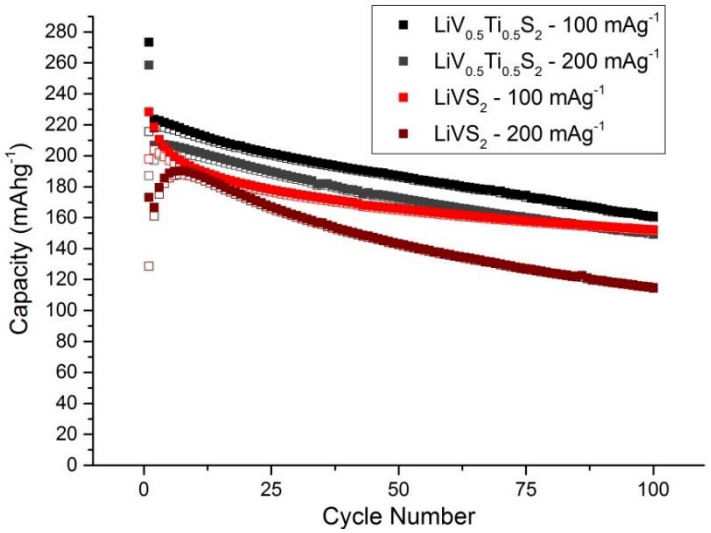

Figure 4.15: Variation of capacity with cycle number for $LiV_{0.5}Ti_{0.5}S_2$ and $LiVS_2$ at various rates of charge/discharge. Closed squares correspond to intercalation and open squares to deintercalation.

The $LiV_{0.5}Ti_{0.5}S_2$ data was cycled between 0.6 V and 1.8 V. The 100 mAg^{-1} $LiVS_2$ data was cycled between 0.8 V and 1.8 V, while the 200 mAg^{-1} $LiVS_2$ data was cycled between 0.8 V and 2.2 V. As can be seen in the figure above at 100 mAg^{-1} $LiV_{0.5}Ti_{0.5}S_2$ displays a superior reversible capacity of 220 $mAhg^{-1}$ compared to 205 $mAhg^{-1}$ for $LiVS_2$. Over 100 cycles $LiV_{0.5}Ti_{0.5}S_2$ and $LiVS_2$ display a virtually identical net capacity fade, although the degree of fading is not uniform across the 100 cycles. $LiVS_2$ shows greater capacity fade over the first 20 cycles but shows very little capacity fade from cycle 75 onwards. The larger capacity loss over the first 20 cycles in $LiVS_2$ could be due to the large change in polarisation and particle size not seen in $LiV_{0.5}Ti_{0.5}S_2$, see SEM images in Section 4.6.4 below. The superior capacity retention of $LiVS_2$ over the subsequent cycles could be due to operating at a higher voltage and therefore not subject to the constant SEI layer formation as described above.

At 200 mAg^{-1} $LiV_{0.5}Ti_{0.5}S_2$ again displays a superior reversible capacity, 205 $mAhg^{-1}$ compared to 185 $mAhg^{-1}$ for $LiVS_2$. $LiV_{0.5}Ti_{0.5}S_2$ electrodes also display greater capacity retention and reach their maximum capacity several cycles earlier. While $LiV_{0.5}Ti_{0.5}S_2$ still produces high capacities above 200 mAg^{-1} the cycling performance of $LiVS_2$ above 200 mAg^{-1} is poor. The overall performance of $LiV_{0.5}Ti_{0.5}S_2$ is superior to that of $LiVS_2$ despite operating at a lower voltage and therefore subject to greater SEI layer formation on the electrode surface. It is likely that the superior performance is due to the lack of change in the electrochemistry and electrode morphology observed for $LiV_{0.5}Ti_{0.5}S_2$ electrodes. $LiVS_2$ shows large polarisations at higher rates, possibly indicating issues involving vanadium trimers discussed in the previous chapter. This combined with increased break-up of $LiVS_2$ electrodes can explain why $LiV_{0.5}Ti_{0.5}S_2$ displays much better cycling performance at higher rates.

The above data demonstrates that $LiV_{0.5}Ti_{0.5}S_2$ performs very well as an anode material for lithium-ion batteries and demonstrates superior performance to $LiVS_2$. However, it is important to note that $LiVS_2$ has a larger particle size than $LiV_{0.5}Ti_{0.5}S_2$ (see Figures 3.13 and 4.23). This

is important as $LiVS_2$ particles break-up on cycling while $LiV_{0.5}Ti_{0.5}S_2$ particles do not and therefore some of the superior performance demonstrated by $LiV_{0.5}Ti_{0.5}S_2$ could be due its smaller particle size, particularly at faster rates where the effects of electrochemical grinding can be more severe. Attempts to ball mill $LiV_{0.5}Ti_{0.5}S_2$ lead to a considerable reduction in capacity even after 15 minutes and little-to-no observable particle size reduction. This could possibly be due to $LiV_{0.5}Ti_{0.5}S_2$ reacting with moisture on the surface of the milling jar. Further ball milling experiments should be carried out in the future on both $LiVS_2$ and $LiV_{0.5}Ti_{0.5}S_2$ to find the optimum particle size of these materials.

It is important at this point to confirm that $LiV_{0.5}Ti_{0.5}S_2$ is the best performing composition of the $LiV_{1-x}Ti_xS_2$ solid solution. To do this $LiV_{0.5}Ti_{0.5}S_2$ will be compared to $LiV_{0.6}Ti_{0.4}S_2$ and $LiV_{0.4}Ti_{0.6}S_2$. $LiV_{0.6}Ti_{0.4}S_2$ and $LiV_{0.4}Ti_{0.6}S_2$ were also found to have an optimal synthesis temperature of 1050 ^oC. Figure 4.16 presents the 1st cycle load curves of $LiV_{0.5}Ti_{0.5}S_2$ and $LiV_{0.6}Ti_{0.4}S_2$.

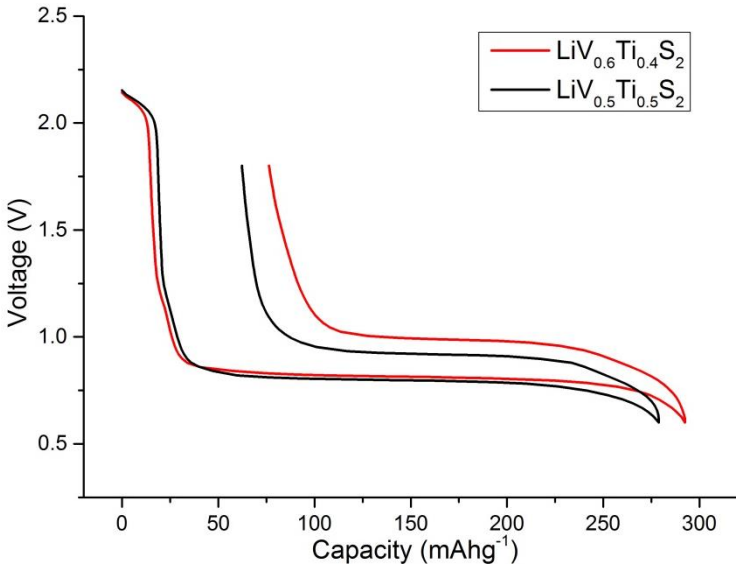

Figure 4.16: 1st cycle load curves of $LiV_{0.5}Ti_{0.5}S_2$ and $LiV_{0.6}Ti_{0.4}S_2$ at a rate of 100 mAg^{-1}.

$LiV_{0.5}Ti_{0.5}S_2$ has several advantages as an electrode material compared to $LiV_{0.6}Ti_{0.4}S_2$. While on first glance $LiV_{0.6}Ti_{0.4}S_2$ appears to have a larger initial capacity, this is purely due to increased irreversible capacity loss on the first cycle. The first cycle polarisation of $LiV_{0.6}Ti_{0.4}S_2$

is ~ 0.1 V larger than $LiV_{0.5}Ti_{0.5}S_2$, and remains slightly larger on extended cycling. Crucially, the voltage at which deintercalation takes place is higher for $LiV_{0.6}Ti_{0.4}S_2$ than $LiV_{0.5}Ti_{0.5}S_2$, therefore the voltage window is decreased when used in a full cell. On extended cycling, where an increasingly large portion of capacity is due to the "sloping" region between the plateau and 1.8 V (Figure 4.14), this issue is intensified and even more of the capacity of $LiV_{0.6}Ti_{0.4}S_2$ is at higher voltages. The capacity retention of $LiV_{0.6}Ti_{0.4}S_2$ is virtually the same as $LiV_{0.5}Ti_{0.5}S_2$. In summary, $LiV_{0.6}Ti_{0.4}S_2$ shows an increase in irreversible capacity loss, polarisation and deintercalation voltage, with no increase in reversible capacity or capacity retention.

Turning now to the titanium rich side of $LiV_{0.5}Ti_{0.5}S_2$, Figure 4.17 presents cycling data for $LiV_{0.5}Ti_{0.5}S_2$ and $LiV_{0.4}Ti_{0.6}S_2$ at a rate of 100 mAg^{-1} between 1.8 V and 0.6 V.

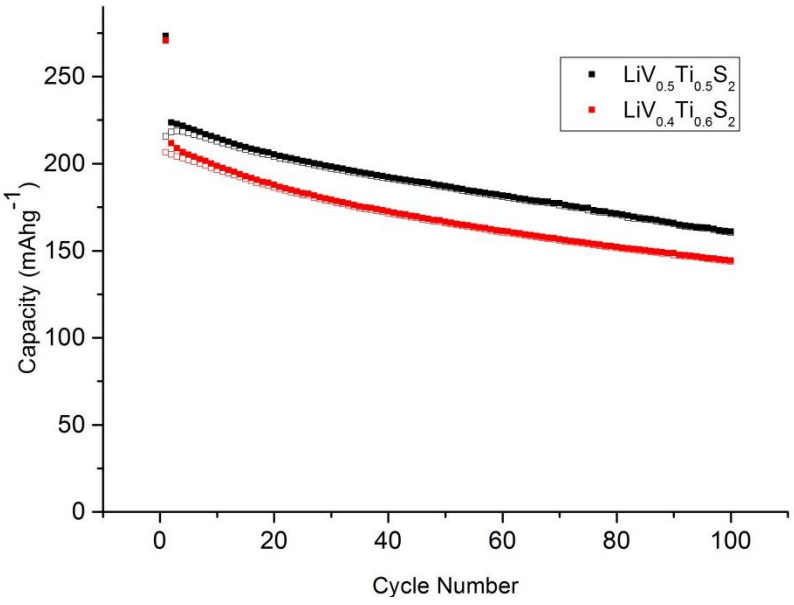

Figure 4.17: Variation of capacity with cycle number for $LiV_{0.5}Ti_{0.5}S_2$ and $LiV_{0.4}Ti_{0.6}S_2$ at a rate of 100 mA g^{-1}. Closed squares correspond to intercalation and open squares to deintercalation.

The potentials of intercalation and deintercalation are slightly lower for $LiV_{0.4}Ti_{0.6}S_2$ than $LiV_{0.5}Ti_{0.5}S_2$ as would be expected by the general trend seen with increasing titanium content, due to the higher effective nuclear charge of Ti leading to higher energy d-states[2]. This results in capacity being "lost" when a lower voltage cut-off of 0.6 V is used for $LiV_{0.4}Ti_{0.6}S_2$ as some intercalation of Li^+ happens below this voltage. This leads to the cycling performance seen in

the figure above where $LiV_{0.5}Ti_{0.5}S_2$ has clearly superior cycling performance. Using a lower voltage cut off of 0.5 V results in increased capacity for the first few cycles but like $LiV_{0.5}Ti_{0.5}S_2$ this leads to increased capacity fade (see Figure 4.9). The difference in capacity between the two materials (Figure 4.17) is more significant than the differences in intercalation/deintercalation voltages, and therefore $LiV_{0.5}Ti_{0.5}S_2$ is judged the superior of the two materials.

It is important to note that the precise qualities required from an anode material will vary somewhat with the application. The decision to focus on $LiV_{0.5}Ti_{0.5}S_2$, as opposed to $LiV_{0.6}Ti_{0.4}S_2$ and $LiV_{0.4}Ti_{0.6}S_2$, is based on the view that its properties are superior for the majority of situations. There may well be specific circumstances where the benefits of the lower operating voltage of $LiV_{0.4}Ti_{0.6}S_2$ may be important enough to overcome its drawbacks.

4.6 The electrochemical process of $LiV_{0.5}Ti_{0.5}S_2$

The above sections in this chapter show that $LiV_{0.5}Ti_{0.5}S_2$ can display very attractive electrochemical properties. In this section the mechanism of lithium intercalation will be explored in greater depth.

4.6.1 Ex-situ X-ray diffraction

X-ray diffraction was carried out on cycled electrode material to monitor structural changes on cycling. Pellet electrodes were used as the low amount of material used in cast electrodes made gathering sufficient material for X-ray diffraction difficult. To ensure full intercalation/deintercalation of lithium cells were cycled at the slow rate of 15 mAg^{-1}. As discussed in Section 3.5 no difference was observed in the fundamental electrochemistry between pellet and cast electrodes. Cells were cycled to a specified point on the $LiV_{0.5}Ti_{0.5}S_2$ load curve and then transferred to an argon filled glove box. All electrode materials where the

lithium content was > 1 were found to be very air sensitive, even momentary exposure to air would result in spontaneous oxidation to $LiV_{0.5}Ti_{0.5}S_2$. Once in the argon filled glove box, cells were carefully opened and the pellet electrode removed. The electrode was subsequently washed with dimethyl carbonate (DMC), to remove electrolyte, dried under vacuum and ground using an agate pestle and mortar. Samples were then loaded in to glass capillaries and measurements were carried out on a Stoe STADI/P diffractometer using Cu $K\alpha_1$ radiation.

Figure 4.18 shows the change in structure of $LiV_{0.5}Ti_{0.5}S_2$ on the first cycle. The letters labelled on the load curve in part a) correspond to the X-rays in part b). The labels on the right of the XRD pattern show the amount of charge passed according to the load curve in a).

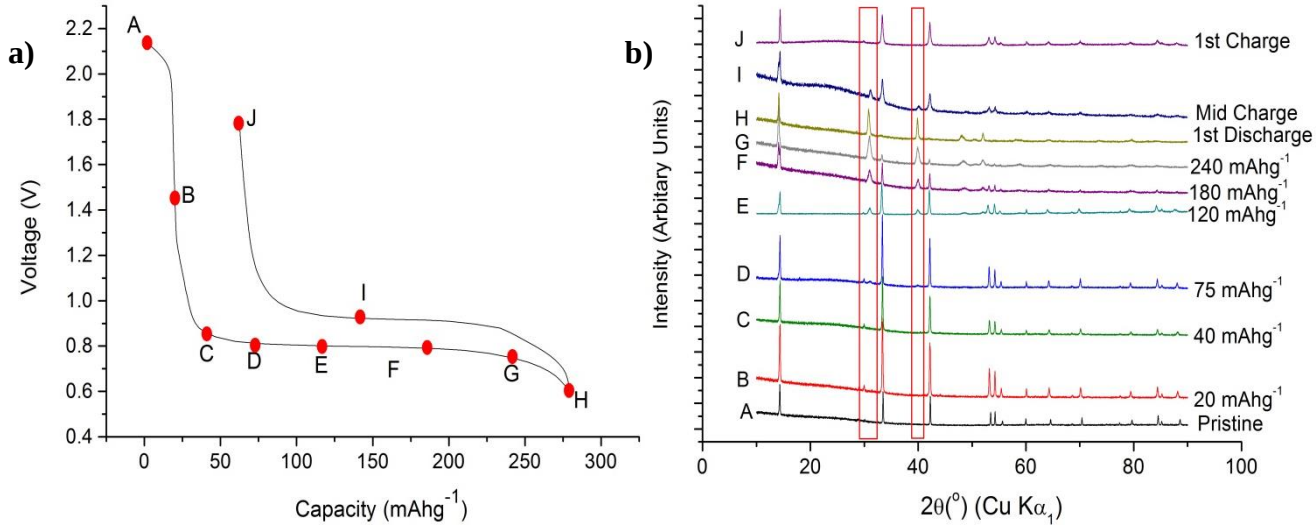

Figure 4.18: Structural change in $LiV_{0.5}Ti_{0.5}S_2$ on the first cycle, a) load curve and b) x-ray diffraction. The red rectangles show the main $Li_2V_{0.5}Ti_{0.5}S_2$ peaks.

There is a slight change in peak positions between points A and B as Li^+ is inserted into lithium deficient $Li_{0.92}V_{0.5}Ti_{0.5}S_2$ to become $LiV_{0.5}Ti_{0.5}S_2$. This coincides with a change in lattice parameters from **a** = 3.4450(1) Å and **c** = 6.1582(2) Å to **a** = 3.4377(4) Å and **c** = 6.1591(2) Å. There is no change in the positions of the $LiV_{0.5}Ti_{0.5}S_2$ peaks from point B onwards. Across the intercalation plateau, points C to H, the intensity of the $LiV_{0.5}Ti_{0.5}S_2$ peaks decrease while new peaks grow. These new peaks correspond to the $Li_2V_{0.5}Ti_{0.5}S_2$ phase; the most prominent peaks are highlighted in Figure 4.18b. This confirms lithium intercalation into $LiV_{0.5}Ti_{0.5}S_2$ occurs

via a two phase process. At point H no $LiV_{0.5}Ti_{0.5}S_2$ can be observed and lithium intercalation appears to be complete. The X-ray mid charge, point I, shows that the deintercalation process also proceeds via a two phase mechanism. At the end of the first charge, point J, no $Li_2V_{0.5}Ti_{0.5}S_2$ can be seen and pure phase $LiV_{0.5}Ti_{0.5}S_2$ has been reformed with the same lattice parameters as at point B. The lack of change in the X-ray patterns at point B and C, as well as the ratio of $LiV_{0.5}Ti_{0.5}S_2$ and $Li_2V_{0.5}Ti_{0.5}S_2$ phases along the plateau, will discussed in depth later in this section.

Analysis of Figure 4.18b by eye shows that points A-C and J can be described as being pure $LiV_{0.5}Ti_{0.5}S_2$ point H as being pure $Li_2V_{0.5}Ti_{0.5}S_2$ and the remaining points being a mixture of the two phases. To gain a better understanding of the structure of $Li_2V_{0.5}Ti_{0.5}S_2$ Rietveld analysis was carried out on point H, the fully discharged sample. Li_2VS_2 was used as the starting model and the model was refined against the data giving a good agreement of $\chi^2 = 1.085$. The Difference plot and table of refinement parameters are below:

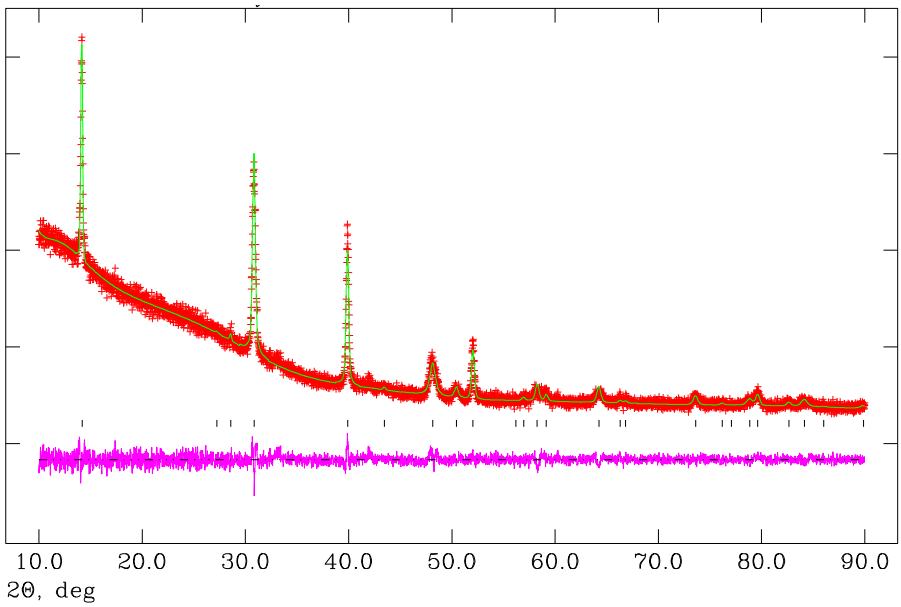

Figure 4.20: Difference plot for Rietveld refinement of PXRD pattern of $Li_2V_{0.5}Ti_{0.5}S_2$.

$Li_2V_{0.5}Ti_{0.5}S_2$: Space Group		P -3 m 1				
Lattice Parameters -	**a**	3.7786(2) Å				
	c	6.2451(5) Å				
Refinement parameters -	χ^2	1.085				
	wR_p	5.23%				
	R_p	3.99%				
Atom	X	Y	Z	Site Multiplicity	Fractional Occupancy	U_{iso}
Li	0.6666	0.3333	0.365(2)	2	1	0.02
V/Ti	0	0	0	1	0.5/0.5	0.02
S	0.3333	0.6666	0.2313(5)	2	1	0.02

Table 4.4: The refinement parameters of the PXRD pattern of $Li_2V_{0.5}Ti_{0.5}S_2$.

The Rietveld refinement confirms that $Li_2V_{0.5}Ti_{0.5}S_2$ adopts the same structure as Li_2VS_2. To accommodate the extra Li^+ intercalated into the structure, the existing lithium moves from octahedral sites to tetrahedral sites. There is no change in the transition metal position and only a very slight change in the position of the sulphide anions. The extra lithium leads to an expansion of the unit cell compared to $LiV_{0.5}Ti_{0.5}S_2$. The refined lattice parameters of $Li_2V_{0.5}Ti_{0.5}S_2$: **a** = 3.7786(2) Å and **c** = 6.2451(5) Å are fairly similar to the literature values of Li_2VS_2: **a** = 3.830 Å and **c** = 6.215 Å. The expansion in **c** seen in $Li_2V_{0.5}Ti_{0.5}S_2$ compared to Li_2VS_2 is consistent with the difference between as prepared $LiV_{0.5}Ti_{0.5}S_2$ and $LiVS_2$.

The intercalation of lithium into $LiV_{0.5}Ti_{0.5}S_2$ results in a unit cell expansion of 23%. This is relatively large but the process is highly reversible and it is nowhere near the scale seen in alloying and conversion reactions: see further discussion in Chapter 1. However, it is still surprising a two-phase reaction that has such a large volumes expansion displays such good capacity retention, especially at high rates. By comparison $Li_4Ti_5O_{12}$, which operates by a well understood two-phase mechanism, operates by a 'zero strain' process and shows virtually no volume expansion upon lithium intercalation[5]. The explanation for the good performance of $LiV_{0.5}Ti_{0.5}S_2$ despite the large volume expansion may be that the expansion in **c** is only ~ 1.5%. The expansion along **a** is larger at ~ 10% and is associated with the elongation of the (M)-S bond as formally $(M)^{3+}$ is reduced to $(M)^{2+}$. As the d-bands in sulphides are relatively wide

compared with oxides, the electrons are well delocalized across the (M)-S_2 slabs. This leads to a larger expansion then might be expected for an oxide.

As discussed above, all points on the load curve of $LiV_{0.5}Ti_{0.5}S_2$ can be described as pure $LiV_{0.5}Ti_{0.5}S_2$, pure $Li_2V_{0.5}Ti_{0.5}S_2$ or a mixture of the two. This allowed for two phase refinements to be carried out on all the points between B and H to calculate the phase ratio of $LiV_{0.5}Ti_{0.5}S_2$ to $Li_2V_{0.5}Ti_{0.5}S_2$ at different points on discharge. Knowing the theoretical capacity of the intercalation of 1 Li^+ in to the structure (222 mA h g^{-1}) allows the calculation of how much charge should have been passed at that point in the intercalation process. These refined values can then be compared to the actual value observed electrochemically. The difference between the refined values and the observed value gives an indication of the amount of electrolyte decomposition and SEI layer formation and thus irreversible capacity loss that has taken place. The table below shows the amounts of each phase and capacities for points B – H in Figure 4.18. The 20 $mAhg^{-1}$ contributed from the $M^{4+/3+}$ redox couple has been subtracted as it is constant across all points.

Point on Load Curve	$LiV_{0.5}Ti_{0.5}S_2$ (%)	$Li_2V_{0.5}Ti_{0.5}S_2$ (%)	Capacity from load curve minus the $M^{4+/3+}$ couple (mA h g^{-1})	Capacity of Li^+ intercalated from X-ray analysis (mA h g^{-1})	Difference (mA h g^{-1})
B	100	0	0	0	0
C	100	0	20	0	20
D	87	13	50	28	22
E	68	32	95	72	23
F	40	60	155	133	22
G	12	88	215	195	20
H	3	97	258	216	42

Table 4.5: Percentage of $LiV_{0.5}Ti_{0.5}S_2$ to $Li_2V_{0.5}Ti_{0.5}S_2$ and amount of capacity passed at various points on the load curve in Figure 4.20.

Between points B and C there is no change in the X-ray diffraction patterns but there is a feature on the load curve that begins at about ~ 1.2 V and produces 20 $mAhg^{-1}$ of capacity. This suggests that this feature and capacity correspond to electrolyte decomposition and SEI layer

formation. This is consistent with other anode materials which also show electrolyte decomposition/SEI layer formation that begins at ~ 1 V vs Li^+/Li^0.

Between points C and G there is constant growth of the $Li_2V_{0.5}Ti_{0.5}S_2$ phase and the difference between the calculated and observed capacity is roughly constant. This indicates that no significant electrolyte decomposition or SEI layer formation occurs between points C and G. Given that there is only a small change in voltage between these points, and the voltage is not at low enough potentials to see large amounts of electrolyte decomposition, this is not surprising. The small fluctuations in the difference between calculated and observed capacity across the plateau can be assigned to small amount of inaccuracy when refining the phase fractions of the two phases.

The remainder of the electrolyte decomposition/SEI layer formation, 22 $mAhg^{-1}$, takes place between points G and H, in accord with the slow downturn in capacity. Extending the lower voltage cut-off below 0.6 V increases this electrolyte reduction and hence leads to increased capacity loss, as seen in Figure 4.9. It may be tempting to suggest raising the lower voltage cut-off to reduce irrepressible capacity loss. However, as the refinement data shows that point H is not actually $Li_2V_{0.5}Ti_{0.5}S_2$, but is slightly lithium deficient, raising the cut-off voltage would also reduce intercalation of Li^+ into the material and therefore the reversible capacity would be reduced as well.

X-ray diffraction measurements were also carried out after multiple cycles. Figure 4.20 shows XRD patterns of the pristine material, 1st cycle and 10th cycle.

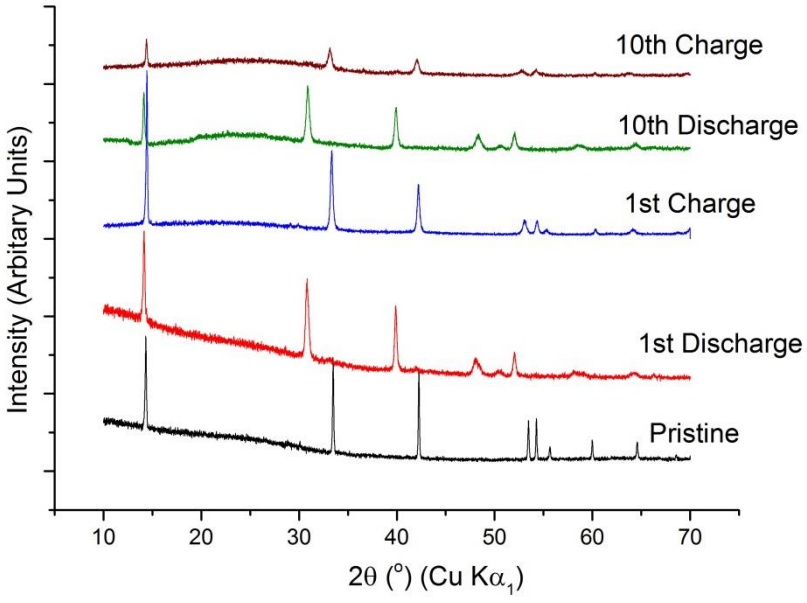

Figure 4.20: X-ray diffraction patterns of pristine $LiV_{0.5}Ti_{0.5}S_2$ and after 1 and 10 cycles.

The X-ray patterns above show that after 10 cycles there are no significant changes in the structure of either $LiV_{0.5}Ti_{0.5}S_2$ or $Li_2V_{0.5}Ti_{0.5}S_2$. There is a slight change in the lattice parameters of pristine $LiV_{0.5}Ti_{0.5}S_2$ and after 1 cycle. This is due to the as-prepared material being slightly lithium deficient and the electrode material after the 1st charge being stoichiometric. No change was observed in the peak positions between 1st charge and 10th charge. There is observable peak broadening between the pristine sample and all cycled material that implies a reduction in particle size occurs on the 1st discharge, this will be investigated further by SEM below. The peak width at half maximum almost doubles between the as-prepared sample and after 1 cycle. It is difficult to compare the 1st and 10th charges due to the loss in peak intensity, however, there is virtually no change between 1st and 10th discharge which implies that there is very little change in particle size after the first cycle. There is a general loss in peak intensity on cycling which is often seen for cycled electrode materials.

It should be noted that while the ex-situ X-ray diffraction shows a clear two phase mechanism it is possible that the process is actually more complicated but the system relaxes to two phases when the cell is removed from the testing equipment. In-situ X-ray diffraction has been used to

confirm the presence of meta-stable phases[6] and other reaction routes[7] in other battery materials that cannot be seen by ex-situ diffraction. In-situ X-ray diffraction should be carried out on $LiV_{0.5}Ti_{0.5}S_2$ in the future to confirm the process is two phase.

4.6.2 The effect of the carbon additive on irreversible capacity loss

It is important to remember that in any electrode that uses Super S carbon as a conductive additive that the carbon has a very high surface area (~45 m^2g^{-1}). This is especially important for sulphides where the particle size is large, see Section 4.6.4. As the surface area of the carbon additive is significantly larger than the surface area of the active material, this results in a situation where even though the carbon additive is only 10% the mass of the electrode it is responsible for a much larger proportion of the surface area. Electrolyte decomposition and SEI layer formation occurs at the surface of the electrode and therefore the greater the surface area the larger the amount of electrolyte decomposition that will take place. To investigate how much of the electrolyte decomposition was due to the Super S carbon additive and how much was inherent to $LiV_{0.5}Ti_{0.5}S_2$, cells were constructed with the same loading of $LiV_{0.5}Ti_{0.5}S_2$ but with the Super S additive removed. For $LiVS_2$ it was not possible to cycle electrodes without a carbon additive due to $LiVS_2$ being an insulator at room temperature. For $LiV_{0.5}Ti_{0.5}S_2$ it was possible to cycle electrodes made with no carbon additive but when using less than 10% carbon they faded badly after the first cycle. The fabrication of cast electrodes without a carbon additive is difficult and leads to a less even coating. Therefore, it was not clear if the capacity fade was due to a problem with conductivity or due to fabrication issues. Figure 4.21 shows the first cycle load curve of a regular $LiV_{0.5}Ti_{0.5}S_2$ electrode and one with no carbon additive.

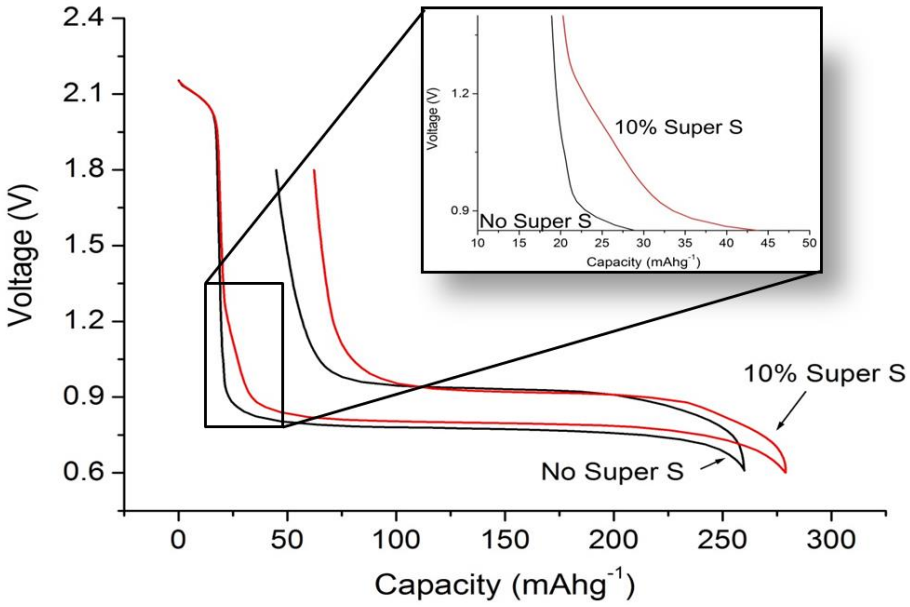

Figure 4.21: Load curves of $LiV_{0.5}Ti_{0.5}S_2$ electrodes with and without Super S additive at a rate of 100 mAg^{-1}. Insert shows difference in capacity between 1.3 V and 0.85 V.

The difference in irreversible capacity between the cells shown in Figure 4.21 is 18 $mAhg^{-1}$. This indicates the irreversible capacity intrinsic to $LiV_{0.5}Ti_{0.5}S_2$ is only 24 $mAhg^{-1}$. The load curves also indicate at which potentials the SEI layer grows on $LiV_{0.5}Ti_{0.5}S_2$ compared to carbon. The electrodes have the same amount of lithium deficiency but begin to diverge at ~ 1.3 volts. The load curve without Super S shows virtually no change in capacity between 1.3 V and 0.85 V, while the other load curve shows significant capacity between those voltages. At 0.85 V the difference in capacity between the two electrodes is ~ 15 $mAhg^{-1}$, implying ¾ of the irreversible capacity seen before the plateau (~ 20 $mAhg^{-1}$ according to the phase fractions in the previous sections) is due to the carbon additive. It follows therefore that the majority of capacity seen at low voltages, after the plateau, is due to the active material.

4.6.3 X-ray Absorption Near Edge Spectroscopy (XANES)

X-ray absorption near edge spectroscopy was carried out at the Diamond Light Source in Didcot, UK in collaboration with Professor Alan Chadwick at the University of Kent.

XANES was carried out on various points on the first discharge with the aim of monitoring the change in the oxidation states of vanadium and titanium. Pellet electrodes were cycled to the required voltage and then removed from the cell. The electrode material was then ground with additional carbon and binder and pressed into a pellet. The pellet was then heat sealed in an aluminium foil bag, to stop contamination from air, and dispatched for the measurement to be carried out. The data processing and analysis was done by Professor Alan Chadwick and co-workers at the University of Kent. Further discussion of XANES can be found in Section 2.4.

The raw data absorption curves can be found in the Appendix A. The energy values presented below are the K-edges and were calculated by using the ½ edge step as the edge. The lithium contents were calculated by using the refined phase fractions at those points in the load curve. Graphs of the calculated energy edge and the calculated lithium content are depicted in Figures 4.22a and 4.22b for vanadium and titanium respectively. Figure 4.22c shows the correlation between V and Ti. The seven points where measurements were collected are presented on a load curve in Figure 4.22d.

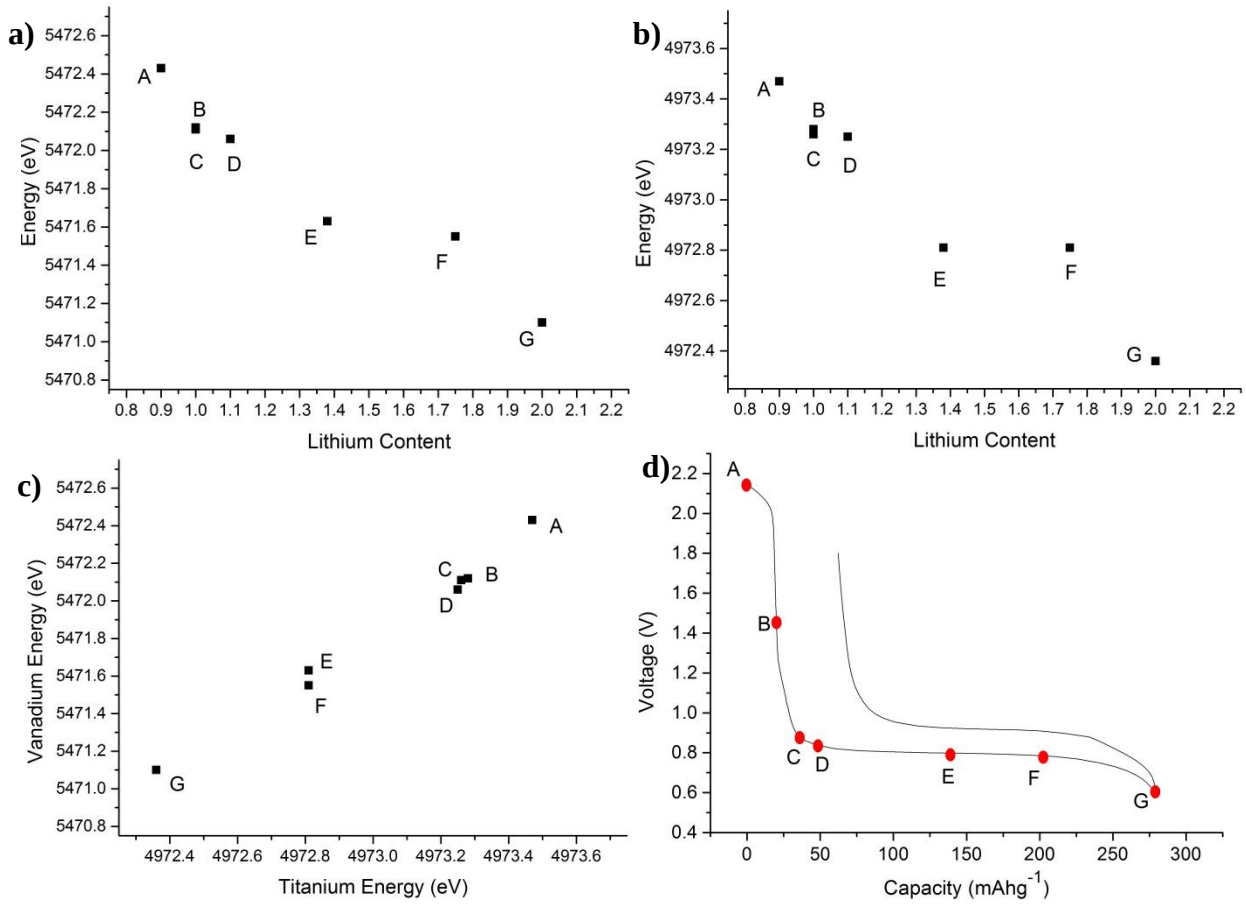

Figure 4.22: XANES data: a) vanadium energy vs lithium content, b) titanium energy vs lithium content, c) correlation of vanadium and titanium energies and d) load curve with measurement points labelled.

The XANES data confirms that pristine $LiV_{0.5}Ti_{0.5}S_2$ is indeed lithium deficient as there is a difference in energy between points A and B. There is virtually no change in vanadium or titanium oxidation states between points B and D. This gives further confirmation that there is no lithium intercalation in to the structure at this point of the load curve. There is a steady change in energy, and therefore oxidation state, between points D - E and point G as would be expected by the change in lithium content. It appears that the sample at point F has partially oxidised as the energy of point F is very close to point E. The correlation plot, Figure 4.22c, shows that the vanadium and titanium correlate very well and shows that the two metals are reduced at the same rate. This is expected as there is only one plateau observed in the electrochemistry.

4.6.4 Scanning Electron Microscopy (SEM)

The SEM image of as-prepared $LiV_{0.5}Ti_{0.5}S_2$ in Section 4.3 showed that $LiV_{0.5}Ti_{0.5}S_2$ varied in size from 5 µm to 50 µm, with the majority of particles being ~ 10 - 20 µm in size. This is slightly smaller than was observed for $LiVS_2$. SEM images of cycled material can be seen below in Figure 4.23. As in the case of $LiVS_2$ in the previous chapter to make the comparison between pristine material and cycled material as easy and relevant as possible the pristine uncycled material was also mixed with Super S carbon and Kynar binder, pressed in to a pellet and placed in to a coin cell.

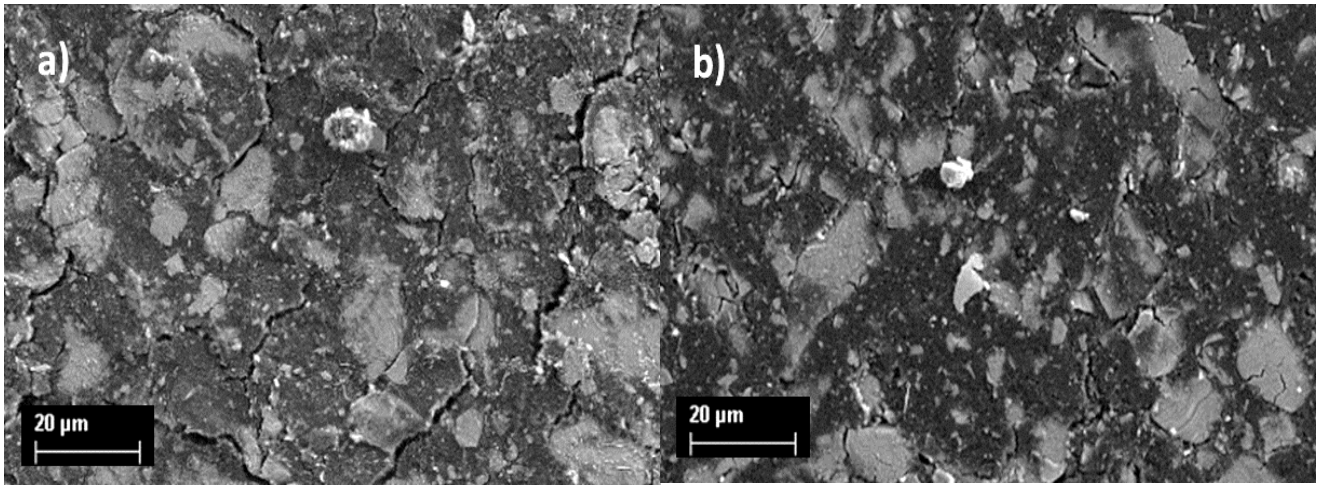

Figure 4.23: SEM images of a) un-cycled $LiV_{0.5}Ti_{0.5}S_2$ and b) $LiV_{0.5}Ti_{0.5}S_2$ after 10 cycles.

The large grey particles are the $LiV_{0.5}Ti_{0.5}S_2$ active material and the smaller dark particles are the carbon additive. It is more difficult to tell with certainty the particle size of pelletised electrodes compared to free-flowing powder due to the particle being pressed into each other and the carbon additive obscuring much of the image. The particles in the both the pristine and cycled material appear to be roughly the same size: 10 – 20 µm. The larger particles of cycled material appear to have broken up a small amount. Comparing the un-cycled material and the electrode after 10 cycles show no large scale change like that seen in $LiVS_2$. The lack of any large reduction in particle size is consistent with the smaller change in polarisation and increased capacity retention over the first 20 cycles seen for $LiV_{0.5}Ti_{0.5}S_2$ compared with $LiVS_2$.

It should be noted that the above electrodes were cycled at a rate of 100 mAg^{-1} and at higher rates there may be more change in the electrode morphology. However, to get the material for SEM, pellet electrode were required and cycling pellet electrodes over 100 mAg^{-1} reduced the capacity of the cell to a point where it was no longer judged to be a fair representation of the material being tested.

4.7 Summary, Conclusions and Future Work

4.7.1 Summary of Results

A range of compositions in the $LiV_{1-x}Ti_xS_2$ solid solution were successfully synthesised and $LiV_{0.5}Ti_{0.5}S_2$ was found to be the most promising anode material and the focus of further investigation. $LiV_{0.5}Ti_{0.5}S_2$ has better capacity retention than compounds with larger amounts of titanium but a lower voltage of intercalation/deintercalation and lower polarisation compared to compounds with more vanadium.

The synthesis of $LiV_{0.5}Ti_{0.5}S_2$ was optimised, with 1050 ^oC found to be the temperature that gives the best electrochemical performance. The structure was characterised via X-ray and neutron diffraction and $LiV_{0.5}Ti_{0.5}S_2$ was found to have the same structure as $LiVS_2$.

The intercalation potential is 0.8 V on the first cycle and this rises to 0.82 on subsequent cycles. Deintercalation shifts from 0.92 V to 0.91 V after the first cycle. Polarisation is small at 0.09 V. The rate performance of $LiV_{0.5}Ti_{0.5}S_2$ is impressive, with reversible capacities of 220 $mAhg^{-1}$ (99% theoretical) achieved at rate of C/2 (100 mA g^{-1}) and 200 $mAhg^{-1}$ achieved at 3C. The capacity loss at C/2 and C-rate is only ~ 0.6 $mAhg^{-1}$ per cycle, this increases slightly at 3C to ~ 0.7 $mAhg^{-1}$ per cycle. The irreversible capacity loss on the first cycle is 42 $mAhg^{-1}$.

Ex-situ X-ray diffraction shows that lithium insertion takes place via a two phase process and $Li_2V_{0.5}Ti_{0.5}S_2$ adopts the same structure as Li_2VS_2. X-ray absorption near edge spectroscopy

(XANES) demonstrates that vanadium and titanium are reduced at the same rate on intercalation of lithium. X-ray refinements and XANES data also show that there is no insertion of lithium at the early part of the plateau at 1.3 V to 0.85 V and that the capacity in this region is due to electrolyte decomposition. The rest of the electrolyte decomposition occurs at lower voltages after the plateau. It has also been demonstrated that over half of the irreversible capacity loss is due to the carbon additive and the irreversible capacity loss due to $LiV_{0.5}Ti_{0.5}S_2$ is only 24 $mAhg^{-1}$. Scanning electron microscopy (SEM) demonstrates that there is no significant change in particle size on cycling.

4.7.2 Comparisons between $LiV_{0.5}Ti_{0.5}S_2$ and other anode materials

The performance of $LiV_{0.5}Ti_{0.5}S_2$ is a significant improvement over any previously reported sulphide anode material. Compared to the $LiVS_2$ and $LiTiS_2$ materials reported by Goodenough and co-workers $LiV_{0.5}Ti_{0.5}S_2$ has better capacity retention at all rates and demonstrates significantly higher capacities at fast rates[1,9]. $LiV_{0.5}Ti_{0.5}S_2$ also displays superior capacities than the $LiVS_2$ data presented in Chapter 3, this is also especially evident at higher rates. Additionally, $LiV_{0.5}Ti_{0.5}S_2$ has a smaller polarisation, change of particle size on cycling and crucially operates at a more useful voltage. $LiV_{0.5}Ti_{0.5}S_2$ is a true 1 volt anode as intercalation and deintercalation occur under 1 volt, this is not the case for $LiVS_2$.

$LiV_{0.5}Ti_{0.5}S_2$ displays a superior capacity to $Li_4Ti_5O_{12}$ (~175 $mAhg^{-1}$) with good capacity retention[10]. It also operates at ~ 0.5 V less, which results in a large potential when used in a full cell. Intercalation and deintercalation in $LiV_{0.5}Ti_{0.5}S_2$ takes place at a higher voltage than in graphite and subsequently $LiV_{0.5}Ti_{0.5}S_2$ has a smaller irreversible capacity loss on the first cycle and no safety concerns with lithium dendrite formation.

The density of $LiV_{0.5}Ti_{0.5}S_2$ is 3.34 gcm^{-1} and the gravimetric capacity of 220 $mAhg^{-1}$ is equivalent to a volumetric capacity of 734 $mAhcm^{-3}$. This is higher than graphite which has a

reversible volumetric capacity of 600 – 700 $mAhcm^{-3}$ depending on the density of the graphite used[4]. The higher density also leads to considerably better volumetric density than organic systems like $Li_2C_6H_4O_4$[11,12]. Volumetric energy density is an important parameter when considering anode materials for use in full lithium-ion "rocking-chair" batteries.

While $LiV_{0.5}Ti_{0.5}S_2$ cannot produce the very high capacities of silicon or some conversion reactions it operates by a simple well understood intercalation mechanism. $LiV_{0.5}Ti_{0.5}S_2$ has a very small polarisation, displays little structural change on cycling and is highly reversible with only a 1.5% increase in the **c** direction upon lithium intercalation.

Sulphides are not exotic materials and have been used in a lot of applications ranging from pigments[13] to solar cells[14]. Sulphur is cheap and wildly available, indeed one of the benefits of the Li-sulphur battery is the low cost of sulphur. Titanium is also relatively inexpensive as seen by the commercialisation of $Li_4Ti_5O_{12}$. Although the sulphides here are synthesized in sealed tubes for convenience in the lab, this is not ubiquitous for sulphides and other methods can be used[15,16]. While $LiV_{0.5}Ti_{0.5}S_2$ is air-sensitive the pristine material can survive short exposure (several minute) to air with no change in X-ray diffraction patterns or electrochemical performance. As has been seen with $LiFePO_4$, air-sensitivity does not necessarily mean a material cannot be commercialised.

$LiV_{0.5}Ti_{0.5}S_2$ has been shown to be a promising anode material but its performance in a full cell is yet to be demonstrated. Chapter 6 will investigate the use of $LiV_{0.5}Ti_{0.5}S_2$ in full cells with a standard $LiCoO_2$ cathode and with the high voltage lithium-rich, manganese-rich mixed metal oxide cathodes that are studied in Chapter 5.

4.7.3 Future work

Future work on optimising the electrochemical performance should focus on electrode fabrication, to reduce the amount of carbon additive required, and use of alternative electrolytes and electrolyte additives. LP 30 has been optimised as an electrolyte for graphite and there may well be electrolytes that are better suited for use with sulphides. Some brief work with the addition of vinylene carbonate (VC) and fluoroethylene carbonate FEC has proved unsuccessful but there is still significant scope for further research. If successful this could reduce the irreversible capacity loss on the first cycle and increase capacity retention.

As mentioned above ball milling should be used to find the optimum particle size of the material and ICP should be carried out to confirm the elemental composition. Additionally, electrical conductivity measurements would be useful to help determine the amount of carbon additive necessary for satisfactory electrochemical performance.

4.8 References

1 Kim, Y., Park, K. S., Song, S. H., Han, J. T. & Goodenough, J. B. *J. Electrochem. Soc.* **156**, A703-A708 (2009).
2 Kim, Y. & Goodenough, J. B. *Electrochem. Solid State Lett.* **12**, A73-A75 (2009).
3 Yang, G. L., Kim, Y. & Goodenough, J. B. *J. Mater. Chem.* **21**, 10160-10164 (2011).
4 Sivakkumar, S. R., Nerkar, J. Y. & Pandolfo, A. G. *Electrochim. Acta* **55**, 3330-3335 (2010).
5 Li, D. & Zhou, H. S. *Mater. Today* **17**, 451-463 (2014).
6 Harks, P., Mulder, F. M. & Notten, P. H. L. *J. Power Sources* **288**, 92-105 (2015).
7 Malik, R., Zhou, F. & Ceder, G. *Nat. Mater.* **10**, 587-590 (2011).
8 Brutti, S., Gentili, V., Menard, H., Scrosati, B. & Bruce, P. G. *Adv. Energy Mater.* **2**, 322-327 (2012).
9 Gupta, A., Mullins, C. B. & Goodenough, J. B. *Electrochim. Acta* **78**, 430-433 (2012).
10 Ferg, E., Gummow, R. J., Dekock, A. & Thackeray, M. M. *J. Electrochem. Soc.* **141**, L147-L150 (1994).
11 Armand, M. *et al. Nat. Mater.* **8**, 120-125 (2009).
12 Kaduk, J. A. *Acta Crystallogr. Sect. B-Struct. Sci.* **56**, 474-485 (2000).
13 Anglos, D. *et al. Appl. Spectrosc.* **50**, 1331-1334 (1996).
14 Guo, Q. *et al. J. Am. Chem. Soc.* **132**, 17384-17386 (2010).
15 Murphy, D. W., Cros, C., Disalvo, F. J. & Waszczak, J. V. *Inorg. Chem.* **16**, 3027-3031 (1977).
16 Vanlaar, B. & Ijdo, D. J. W. *J. Solid State Chem.* **3**, 590-& (1971).

Chapter 5: Investigations in to Lithium-Rich Mixed Metal Oxides as Cathode Materials

5.1 Introduction

It was demonstrated in the previous chapter that $LiV_{0.5}Ti_{0.5}S_2$ shows promise as an anode material for lithium ion batteries, in this chapter attention is turned to the positive electrode. The overview of cathode materials in Chapter 1 established that the lithium-rich layered mixed metal oxides are a group of materials of significant interest. These materials can produce high capacities (> 200 $mAhg^{-1}$) and do so at high voltages (up to 4.8 V)[1]. However, they have issues with both capacity fade, especially at high rates, and voltage fade, with the majority of the capacity accessed below 4 V on extended cycling[2].

It has been demonstrated previously that the non Li-rich mixed metal oxides $Li(Ni_{0.5}Mn_{1.5})O_4$[3] and $LiNi_{1/3}Mn_{1/3}Co_{1/3}O_2$[4] can be synthesised using a one-pot resorcinol-formaldehyde gel (RF-gel) synthesis. Materials previously synthesised using this method have displayed excellent electrochemistry and as a result, the same procedure was investigated for use with lithium rich materials. This chapter will outline the RF-gel synthesis and electrochemistry of $0.5Li_2MnO_3{:}0.5LiNi_{0.5}Mn_{0.5}O_2$ (LMR-NMO) and $0.6Li_2MnO_3{:}0.4Li(Ni_{1/3}Mn_{1/3}Co_{1/3})O_2$ (LMR-NMCO), two of the best performing Li-rich cathode materials for lithium-ion batteries.

Neutron diffraction is an excellent way of monitoring the changes in a battery material on extended cycling because the neutron scattering length of an element is not dependent on number of electrons present, therefore elements with small atomic masses, such as lithium, can be detected. Neutron diffraction data after the first 50 cycles of both LMR-NMO and LMR-NMCO were collected in order to gain a better understanding of the structural changes these materials undergo on extended cycling. The neutron diffraction work was carried out in collaboration with Dr A.R. Armstrong at the University of St Andrews.

5.2 Synthesis

Both $0.5Li_2MnO_3{:}0.5LiNi_{0.5}Mn_{0.5}O_2$ and $0.6Li_2MnO_3{:}0.4Li(Ni_{1/3}Mn_{1/3}Co_{1/3})O_2$ were synthesised using the RF-gel method described in Section 2.12.

Typically 0.025 moles of product was prepared in each synthesis, which resulted in approximately 2.2 g of material. Appropriate stoichiometric ratios of metal acetates were dissolved in distilled water. In a separate beaker resorcinol (0.1 mol) and lithium carbonate (0.25 g) were dissolved in a formaldehyde (0.15 mol) - water solution (21.17 ml). When the solids in both beakers were dissolved the contents were combined and stirred at 60 ^oC until a thick slurry/gel was formed, this was then dried overnight at 90 ^oC to remove any residual formaldehyde. The gel was subsequently calcined at 200 ^oC for 2 – 3 hours, to burn off the organic framework. At the end of calcination the gel was reduced to a brown/black powder. The final heating step typically consisted of heating at a rate of 2 ^oC per minute to 800 ^oC and holding that temperature for 6 hours. The furnace was than cooled at a rate of 10 ^oC per minute to room temperature and the product was removed.

5.3 Powder X-ray Diffraction (PXRD)

Powder X-ray diffraction was carried out to confirm that the materials were phase pure and of the correct general structure. As discussed in Section 2.2.1 X-ray diffraction measurements were conducted using an instrument with an iron source to overcome problems with fluorescence seen when using a traditional copper source. However, the iron source is less intense than copper, this results in a reduction in peak intensity in the collected X-ray diffraction patterns. Figure 5.1 shows the Powder X-ray diffraction patterns of LMR-NMO and LMR-NMCO synthesised using the RF-gel method and data from the literature.

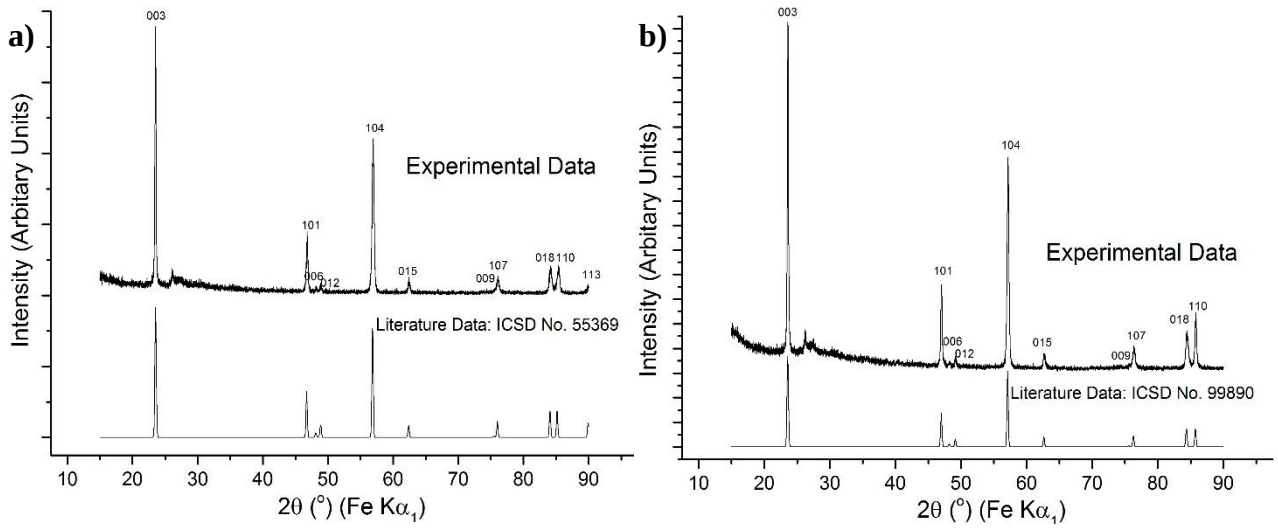

Figure 5.1: Powder X-ray diffraction patterns of a)$0.5Li_2MnO_3$:$0.5LiNi_{0.5}Mn_{0.5}O_2$ and b) $0.6Li_2MnO_3$:$0.4Li(Ni_{1/3}Mn_{1/3}Co_{1/3})O_2$. Both experimental and literature patterns are shown.

The experimental data for both materials correspond well to the literature data, with the synthesised material appearing to adopt the α-$NaFeO_2$ structure previously reported[5]. Li_2MnO_3 can be described in the $LiMO_2$ notation where $M^{3+} = Li^+_{1/3}Mn^{4+}_{2/3}$. The alternating arrangement of Li^+ and Mn^{4+} in the metal layer leads to the appearance of the superlattice peaks at ~ 27° [1]. While the presence of such peaks is found in lithium, manganese rich materials regardless of synthetic route, they are particularly strong when the RF-gel synthesis is used, indicating the material is very well ordered.

5.4 Scanning Electron Microscopy (SEM)

Scanning electron microscopy (SEM) was carried out on LMR-NMO and LMR-NMCO to gain information on the morphology of the materials produced by the RF-gel synthesis. Images of both materials at a magnification of 15,000 can be seen in Figure 5.2. The particle size of the two materials is approximately the same. There is a distribution of particle size from ~ 100 nm to ~ 1 µm, with most particles being 300 – 700 nm.

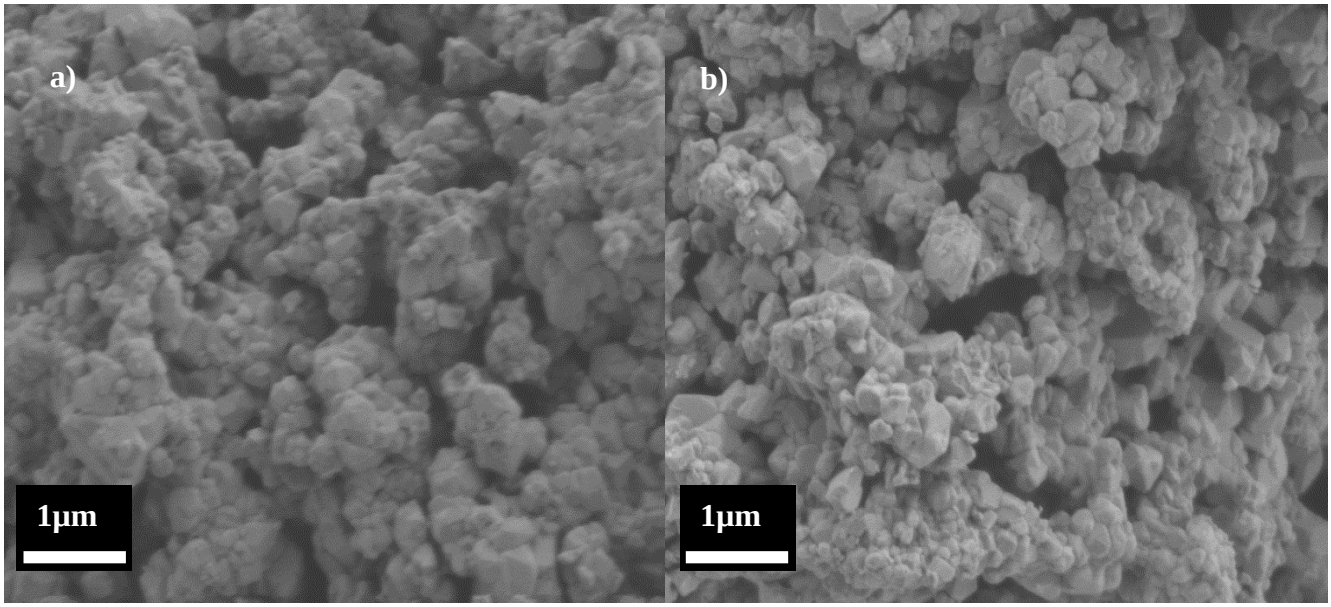

Figure 5.2: SEM images a) LMR-NMO and b) LMR-NMCO

5.5 Electrochemical Performance

This section will discuss the electrochemistry of the RF-gel synthesised lithium-rich, manganese-rich cathode materials. The first part will deal with LMR-NMO, while the second will be concerned with LMR-NMCO and also discuss the differences and similarities between the two materials. Electrochemical measurements were performed in coin cells as described in Section 2.5. All cells in this section were constructed with cast electrodes, using the ratio 76 : 12 : 12 by weight of active material : Super S carbon conductive additive : Kynar 2801 Binder. LP 30 (1 M $LiPF_6$ in 1 : 1 v/v EC : DMC) was the electrolyte used for all measurements.

5.5.1.1 Ni/Mn

Figure 5.3 below shows the load curves of the 1st, 2nd, 5th and 10th cycles of LMR-NMO at the rates of 15 mA g^{-1} and 150 mA g^{-1}. The cells were cycled between 4.8 V and 2.0 V.

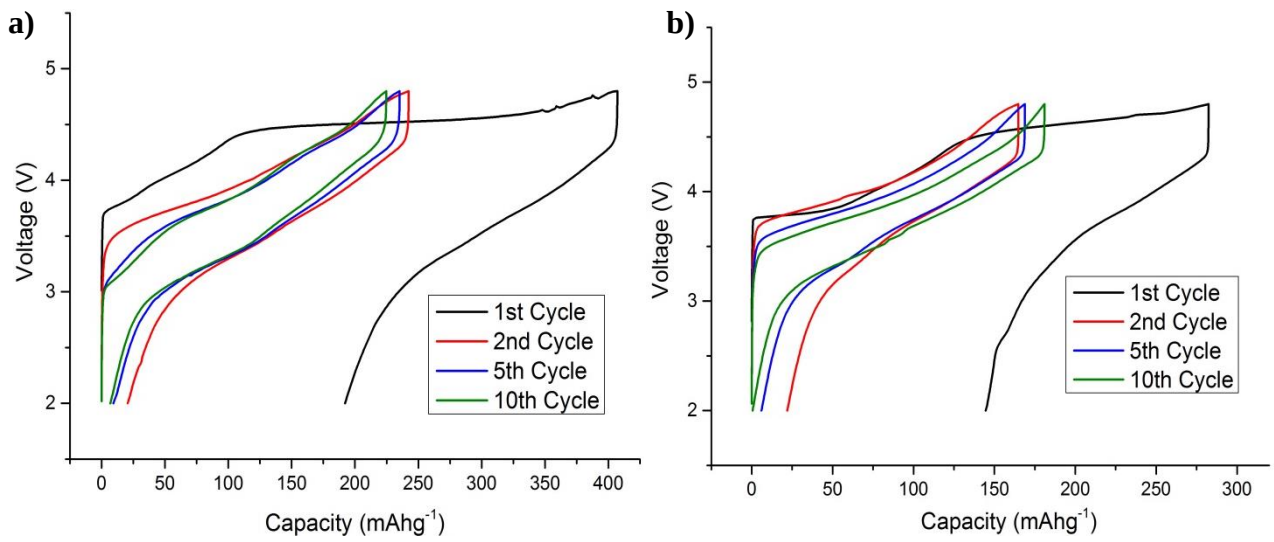

Figure 5.3: Load curves of the 1st, 2nd, 5th and 10th cycle of LMR-NMO at a) 15 mAg^{-1} and b) 150 mAg^{-1}.

The most striking observation from the above load curves is the difference between the first cycle and subsequent cycles. The first charge can be divided into two distinct regions. The first, between ~ 3.7 V and ~ 4.4 V, may be further sub-divided into two regions, this is more evident at the higher rate. The capacity in this region can be attributed to lithium deintercalation from the LMR-NMO[5]. Above 4.4 V the Li_2MnO_3 component of the material is activated and this is responsible for the high voltage plateau observed at ~ 4.5 V. It is generally thought that during this activation process lithium and oxygen are removed from the Li_2MnO_3 component[2]. The mechanism of this removal process and the identity of the resultant material have been subject to much research, however, neither are currently well understood[2]. One explanation is that after the activation process the electrochemically inactive Li_2MnO_3 is transformed to the electrochemically active MnO_2[1]. The introduction of this second electrochemically active species explains the high capacities obtained by these materials. On the 1st discharge only one pseudo-plateau is observed and is consistent with the oxygen removal process being irreversible. Unsurprisingly, this leads to a large irreversible capacity loss on the first cycle. As discussed in Section 1.4.2.4 there is also increasing evidence that an oxygen redox process may be responsible for the high voltage process. The irreversible capacity loss is high at both rates

but is higher at slow rates, indicating that the oxygen removal process may be partly kinetically determined. On subsequent cycles there is a significant decrease in polarisation compared to the 1st cycle. At a rate of 150 mAg^{-1}, after 10 cycles the polarisation is only ~0.2 V; however, the electrochemical process occurs over a large voltage range. Interestingly, the voltage of the electrochemical process appears to be rate dependent, this will be discussed in greater detail below. It is also clear from the load curves that there is 'voltage fade' on cycling especially at the higher rate. This can be seen by the reduction in the potential of both the charge and discharge curves in Figure 5.3b, this is a common issue with these materials[6].

Considering further the performance of RF-gel synthesised LMR-NMO the variation of capacity with cycle number for the two rates discussed above are shown in Figure 5.4.

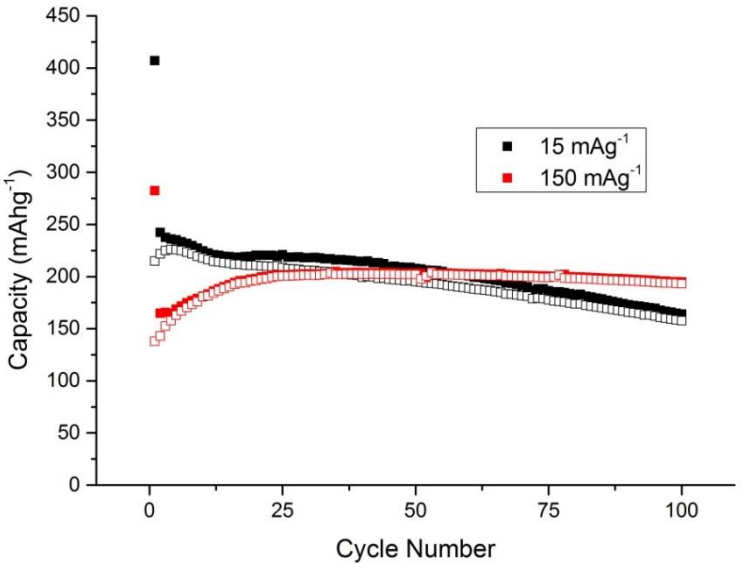

Figure 5.4: Variation of capacity with cycle number for LMR-NMO at various rates. Cells were cycled between 4.8 V and 2.0 V. Closed squares correspond to charge and open squares to discharge.

As shown above the cell cycled at the slow rate of 15 mAg^{-1} initially displayed a superior capacity, however, this was subject to continual capacity fade. In contrast, at a rate of 150 mAg^{-1}, only modest charge/discharge capacities are initially displayed but this increases considerably over ~ 25 cycles to a maximum of over 200 $mAhg^{-1}$ and this capacity is maintained with very little capacity fade for 75 cycles. Increasing capacity over the first few cycles at high rates was

also observed for the anode materials discussed in Chapter 3 and 4. For the anode materials this was due to capacity being lost at low voltages due to the reduction in the intercalation potential, this is not the case for the LMR-NMO materials. Here it appears to be due to the gradual electrochemical activation of the whole electrode as can be seen in the differential capacity plots observed below. The presence of these 'break-in cycles' is often observed for these materials and appears to be dependent on synthesis route[7]. The reversible capacity of 200 $mAhg^{-1}$ observed for RF-gel synthesised LMR-NMO at rate of 150 mAg^{-1} is higher than seen in the vast majority of previously reported materials of this type[1], with only a highly complex nanoparticle synthesis route showing superior capacities[8].

Given the pseudo-plateau nature of the electrochemical process it is difficult to ascertain from the load curves above how many "plateaus" are actually present. Plateaux on the load curves presented in Figure 5.3 correspond to peaks in the differential capacity plots below. To gain a better understanding of how the electrochemistry changes on cycling, differential capacity plots of the 2nd, 10th, 25th, 50th, 75th and 100th cycles were constructed for both rates. As seen in the load curves the 1st cycle is very different from the others and has been omitted.

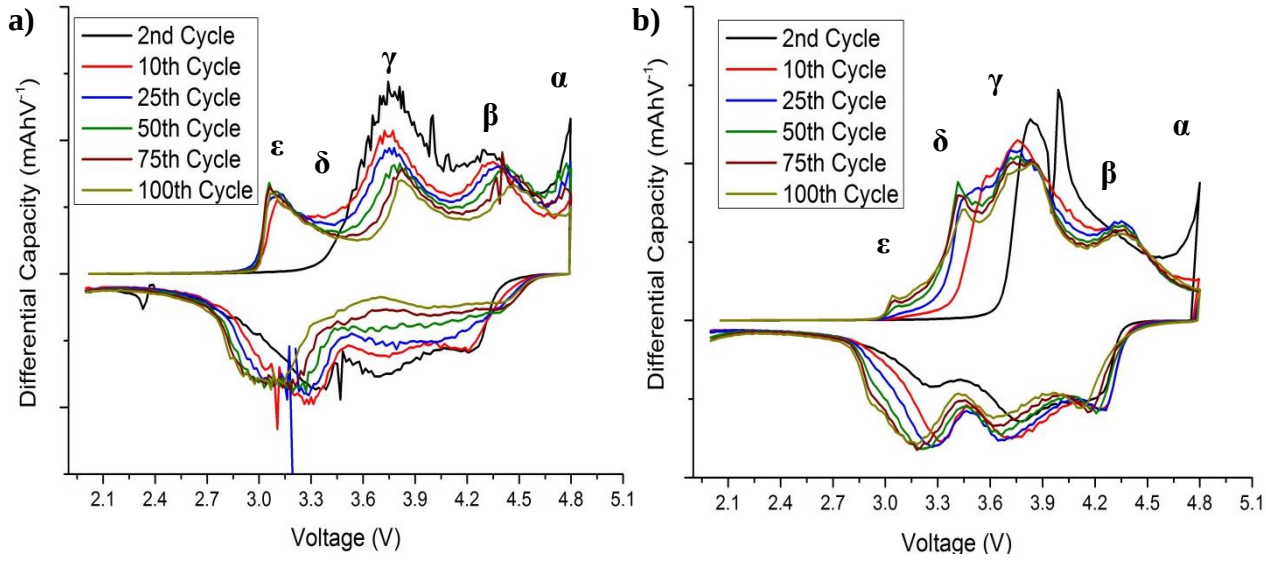

Figure 5.5: Differential capacity plots of the 2nd, 10th, 25th, 50th, 75th and 100th cycles for LMR-NMO at a) 15 mAg^{-1} and b) 150 mAg^{-1}.

The differential capacity plots reveal there are multiple electrochemical processes occurring at both rates. Differential capacity plots are very sensitive to very small changes in the load curve of a material and therefore 'spikes' appear, these will not be discussed and analysis will be confined to the more significant features. Discussion will focus mainly on the charge processes, and voltages quoted refer to this, as this is where it is believed the important changes take place. Additionally, it is worth noting that with so many processes occurring it is difficult to assign each peak to a specific electrochemical process with certainty.

The peaks labelled α, β, γ, δ and ε will be discussed in turn beginning with the high voltage process and moving down. The process labelled α at 4.7 - 4.8 V is due to a small continuation of the process seen on the first charge and is irreversible. At the high rate it is only a factor on the second cycle while at the slow rate it continues to a small extent on extended cycling. This explains the fairly large irreversible capacity losses seen for the second cycle load curves in Figure 5.3.

The peaks labelled β and γ are present at both high and low rates and are due to the reversible nickel redox couples[9]. On the second cycle at 150 mAg^{-1} the two peaks in this region are much closer together at 3.82 V and 3.99 V, these correspond to the couples Ni^{2+}/Ni^{3+} and Ni^{3+}/Ni^{4+} respectively[10]. These peaks are also present on the first charge but it is unusual for them to be observed on the second charge. However, it important to note that all the differential capacity plot measurements in the literature are carried out at slow rates (typically ≤ 30 mAg^{-1}) and are therefore under conditions of gradual capacity decline. The presence of the peaks at 3.82 V and 3.99 V indicate that at fast rates LMR-NMO still shows characteristics of the pristine material on the second cycle. On subsequent cycles the Ni^{2+}/Ni^{3+} redox couple migrates to ~ 3.75 V and the Ni^{3+}/Ni^{4+} redox couple to ~ 4.35 V, both of these values are in good agreement with literature values. At the slow rate the intensity of both β and γ decrease on cycling, this is unsurprising as there is gradual capacity fade over the 100 cycles.

The peaks labelled δ and ε are probably due to manganese redox processes. It initially appears that the peak labelled δ is not found at 15 mAg^{-1} and the peak labelled ε is very small at 150 mAg^{-1}, however, this is misleading. It was observed in Chapters 3 and 4 that the potential at which lithium intercalation occurred in the sulphide anode materials was dependent on rate of charge, it is also a factor for cathode materials. The Mn^{3+}/Mn^{4+} redox couple is often reported to be at ~ 3.2 V in these materials[9], however, as discussed above these measurements were carried out at slow rates. It is possible that the Mn^{3+}/Mn^{4+} redox couple moves to a higher potential at higher rates and that δ in Figure 5.5b and ε in Figure 5.5a both correspond to this redox couple. The small ε peak that grows on extended cycling at the fast rate of 150 mAg^{-1} could correspond to the growth of a spinel phase, as has been reported for these materials[11,12]. The activation of the δ and ε peaks is responsible for the voltage fade observed in the load curves in Figure 5.3b. Figure 5.5b shows that the voltage of deintercalation (charge) ceases to show any significant fade after 25 cycles but on intercalation (discharge) it continues to 50 cycles. It is also interesting to note that while the peaks corresponding to the nickel redox couples reduce in size on cycling at 15 mAg^{-1} the peak corresponding to Mn^{3+}/Mn^{4+} does not, indicating the growth of a manganese spinel phase.

To summarise; at slow rates the high voltage nickel redox process fades quite considerably upon cycling while the low voltage manganese redox process is fairly steady. The reduction in the nickel contribution results in the capacity loss seen in Figure 5.4 At the high rate of 150 mAg^{-1} there is much less reduction in the magnitude of the nickel redox peaks and there is a marked increase in the manganese process. The activation of the manganese process over the first 50 cycles is responsible for the increase in capacity seen in the cycling data above. The activation of the manganese process also appears to be responsible for the voltage fade seen in these materials. As the manganese processes take fewer cycles to reach their maximum at slow rates it implies that the manganese process is kinetically limited. The greater capacity fade seen

at slower rates was also seen in the previous chapters on anode materials. In those chapters it was due to the electrode spending more time at low rates and therefore being subject to more SEI layer formation. The reason for the capacity loss here is most likely very similar. 4.8 V is very close to the upper limit of the stability of most electrolytes, including LP 30, therefore as the slow rate electrode spends more time at high voltages there will be more electrolyte decomposition, this leads to greater capacity loss.

5.5.1.2 Ni/Mn/Co

Turning attention to the cobalt-containing $0.6Li_2MnO_3{:}0.4Li(Ni_{1/3}Mn_{1/3}Co_{1/3})O_2$. Figure 5.6 below displays the load curves of the 1st, 2nd, 5th and 10th cycles of LMR-NMCO at the rates of 15 mAg^{-1} and 150 mAg^{-1}. It was observed in the LMR-NMO system that at low rates virtually all of the capacity, and Li_2MnO_3 activation, was found to be below 4.6 V. Therefore the cell at 15 mAg^{-1} was cycled between 4.6 V and 2.0 V and the cell at 150 mAg^{-1} was cycled between 4.8 V and 2.0 V.

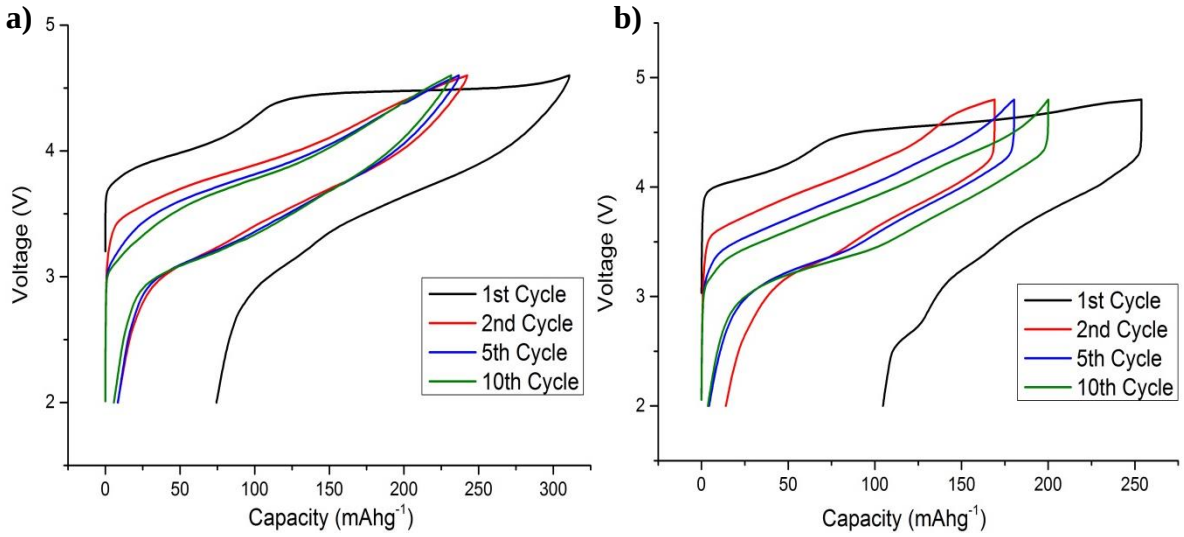

Figure 5.6: Load curves of the 1st, 2nd, 5th and 10th cycle of LMR-NMCO at a) 15 mAg^{-1} and b)150 mAg^{-1}.

The general appearance of these load curves are very similar to the LMR-NMO load curves seen above, however, there are several differences. The LMR-NMCO cells display a reduced

first cycle irreversible capacity loss compared to LMR-NMO. This is most obviously seen at 15 mAg^{-1} as the irreversible capacity loss is reduced from nearly 200 $mAhg^{-1}$ to ~ 75 $mAhg^{-1}$, in part due to the reduction of the upper voltage cut-off. At 150 mAg^{-1} the irreversible capacity loss is reduced from nearly 150 $mAhg^{-1}$ to ~ 100 $mAhg^{-1}$, suggesting that the presence of cobalt suppresses the irreversible capacity loss to some extent. The other major difference is on the first charge, initial lithium extraction begins at a higher voltage for LMR-NMCO compared to LMR-NMO. This is especially evident at 150 mAg^{-1} where it rises from 3.75 V to 4.0V. This is due to the Co^{3+}/Co^{4+} redox couple raising the potential of lithium deintercalation. The rest of the major observations from Figure 5.5: the different stages of the 1st charge load curve, the reduced polarisation on cycling and the voltage fade at 150 mAg^{-1} are the same as seen for LMR-NMO.

Figure 5.7 displays the rate performance of RF-gel synthesised LMR-NMCO at 15 mAg^{-1} and 150 mAg^{-1}.

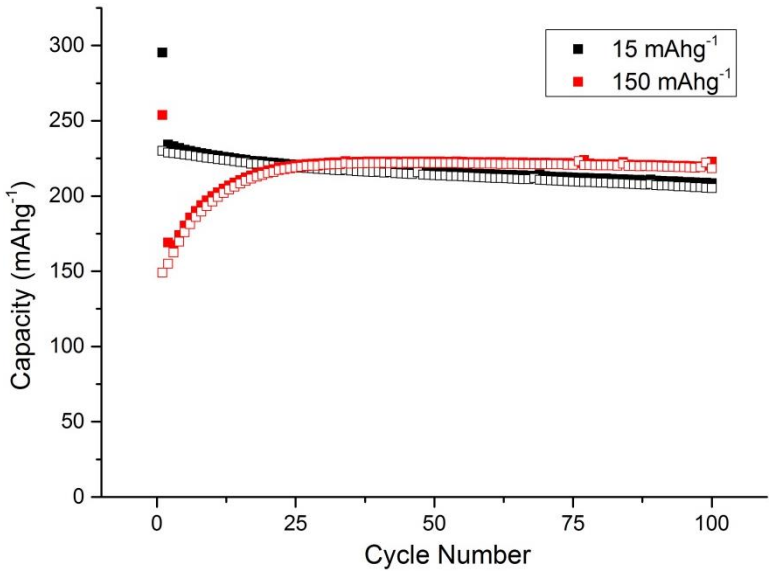

Figure 5.7: Variation of capacity with cycle number for LMR-NMCO at various rates. Closed squares correspond to charge and open squares to discharge.

LMR-NMCO shows superior electrochemical performance compared to LMR-NMO, however, the same general trends are displayed. This is consistent with what has been previously reported

– increasing the amount of cobalt increases the capacity[13]. At the slow rate of 15 $mAhg^{-1}$ the initial capacity is 225 $mAhg^{-1}$ virtually the same as that observed for LMR-MNO, but the capacity fade is considerably less for LMR-NMCO, this may in part be due to the change in voltage cut off. The observed capacity is roughly similar to literature values for LMR-NMCO operating at slow rates. At 150 $mAhg^{-1}$ there is a steady increase in capacity until a capacity of ~ 220 $mAhg^{-1}$ is achieved at around cycle 25. There is then excellent capacity retention up to 100 cycles. The capacity of 220 $mAhg^{-1}$ is 20 $mAhg^{-1}$ higher than the capacity observed for LMR-NMO and higher than the capacity observed in the vast majority of LMR-NMCO synthesised by other routes[14].

As the rate performance trends of LMR-NMCO are very similar to LMR-NMO it might be expected that the same electrochemical processes are present. Differential capacity plots of the 2nd, 10th, 25th, 50th, 75th and 100th cycles were plotted for 15 mAg^{-1} and 150 mAg^{-1} to confirm if this was the case. Like LMR-NMO the 1st cycle is omitted as it is dominated by a very large peak at ~ 4.6.

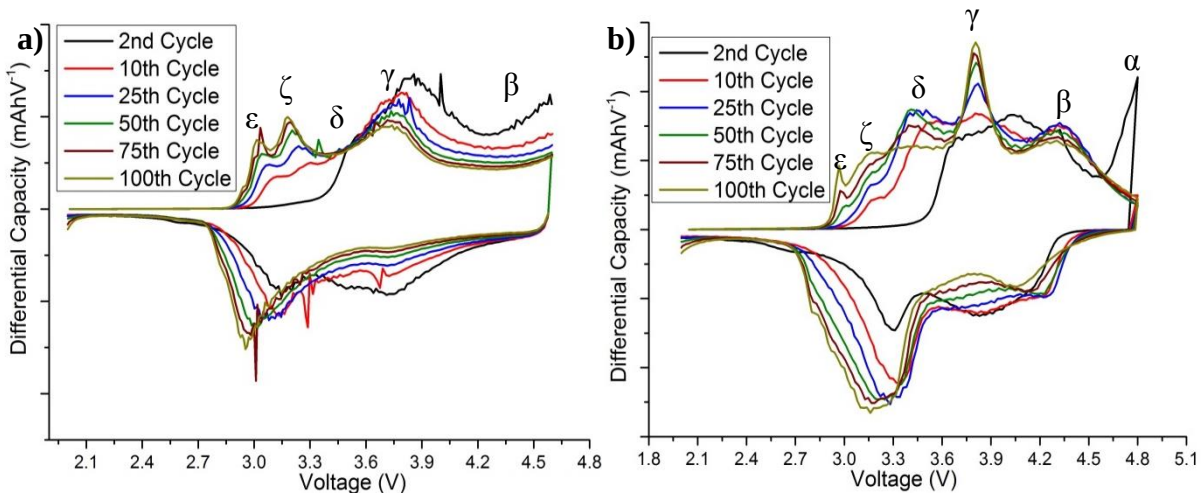

Figure 5.8: Differential capacity plots of the 2nd, 10th, 25th, 50th, 75th and 100th cycles for LMR-NMCO at a) 15 mAg^{-1} and b) 150 mAg^{-1}.

Like the differential capacity plots for LMR-NMO seen in Figure 5.5 it is useful to go through the peaks one at a time. Many of the peaks are the same as seen previously. Peak α corresponds

to a continuation of the irreversible oxygen and lithium loss process seen on the first cycle, due to the lower voltage cut off this is missing from Figure 5.8a. Peak β is due to the Ni^{3+}/Ni^{4+} redox couple, at the slow rate this is very broad. Peak γ corresponds to the Ni^{3+}/Ni^{4+} redox couple and also the Co^{3+}/Co^{4+} couple[9]. The large broad peak in the 2nd cycle differential capacity plot at 150 mAg^{-1} is due to the overlapping of the nickel and cobalt redox couples. As with LMR-NMO peak δ is probably due to the Mn^{3+}/Mn^{4+} redox couple shifted to a higher voltage by the higher rate.

It is between 3.0 V and 3.3 V that the differential capacity plots of LMR-NMCO are most different compared to LMR-NMO. It is probable that the peak ζ that does not appear in either of the LMR-NMO load curves is due to cobalt. The peak ε is again probably due to the growth of a spinel like phase. Possible evidence for this is that for the data collected at 150 mAg^{-1} the Mn^{3+}/Mn^{4+} redox couple, peak δ, decreases as the manganese spinel peak, ε, increases, implying manganese rich portions of the material are transforming from a layered structure to a spinel structure, this has previously been seen in other LMR-NMCO materials[15].

The rate capabilities of LMR-NMCO are presented in a "waterfall plot" in Figure 5.9. The electrode material was cycled for 1 cycle at 15 mAg^{-1} and then 10 cycles at 150 mAg^{-1}, 300 mAg^{-1}, 600 mAg^{-1}, 900 mAg^{-1} and 1200 mAg^{-1}.

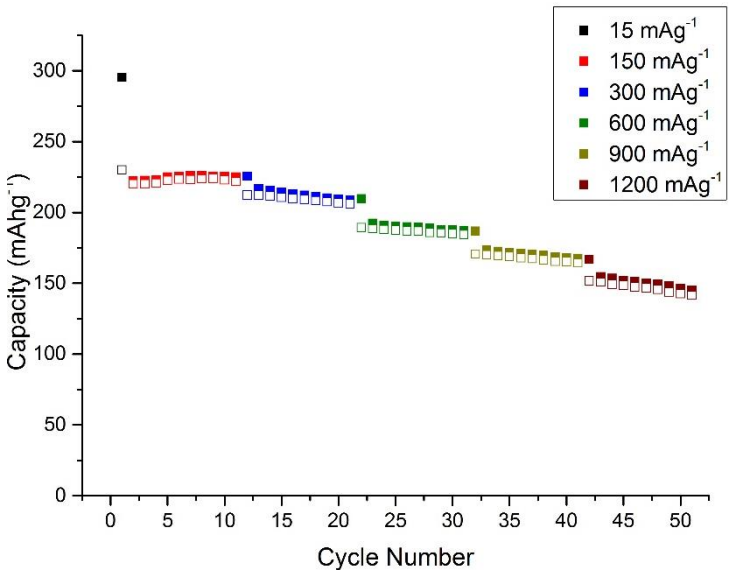

Figure 5.9: Variation of capacity with cycle number for LMR-NMCO at various rates of charge/discharge. Closed squares correspond to intercalation and open squares to deintercalation.

The rate capability of LMR-NMCO is clearly very good with a reduction in capacity from 220 $mAhg^{-1}$ at 150 mAg^{-1} to 150 $mAhg^{-1}$ at 1200 mAg^{-1}, this compares very favourably to previously reported materials[16]. Including 1 cycle at 15 mAg^{-1} eliminates the 'break-in cycles' seen in the 150 $mAhg^{-1}$ rate data seen in Figure 5.7. Capacity fade at higher rates is only slightly more significant than at 150 mAg^{-1}.

One of the issues seen in the LMR-NMCO data above is the presence of 'break-in cycles' at high rates. It is obviously desirable for a material to show its maximum capacity immediately and not after 25 cycles. As seen in Figure 5.9 one way of circumventing this issue it to begin with one cycle at a low rate before cycling at higher rates. It is also important to note that while the RF-gel synthesis has the benefits of being a one pot synthesis it has a great many variables that can be optimised. One of these variables is the amount of Li_2CO_3 catalyst used in the synthesis. In all the previous data for both LMR-NMO and LMR-NMCO 0.25 g of Li_2CO_3 is used, Figure 5.10 below shows the effect on capacity vs cycle number when this amount is reduced.

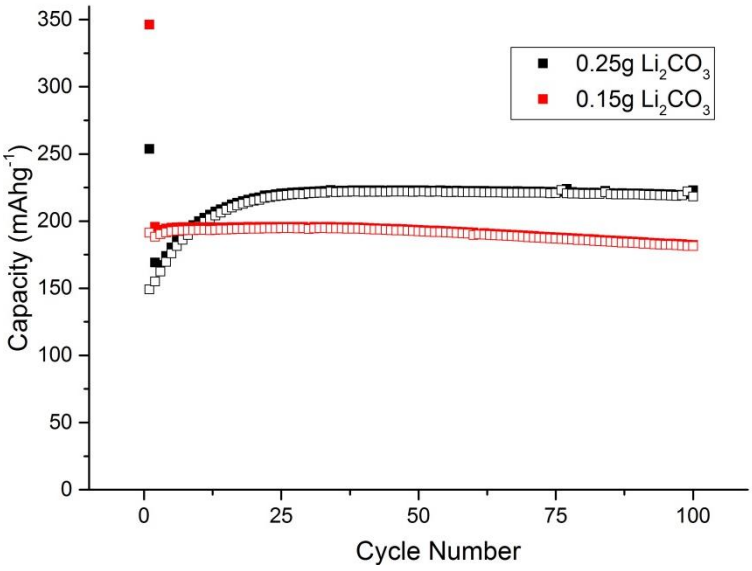

Figure 5.10: Variation of capacity with cycle number for LMR-NMCO at 150 mAg^{-1} using various amounts of Li_2CO_3. Closed squares correspond to charge and open squares to discharge.

Figure 5.10 shows that the amount of Li_2CO_3 has a significant effect on the electrochemical performance. Lowering the amount of Li_2CO_3 eliminates break-in cycles but also reduces the overall capacity and increases capacity fade. It has been shown previously that the amount of catalyst can control the cluster size of the agglomerated resorcinol rings[17], however SEM images and differential capacity plots show no variation with the amount of Li_2CO_3, implying that the differences in Figure 5.10 are not due to a change in morphology but due to the amount of lithium in the system. Unlike most synthesis methods of lithium-manganese-rich materials the RF-gel synthesis does not use an excess of lithium in the starting materials - a stoichiometric amount of lithium acetate is used. However, the excess Li_2CO_3 seems to play this role, as well as speeding up the gelation process. It may be possible by optimising the amounts of Li_2CO_3 catalyst and excess lithium acetate to synthesise a material with no break-in cycles that displays a reversible capacity of over 220 $mAhg^{-1}$ at 150 mAg^{-1}, this should be a focus of future work.

5.6 Neutron Diffraction

This section is concerned with the neutron diffraction of LMR-NMO and LMR-NMCO. Part of the reason for this neutron diffraction investigation is to take advantage of the fact that ^{58}Ni

and ^{60}Ni have very different neutron scattering lengths. By synthesising a ^{58}Ni and ^{60}Ni version of each composition this allowed for the two samples to be refined simultaneously to give more accurate atomic occupancies and positions. The neutron experiment is concerned with the change in structure of both LMR-NMO and LMR-NMCO on extended cycling. While the first cycle of these lithium rich materials has been extensively investigated there has been less work carried out on these materials after multiple cycles.

5.6.1 Synthesis and Electrode Preparation

To produce lithium rich materials that have isotopically pure nickel a slightly different synthetic procedure was required. Pure ^{58}Ni and ^{60}Ni were dissolved in nitric acid to form isotopically pure nickel nitrate. Attempts to dissolve the nickel metals in acetic acid did not result in pure phase metal acetates, possibly due to differences in the number of water ligands, thus nickel nitrate was then used instead and the rest of the synthesis was carried out as described previously. The X-ray data for the ^{58}Ni-nitrate containing LMR-NMO and LMR-NMCO are presented in Figure 5.11, the data for ^{60}Ni versions are not shown as they are identical.

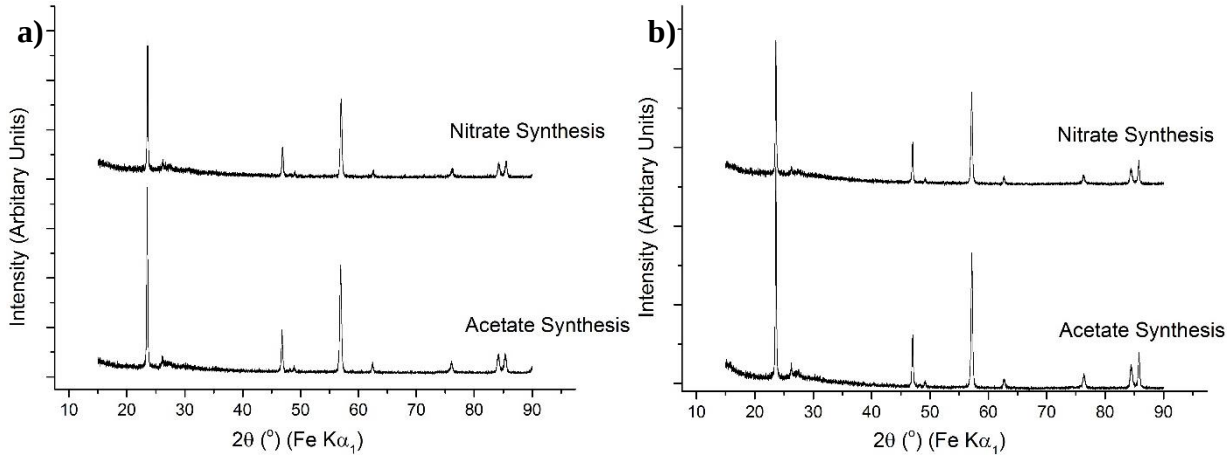

Figure 5.11: X-ray diffraction patterns comparing the acetate and nitrate synthesis for a) LMR-NMO and b) LMR-NMCO.

In order to produce the amount of material needed for neutron diffraction, pellet electrodes were used and cycled at a slow rate of 30 mAg^{-1}. Cells were cycled for various numbers of cycles,

these were: 1 cycle, 2 cycles, 5 cycles, and 50 cycles. The cycling data for both materials are presented in Figure 5.12. As the different isotopes of nickel have no effect on the electrochemistry only the ^{58}Ni data is presented here, like in the X-ray data above the ^{60}Ni is identical.

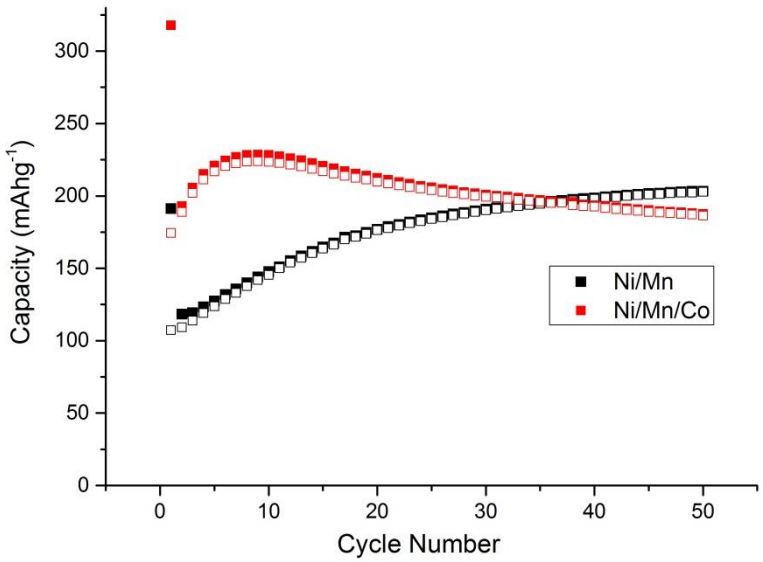

Figure 5.12: Variation of capacity with cycle number for LMR-NMO and LMR-NMCO pellets at 30 mAg^{-1}. Closed squares correspond to charge and open squares to discharge.

The materials display slightly different behaviour from the cast electrodes seen above. LMR-NMO shows a maximum capacity of ~ 200 mAhg^{-1} the same as for the cast material but it takes almost 50 cycles to achieve that. LMR-NMCO also achieves the same capacity as the cast electrodes, 220 mAhg^{-1}, but after only 8 cycles, and there is capacity fade after this. The behaviour of LMR-NMCO can be explained since the number of break-in cycles is between what is seen at 15 mAg^{-1} and 150 mAg^{-1} and the poor capacity retention is to be expected from thicker pellet electrodes compared to cast electrodes.

Differential capacity plots for both compositions synthesised using nickel nitrate are produced in Figure 5.13 below.

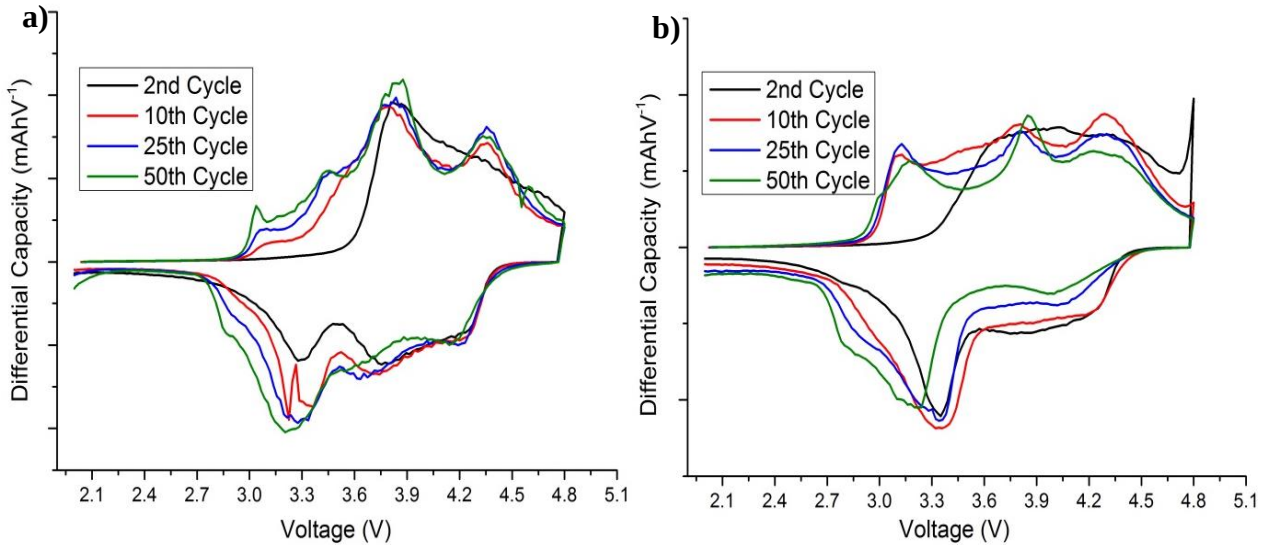

Figure 5.13: Differential capacity plots of the 2nd, 10th, 25th and 50th cycles for a) LMR-NMO and b) LMR-NMCO, synthesised using isotopically pure nickel nitrate and cycled at 30 mAg^{-1}.

While the two differential capacity plots look very different, the peaks present all correspond to those seen in Figures 5.5 and 5.8, a full discussion of these was covered above and will not be repeated here. However, it is interesting to note that the LMR-NMO plot in Figure 5.13 is very similar to the 150 mAg^{-1} plots seen above, while the LMR-NMCO plot is much closer to the 15 mAg^{-1} previously seen.

Neutron refinements and the relationship between the structure of the materials and the electrochemistry will be discussed below. All of the neutron diffraction data was obtained from isotopically pure nickel samples. The ^{58}Ni and ^{60}Ni versions of each sample were refined together as a joint refinement. This allowed for a greater amount of precision and enabled refinement of parameters that would not have been possible without the use of the isotopically pure nickel.

5.6.2 Neutron Diffraction of pristine materials

For both LMR-NMO and LMR-NMCO a monoclinic structure in the space group C2/m (Li_2MnO_3 structure) was used as the staring model and the model was refined against the data to give excellent fits in both cases. There was no evidence of any secondary phases in the

neutron diffraction data of either material, implying that the materials are solid solutions and are not made up of $LiMO_2$ and Li_2MnO_3 regions, this is consistent with previously published X-ray diffraction and STEM studies[18]. The tables, displaying the key refined parameters and goodness of fit parameters, and the difference plots of both materials can be found in Appendix B.

As expected, the materials have very similar structures. The most obvious difference is the reduction in the size of the unit cell in LMR-NMCO compared to LMR-NMO. This is presumably due to the smaller ionic radii of Co^{3+} compared to Ni^{2+}. Both materials show that lithium has a clear preference for Li site in Mn layers of Li_2MnO_3 this leads to the alternating arrangement of Li^+ and Mn^{4+} and subsequently the appearance of the superlattice peaks at ~ 27^o in the X-ray diffraction patterns above.

5.6.3 Structural changes on cycling

Full tables of refinement parameters and difference plots for all the data in this section can be found in Appendix B.

After one cycle there is a structural rearrangement from a monoclinic Li_2MnO_3 like structure to a trigonal $LiMO_2$ like structure. This is expected given the structural rearrangement that takes place at high voltages on the first charge coinciding with oxygen loss/oxygen redox. Both LMR-NMO and LMR-NMCO were found to be single trigonal phases with R-3m symmetry. Unlike the pristine samples, there is very little variation in lattice parameters between the two compositions. LMR-NMO has refined lattice parameters of **a** = 2.8638(1) **c** = 14.2718(13) (**c**/**a** = 4.9835), while LMR-NMCO displays refined lattice parameters of **a** = 2.8675(1) **c** = 14.254(1) (**c**/**a** = 4.971). Both compositions display a loss of lithium consistent with the reported oxygen loss/redox mechanisms proposed in the literature. The lithium content in LMR-NMO is reduced from 1.17 to 0.92, while for LMR-NMCO it is reduced from 1.2 to 0.97.

On the subsequent cycles the two materials display divergent behaviour. After the 2nd cycle the cobalt containing LMR-NMCO continues to display a single trigonal phase with very similar lattice parameters and atomic occupancies to the material after 1 cycle. However, LMR-NMO now consists of two phases. The first of these is the trigonal phase seen after 1 cycle, the second is also a trigonal phase, but one that contains a small amount of tetrahedral lithium in the transition metal layers. After 5 cycles both materials can be refined as pure phase trigonal phases containing tetrahedral lithium. The presence of this tetrahedral lithium forms local regions with a spinel-like atomic arrangement within the layered structure; this is sometimes referred to as a 'splayered' structure. As Co^{3+} has a high affinity to maintain a layered structure, due to its small size, it suppresses the formation of 'splayered' regions for several cycles and LMR-NMCO after the 2nd cycle is a pure phase. It should be noted that after 5 cycles both LMR-NMO and LMR-NMCO show a small amount of nickel on the octahedral lithium site. This is not uncommon for lithium nickel oxides as Li^{+} and Ni^{2+} have similar ionic radii and the amount of nickel migration seen here is very small with only ~ 1% Ni occupancy of the Li(1) site in LMR-NMO.

After 50 cycles both materials are clearly two phases, the first the 'splayered' structure seen after 5 cycles and the other a spinel phase. For LMR-NMO the spinel phase is approximately 13% of the sample, while for LMR-NMCO it is only 10%. The lower amount of spinel phase for the cobalt containing sample is consistent with the suppression of the splayered phase documented above and is due to the same reason. Only a small amount of spinel phase is observed for both compositions, thus showing the structural stability of the RF-gel synthesised materials.

Comparing the neutron data to the electrochemistry earlier in this chapter several observations can be made. The formation of splayered phase appears to take place at the same time as the activation of the manganese redox process at ~ 3.5 V. This indicates that the manganese requires

a small amount of tetrahedral lithium to become redox active. Further neutron experiments on different numbers of cycles will be required to confirm if the contribution from the manganese redox process (and hence the specific capacity of the material) is dependent on the amount of tetrahedral lithium. That only a small amount of spinel phase is observed, and it is not present on early cycling, indicates that the small peak at ~ 3.0 V (ε in Figures 5.5 and 5.8) is due to the spinel phase, as was hypothesised in the earlier sections. In 5.13b this is obscured by the larger manganese redox peak but the shoulder seen on the 50th cycle may be the spinel component.

5.7 Conclusions

The resorcinol-formaldehyde gel method has been successfully employed to synthesise $0.5Li_2MnO_3{:}0.5LiNi_{0.5}Mn_{0.5}O_2$ (LMR-NMO) and $0.6Li_2MnO_3{:}0.4Li(Ni_{1/3}Mn_{1/3}Co_{1/3})O_2$ (LMR-NMCO).

LMR-NMO shows an initial capacity of 220 mAhg^{-1} at 15 mAg^{-1}, but is subject to continual capacity fade. At 150 mAg^{-1} the initial capacity is low but after 25 cycles a capacity of over 200 mAhg^{-1} is displayed and this is maintained with no capacity fade for 75 cycles.

LMR-NMCO displays an initial capacity of 225 mAhg^{-1} at 15 mAg^{-1}, and is also subject to continual capacity fade but not at such a significant rate as LMR-NMO. At 150 mAg^{-1} the initial capacity is 140 mAhg^{-1} but after 30 cycles the capacity is 220 mAhg^{-1} and no capacity fade is observed for the next 70 cycles.

The specific capacities and capacity retention of both materials at 150 mAg^{-1} are excellent and better than virtually all previously reported materials of this type. The higher rate data for LMR-NMCO is also very promising with a capacity of 150 mAhg^{-1} produced at the very fast rate of 1200 mAg^{-1}. The amount of Li_2CO_3 in the RF-gel synthesis has been found to play a

significant role in the electrochemical performance of the materials. Reducing the amount of Li_2CO_3 reduced the overall capacity but reduces the number of 'break-in' cycles before the maximum capacity is achieved.

Neutron diffraction data show the formation of a splayered phase containing tetrahedral lithium after only a few cycles for both compositions. This coincides with the activation of the manganese redox process at ~ 3.5 V. After 50 cycles 10 – 15 % spinel phase is observed, the corresponding peak in the differential capacity plots is at ~ 3.0 V. Cobalt reduces the amount of splayered and spinel formation due to its affinity for the layered structure.

Both $0.5Li_2MnO_3{:}0.5LiNi_{0.5}Mn_{0.5}O_2$ (LMR-NMO) and $0.6Li_2MnO_3{:}0.4Li(Ni_{1/3}Mn_{1/3}Co_{1/3})O_2$ (LMR-NMCO) will be used as the cathode material in full lithium-ion cells with $LiV_{0.5}Ti_{0.5}S_2$ in the following chapter.

Future work will focus on optimisation of the synthetic procedure, especially in regards to the amount of lithium present in the system, and gaining a better understanding of the underlining electrochemical processes using a range of different techniques.

5.8 References

(1) Gu, R. M.; Yan, S. Y.; Sun, S.; Wang, C. Y.; Li, M.. *J. Solid State Electrochem.* **2015**, *19*, 1659-1669.
(2) Yan, J. H.; Liu, X. B.; Li, B. Y. *RSC Adv.* **2014**, *4*, 63268-63284.
(3) Shaju, K. M.; Bruce, P. G. *Dalton Trans.* **2008**, 5471-5475.
(4) Shaju, K. M.; Bruce, P. G. *Adv. Mater.* **2006**, *18*, 2330-+.
(5) Ying, P. Z.; Qiu, X. Y.; Zhang, Q. Q.; Zhuang, Q. C. *Ionics* **2015**, *21*, 657-665.
(6) Zhang, X. F.; Meng, X. B.; Elam, J. W.; Belharouak, I. *Solid State Ion.* **2014**, *268*, 231-235.
(7) Wei, X.; Zhang, S. C.; Du, Z. J.; Yang, P. H.; Wang, J.; Ren, Y. B. *Electrochim. Acta* **2013**, *107*, 549-554.
(8) Chen, L.; Su, Y. F.; Chen, S.; Li, N.; Bao, L. Y.; Li, W. K.; Wang, Z.; Wang, M.; Wu, F. *Adv. Mater.* **2014**, *26*, 6756-6760.
(9) Xiang, X. D.; Knight, J. C.; Li, W. S.; Manthiram, A. *J. Phys. Chem. C* **2014**, *118*, 21826-21833.
(10) Xiang, X. D.; Li, X. Q.; Li, W. S. *J. Power Sources* **2013**, *230*, 89-95.
(11) Croy, J. R.; Kim, D.; Balasubramanian, M.; Gallagher, K.; Kang, S. H.; Thackeray, M. M. *J. Electrochem. Soc.* **2012**, *159*, A781-A790.
(12) Yang, X. K.; Wang, D.; Yu, R. Z.; Bai, Y. S.; Shu, H. B.; Ge, L.; Guo, H. P.; Wei, Q. L.; Liu, L.; Wang, X. Y. *J. Mater. Chem. A* **2014**, *2*, 3899-3911.
(13) Li, J.; Camardese, J.; Shunmugasundaram, R.; Glazier, S.; Lu, Z. H.; Dahn, J. R. *Chem. Mat.* **2015**, *27*, 3366-3377.
(14) Kang, S. F.; Li, B.; Qin, H. F.; Fang, Y.; Li, X.; Wang, Y. G. *J. Solid State Electrochem.* **2015**, *19*, 525-531.
(15) Koga, H.; Croguennec, L.; Menetrier, M.; Mannessiez, P.; Weill, F.; Delmas, C. *J. Power Sources* **2013**, *236*, 250-258.
(16) Bian, X. F.; Fu, Q.; Qiu, C. G.; Bie, X. F.; Du, F.; Wang, Y. H.; Zhang, Y. Q.; Qiu, H. L.; Chen, G.; Wei, Y. J. *Mater. Chem. Phys.* **2015**, *156*, 69-75.
(17) Lu, X.; Arduini-Schuster, M. C.; Kuhn, J.; Nilsson, O.; Fricke, J.; Pekala, R. W. *Science.* **1992**, *255*, *971-972*.

(18) Jarvis, K. A.; Deng, Z. Q.; Allard, L. F.; Manthiram, A.; Ferreira, P. J. Atomic *Chem. Mat.* **2011**, *23*, 3614-3621.

Chapter 6: Full Cells using $LiV_{0.5}Ti_{0.5}S_2$

6.1 Introduction

Chapter 4 demonstrated that $LiV_{0.5}Ti_{0.5}S_2$ showed potential as an anode material and this chapter will combine $LiV_{0.5}Ti_{0.5}S_2$ with various cathode materials to make full lithium-ion 'rocking-chair' cells. Any potential anode material must prove that it is compatible with real cathode materials and not just lithium foil.[1,2] This is important because in lithium foil half-cells there is a massive excess of lithium used while in a practical Li-ion cell the amount of lithium is limited by the amount of cathode material. Therefore issues with irreversible capacity loss and capacity fade can be compounded in full-cells if lithium is removed from the reversible redox process.

The first section will describe the process of making and balancing full cells before moving on to show $LiV_{0.5}Ti_{0.5}S_2$ in a full cell with the most commonly used cathode material – $LiCoO_2$[3]. The following section will combine $LiV_{0.5}Ti_{0.5}S_2$ with the RF – gel synthesised $0.5Li_2MnO_3{:}0.5LiNi_{0.5}Mn_{0.5}O_2$ (LMR-NMO) and $0.6Li_2MnO_3{:}0.4Li(Ni_{1/3}Mn_{1/3}Co_{1/3})O_2$ (LMR-NMCO) materials described in Chapter 5.

It is important to state that the balancing of electrodes and optimisation of full cells is an intricate process that can make a substantial difference to the performance of a full cell. The main point of this chapter it to demonstrate that $LiV_{0.5}Ti_{0.5}S_2$ can be paired with various cathode materials and not the optimisation of these cells. Therefore this work should be seen as a proof of concept.

6.2 Cell Fabrication

Two electrode coin cells were used to obtain the majority of data in this chapter. Cells were constructed as described in Section 2.5.2.1 with $LiV_{0.5}Ti_{0.5}S_2$ as the working electrode and the cathodes of choice replacing lithium metal as the counter electrode. In addition to a glass

separator a Celgard monolayer polypropylene (PP) separator is used in full cells. When two electrode materials are used in a full-cell there is often dissolution of ions into the electrolyte that can be transferred to the other electrode. As this process is usually irreversible and it 'blocks' parts of the electrode it can lead to capacity fade and irreversible capacity loss. The Celgard separators are less permeable than glass separators and this helps to eliminate transfer of electrode material from one electrode to the other. When three-electrode Swagelok cells were constructed three separators were used.

For full cells it is important to ensure that the two electrodes are balanced[4]. This can be difficult as different materials have different specific capacities. All of the full cells in this Chapter are anode limited, therefore an excess of cathode material was used to ensure that there was always sufficient lithium in the cell to intercalate into $LiV_{0.5}Ti_{0.5}S_2$ to form $Li_2V_{0.5}Ti_{0.5}S_2$. This was done as the main emphasis of this thesis has been about the performance of $LiV_{0.5}Ti_{0.5}S_2$ and it is the performance of $LiV_{0.5}Ti_{0.5}S_2$ in a full cell that is of interest. In all the cells discussed below the $LiV_{0.5}Ti_{0.5}S_2$ electrode was a cast electrode, this electrode was then weighed and a cathode electrode of the required counter weight was formed from a pellet. Pellet electrodes were used for the cathode counter as they can be made to measure more accurately than punching casted electrodes. Additionally, unlike the sulphide anode materials, the cathode materials used in this chapter do not show drastically increased capacity fade when a pellet electrode is employed.

6.3 $LiCoO_2$ as the cathode

Commercial $LiCoO_2$ powder (99.8%, Aldrich) was used to make the $LiCoO_2$ counter electrode with 10% Super S carbon and 10% Kynar binder. The $LiCoO_2$, Super S and Kynar were mixed and pressed into pellets for electrochemical testing. Figure 6.1 shows the performance of the $LiCoO_2$ electrode with a lithium counter electrode at a rate of 100 mAg^{-1}.

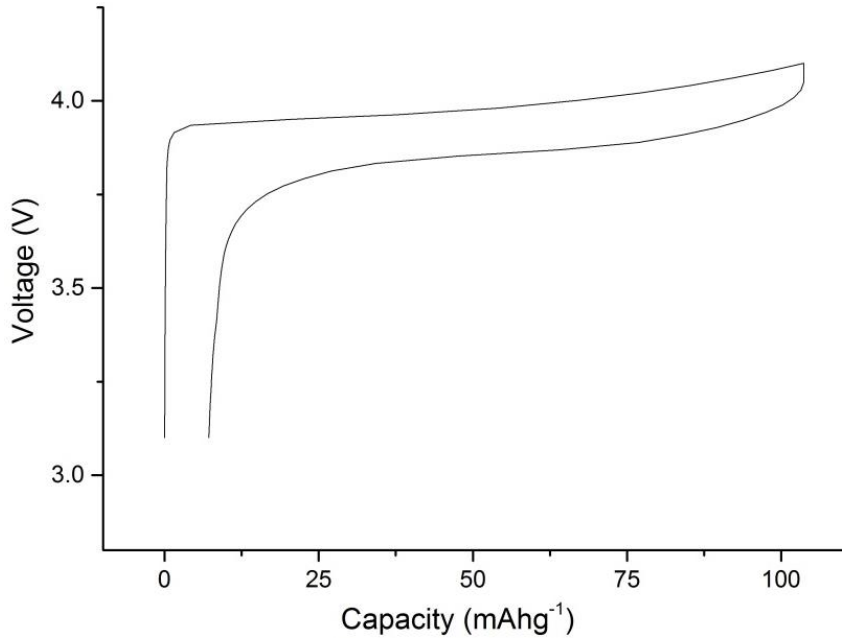

Figure 6.1: 1st cycle load curve of $LiCoO_2$ with a lithium electrode at a rate of 100 mAg^{-1}.

The commercial $LiCoO_2$ displays a reversible capacity of ~ 100 $mAhg^{-1}$, less than the literature value of 130 – 140 $mAhg^{-1}$ usually seen for $LiCoO_2$. This may be due to the relatively high rate of 100 mAg^{-1} and the use of pellet electrodes. It is important to know the specific capacity of the cathode material to make sure the two electrodes in the full cell are balanced correctly. In order to achieve the maximum capacity for the $LiV_{0.5}Ti_{0.5}S_2$ anode material there needs to be sufficient lithium in the cathode electrode to form $Li_2V_{0.5}Ti_{0.5}S_2$. There is an increase in irreversible capacity loss on the first cycle for full cells compared to half cells, see below, and this needs to be taken into account. Therefore the cells were balanced at 3.5 times $LiCoO_2$ to $LiV_{0.5}Ti_{0.5}S_2$. The 1st cycle load curve for the $LiV_{0.5}Ti_{0.5}S_2/LiCoO_2$ full cell at a rate of 100 mAg^{-1} is displayed in Figure 6.2.

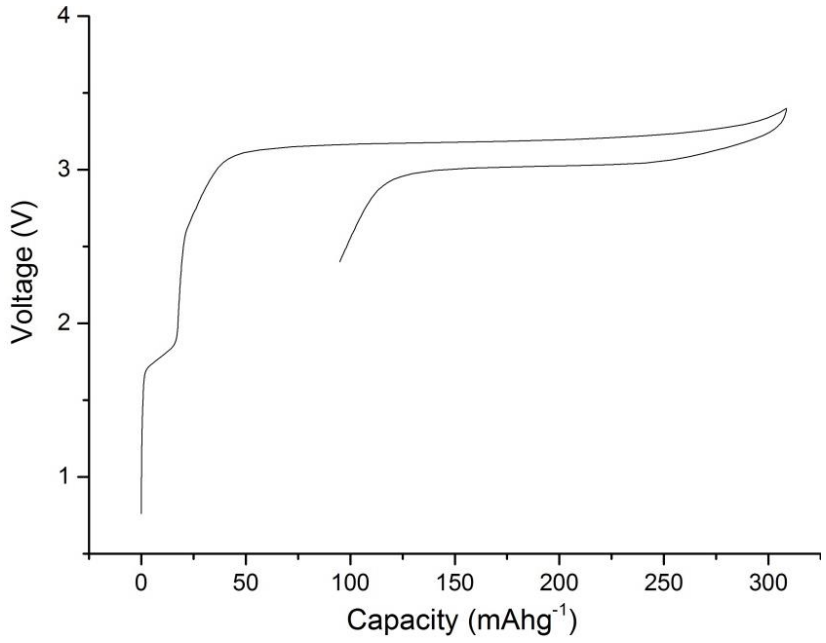

Figure 6.2: 1st cycle load curve of $LiV_{0.5}Ti_{0.5}S_2$/$LiCoO_2$ full cell at a rate of 100 mAg^{-1}.

As expected the load curve looks significantly like an inverse of the $LiV_{0.5}Ti_{0.5}S_2$ half-cell load curve seen in Chapter 4. The small plateau at ~ 1.7 V corresponds to the M^{3+}/M^{4+} redox couple associated with lithium deficient $LiV_{0.5}Ti_{0.5}S_2$ becoming stoichiometric. Lithium insertion into $LiV_{0.5}Ti_{0.5}S_2$ occurs at ~ 3.2 V and extraction takes place at ~ 3.0 V. The polarisation of ~ 0.2 V is higher than observed for $LiV_{0.5}Ti_{0.5}S_2$ half-cell due to the polarisation seen in the $LiCoO_2$ electrode (Figure 6.1). The irreversible capacity loss is ~ 75 $mAhg^{-1}$, significantly higher than the 42 $mAhg^{-1}$ seen in the half-cells seen in Chapter 4. This could be partly due to the fact that in a full-cell it is difficult to know the potential at which the individual electrodes operate, as only an average of the two is observed. Therefore, the $LiV_{0.5}Ti_{0.5}S_2$ anode could be occupying a lower voltage than previously seen; this would lead to increased electrolyte decomposition and irreversible capacity loss. Optimisation of the voltage cut-offs used could help to alleviate this effect.

Figure 6.3 below shows the charge and discharge capacities of the $LiV_{0.5}Ti_{0.5}S_2$/$LiCoO_2$ full-cell at a rate of 100 mAg^{-1} over the first 10 cycles.

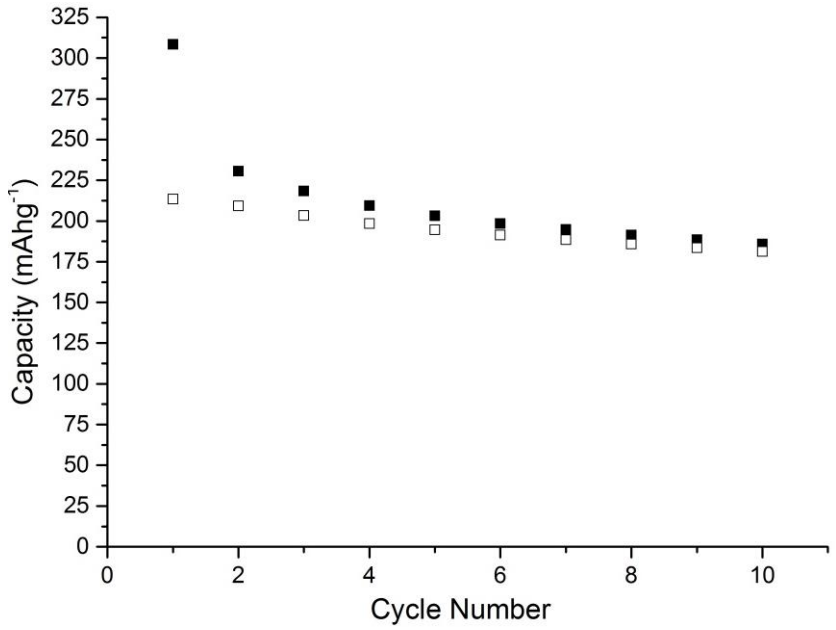

Figure 6.3: Variation of capacity with cycle number for $LiV_{0.5}Ti_{0.5}S_2/LiCoO_2$ full-cell at a rate of 100 mAg^{-1}. Closed squares correspond to intercalation and open squares to deintercalation.

The first cycle displays a discharge capacity is 215 $mAhg^{-1}$, very close the theoretical capacity of 220 $mAhg^{-1}$. However, there is significant capacity fade over the first 10 cycles and the capacity is reduced to 180 $mAhg^{-1}$. This capacity fade is more severe than seen for $LiV_{0.5}Ti_{0.5}S_2$ half-cells. This could be due increased SEI layer build up as discussed above or due to capacity fade in the cathode resulting in insufficient lithium being present in the system.

Three-electrode Swagelok cells were constructed to observe the $LiV_{0.5}Ti_{0.5}S_2$ anode and $LiCoO_2$ cathode relative to lithium simultaneously. Unfortunately, the performance of the Swagelok cells was considerably worse than the performance of coin cells, making it difficult to infer much information from the three-electrode systems. Figure 6.4 shows the first two cycles of the three electrode system cycled at 20 mAg^{-1}, cell performance drops considerably after two cycles. Cycling at a higher rate than the 20 mAg^{-1} seen in Figure 6.4 was found to lead to the cell failing on the first cycle.

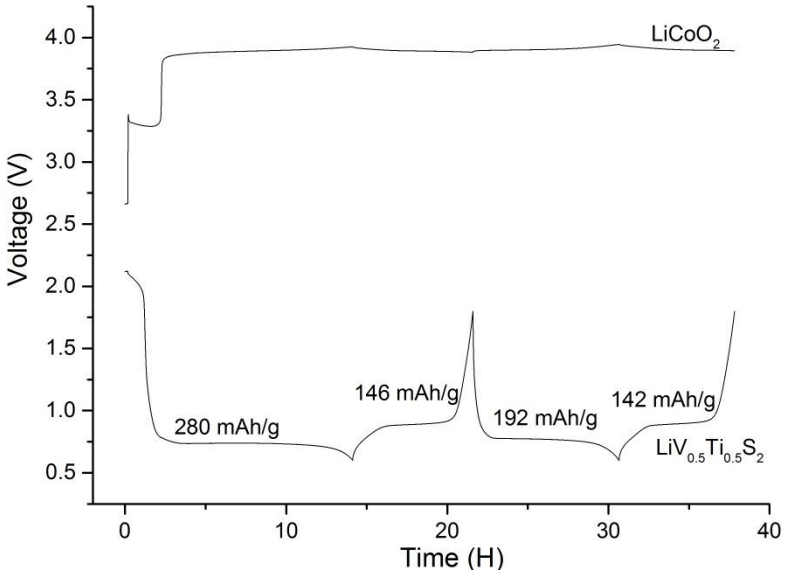

Figure 6.4: Load curves of $LiV_{0.5}Ti_{0.5}S_2$ and $LiCoO_2$ in a three electrode system cycled at a rate of 20 mAg^{-1}.

The three electrode data shows lower capacities and larger irreversible capacities than seen in traditional two electrode coin cells. The large irreversible capacity losses on both 1st and 2nd cycles indicate large amounts of SEI layer formation/electrolyte decomposition. In the cycling programme for the three electrode cells the $LiV_{0.5}Ti_{0.5}S_2$ anode was cycled between 1.8 V and 0.6 V, while the $LiCoO_2$ cathode was allowed to react freely. It can be seen that the $LiCoO_2$ electrode cycles at a steady 3.9 V, implying, for the first two cycles at least, a lack of lithium in the system is not responsible for the lower capacities. The low capacities could be due to the reduced stack pressure in Swagelok cells as opposed to a coin cell. If the stack pressure is not high enough than parts of the electrodes are not in contact with either the current collector or electrolyte soaked separator and there is a reduction in lithium intercalation or deintercalation. Alternatively, it is possible that, despite the use of multiple separators, there is transfer of $LiCoO_2$ from the cathode electrode to the anode and this blocks areas of the electrode and stops deintercalation of lithium, therefore reducing the capacity and leading to the cell failing after 2 cycles. The voltage of $LiCoO_2$ also implies that the upper voltage cut off of 3.4 V, used in Figures 6.2 and 6.3, is at least roughly correct, but further testing will be required to confirm

the exact optimum cycling voltage. Regrettably, as the three electrode cell fails after 2 cycles it does not give any information in to the cause of the capacity fade seen in Figure 6.3.

The data above demonstrate that the $LiV_{0.5}Ti_{0.5}S_2$ anode can be used with a $LiCoO_2$ cathode to form a full-cell; however, further optimisation needs to be carried out to improve performance to a satisfactory level.

6.4 Lithium-rich mixed metal oxide as the cathode

This section will use the RF-gel synthesised lithium-rich mixed metal oxides discussed in Chapter 5 as the cathode electrode in full-cells with $LiV_{0.5}Ti_{0.5}S_2$. This will begin with the nickel, manganese containing $0.5Li_2MnO_3{:}0.5LiNi_{0.5}Mn_{0.5}O_2$ before considering the nickel, manganese, cobalt containing $0.6Li_2MnO_3{:}0.4Li(Ni_{1/3}Mn_{1/3}Co_{1/3})O_2$.

6.4.1 $0.5Li_2MnO_3{:}0.5LiNi_{0.5}Mn_{0.5}O_2$ (LMR-NMO)

It was seen in Chapter 5 that RF-gel synthesised LMR-NMO produces a capacity of ~200 $mAhg^{-1}$. However, it was also demonstrated that it could take several cycles, especially for pellet electrodes (as were used here), to reach this capacity. Additionally, the material shows a large irreversible capacity loss on the first cycle. These factors make cell balancing difficult, ultimately 2.5 times more (by mass) LMR-NMO was used compared to $LiV_{0.5}Ti_{0.5}S_2$. This was to guarantee there was sufficient lithium in the system to form $Li_2V_{0.5}Ti_{0.5}S_2$ and it may be possible to reduce this amount in the future.

Figure 6.5 shows the 1st, 2nd and 10th load curves of the $LiV_{0.5}Ti_{0.5}S_2$/LMR-NMO full-cell at a rate of 30 mAg^{-1}, the general shape was unchanged at higher rates. Cells were cycled between 4.2 V and 1.4 V. The use of a large voltage window was necessary as the electrochemical processes of LMR-NMO occur over a large voltage range, see differential capacity plots in Chapter 5.

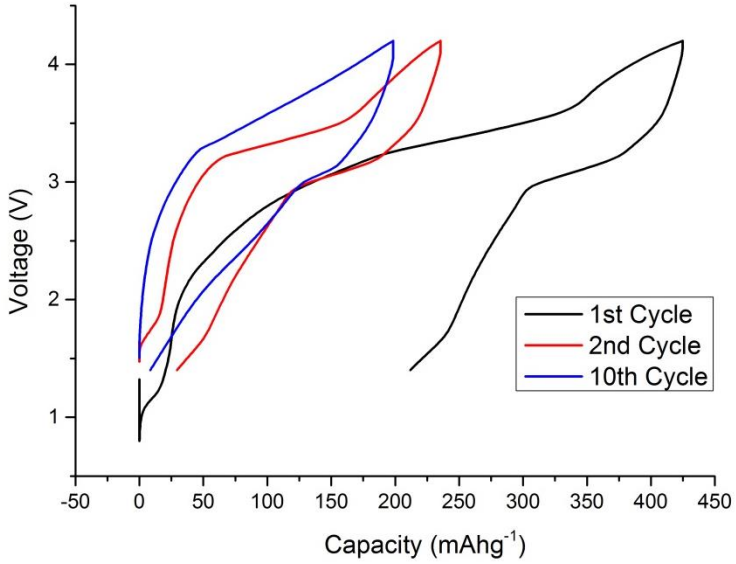

Figure 6.5: Load curves for $LiV_{0.5}Ti_{0.5}S_2$/ LMR-NMO full-cell at a rate of 30 mAg^{-1}.

There is clearly a very large irreversible capacity loss on the first cycle, over 200 $mAhg^{-1}$ compared to ~ 40 $mAhg^{-1}$ seen in $LiV_{0.5}Ti_{0.5}S_2$ half-cells. It is probable that at least some of this difference is due the oxygen loss at the LMR-NMO cathode discussed in Chapter 5, but there may also be a contribution from extra SEI layer formation on the $LiV_{0.5}Ti_{0.5}S_2$ anode due to cycling in a larger voltage window. The $LiV_{0.5}Ti_{0.5}S_2$ half-cells seen in Chapter 4 were cycled in a voltage window of 1.2 V (1.8 – 0.6 V), however, here they are cycled over a much large potential of 2.8 V; therefore the anode may be operating at lower voltages. The pseudo-plateau above 3.5 V on the first charge could possibly be due to the anode operating at lower voltages; however, it could also be due to the high-voltage oxygen loss cathode process, lowering the upper cut-off leads to a considerable reduction in capacity. Given the large voltage window it is somewhat surprising that the $LiV_{0.5}Ti_{0.5}S_2$ cycles as well as it does and that there is no obvious contribution from the high voltage M^{2+}/M^{3+} process. On the first two cycles the charge curve is split into two regions that could correspond to the two regions seen for LMR-NMO in Chapter 5. By cycle 10 the two plateaus have become one pseudo-plateau, mimicking the appearance of LMR-NMO half-cells. It initially appears that unlike LMR-NMO half-cells where voltage fade is observed, over the first 10 cycles $LiV_{0.5}Ti_{0.5}S_2$/LMR-NMO full-cells show the charge process

moving to higher voltages. However, on closer inspection this appears to be due to an increase in polarisation.

It was hoped that the use of three electrode cells could give more information on these issues but unfortunately all three electrode Swagelok cells with lithium-rich cathode materials failed on the first discharge even at low rates. It is possible that the low stack pressure seen in Swagelok cells combined with the large structural change that occurs on the first charge in lithium-rich materials leads to a loss of contact between the electrode and current collector.

Figure 6.6 presents the charge and discharge capacities of the $LiV_{0.5}Ti_{0.5}S_2$/LMR-NMO full-cell at 30 mAg^{-1} and 100 mAg^{-1}.

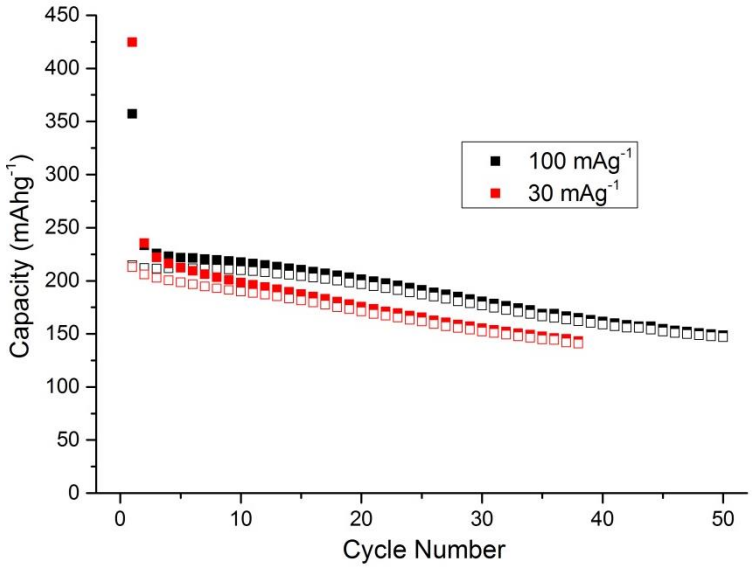

Figure 6.6: Variation of capacity with cycle number for $LiV_{0.5}Ti_{0.5}S_2$/LMR-NMO full-cells at various rates. Closed squares correspond to intercalation and open squares to deintercalation.

At 30 mAg^{-1} there is an initial reversible capacity of ~ 210 $mAhg^{-1}$ and a first cycle irreversible capacity loss of nearly 220 $mAhg^{-1}$. The reversible capacity is then subject to constant capacity fade. At 100 mAg^{-1} there is an initial reversible capacity of ~ 215 $mAhg^{-1}$, very close to the theoretical capacity of $LiV_{0.5}Ti_{0.5}S_2$, and a first cycle irreversible capacity loss of 150 $mAhg^{-1}$. The reversible capacity is steady for 15 cycles before steady capacity fade begins. As observed in previous chapters there is a reduction in irreversible capacity loss on increasing the rate of

intercalation/deintercalation. Over the first couple of cycles both rates display a discharge of 215 $mAhg^{-1}$ but at the slow rate of 30 mAg^{-1} there is more significant capacity loss compared to 100 mAg^{-1}, this is similar to the performance of $LiV_{0.5}Ti_{0.5}S_2$ half-cells seen in Figure 4.14. The explanation for this is the same as seen previous, increased SEI layer formation at slow rates due to spending more time at low and high voltages. The capacity fade at 100 mAg^{-1} is reduced compared to the fade observed in Figure 6.3 with a $LiCoO_2$ cathode possibly indicating that the $LiV_{0.5}Ti_{0.5}S_2$ anode is not operating at such a low potential and not subject to as much SEI layer formation on the electrode surface.

6.4.2 $0.6Li_2MnO_3:0.4Li(Ni_{1/3}Mn_{1/3}Co_{1/3})O_2$ (LMR-NMCO)

Data in Chapter 5 showed that LMR-NMCO performs similarly to LMR-NMO but with a slightly higher specific capacity, therefore, the same ratio of cathode material to anode material (2.5:1) was used. The same cycling window of 4.2 V – 1.4 V was also used. Figure 6.7 displays 1st, 2nd and 10th load curves of the $LiV_{0.5}Ti_{0.5}S_2$/LMR-NMCO full-cell at a rate of 30 mAg^{-1}.

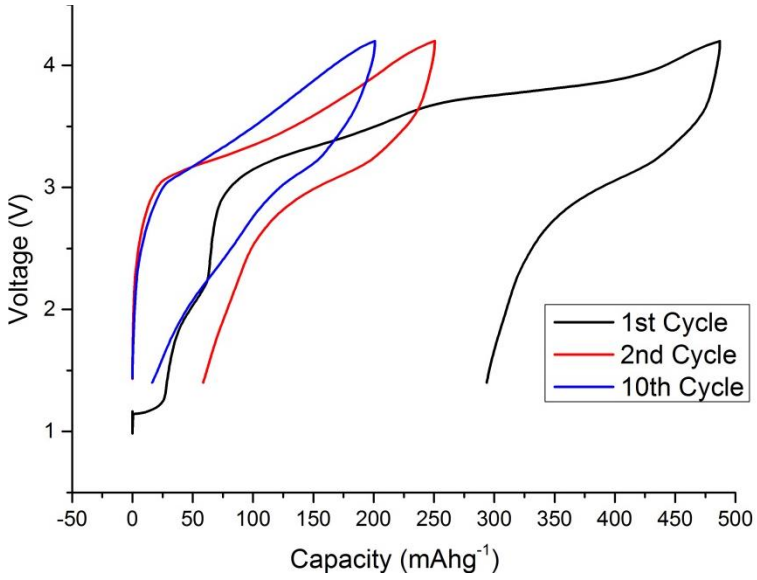

Figure 6.7: Load curves for $LiV_{0.5}Ti_{0.5}S_2$/ LMR-NMCO full-cell at a rate of 30 mAg^{-1}.

The 1st cycle load curve very closely resembles that of a LMR-NMCO half-cell but at a reduced voltage, due to the use of the sulphide anode counter as opposed to lithium metal, and with an increased irreversible capacity loss. This differs slightly to the LMR-NMO full-cell seen above,

where the first cycle seemed to resemble more an inverted $LiV_{0.5}Ti_{0.5}S_2$ load curve. By the 10th cycle load curves for both full-cells appear very similar. As seen for the LMR-NMO full-cell data there is an increase in the voltage of intercalation of lithium in to $LiV_{0.5}Ti_{0.5}S_2$ on cycling due to an increase in polarisation. Without three electrode cell data it is impossible to tell if this is due to a change at the cathode or anode. The irreversible capacity loss is larger here than in the LMR-NMO full-cell, the more pronounced high voltage plateau seen for the LMR-NMCO cell implies this could be due to an increase in oxygen loss during the cathode rearrangement process. The charge capacity for the second cycle is almost 250 mAhg^{-1}; this is more than the theoretical of $LiV_{0.5}Ti_{0.5}S_2$ and shows that the irreversible process continues to some degree after the first cycle.

The variation of capacity with cycle number for the $LiV_{0.5}Ti_{0.5}S_2$/LMR-NMCO full-cell at 30 mAg^{-1} and 100 mAg^{-1} is displayed in Figure 6.8.

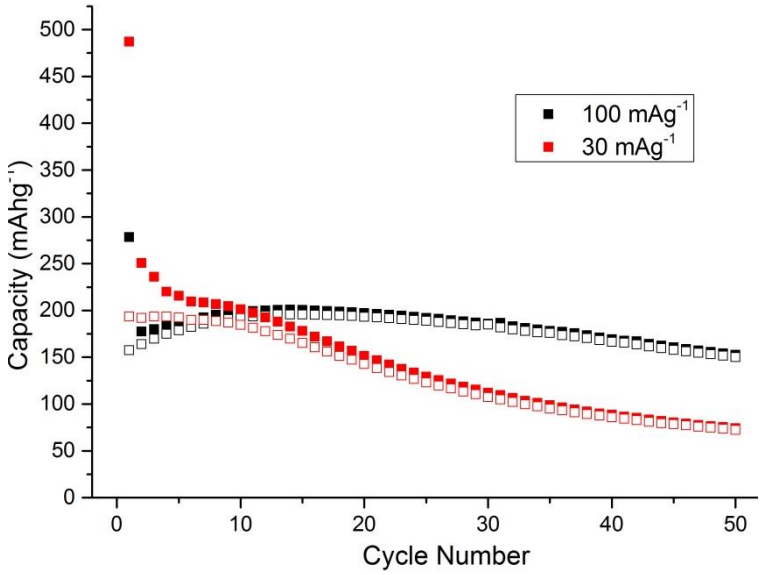

Figure 6.8: Variation of capacity with cycle number for $LiV_{0.5}Ti_{0.5}S_2$/LMR-NMCO full-cells at various rates. Closed squares correspond to intercalation and open squares to deintercalation.

At 30 mAg^{-1} there is an initial reversible capacity of ~ 200 mAhg^{-1} and a first cycle irreversible capacity loss of nearly 300 mAhg^{-1}. The reversible capacity is steady for 10 cycles but is then subject to increasing capacity fade. At 100 mAg^{-1} there is an initial reversible capacity of ~

150 $mAhg^{-1}$ and a first cycle irreversible capacity loss of 125 $mAhg^{-1}$. The reversible capacity then increases over 15 cycles to a maximum of 200 $mAhg^{-1}$, there is then steady capacity fade and the capacity is reduced back to 150 $mAhg^{-1}$ at cycle 50. As seen in the $LiV_{0.5}Ti_{0.5}S_2$/LMR-NMO full-cell in Figure 6.6, the $LiV_{0.5}Ti_{0.5}S_2$/LMR-NMCO full-cell shows increased capacity fade and a significantly larger first cycle irreversible capacity at the slow rate. The first 15 or so cycles at 30 mAg^{-1} display a poor cycling efficiency due to some form of irreversible process. Unlike the non-cobalt containing system where the maximum capacity is seen on the first cycle, it takes ~ 10 cycles for the 100 mAg^{-1} cell to reach maximum capacity. As this mirrors the behaviour of LMR-NMCO half-cells it implies that there is insufficient lithium to form $Li_2V_{0.5}Ti_{0.5}S_2$ on the initial cycles. Increasing the amount of cathode material relative to $LiV_{0.5}Ti_{0.5}S_2$ could eliminate this issue. The maximum capacity at 100 mAg^{-1} is ~ 200 $mAhg^{-1}$, less than was seen for the $LiV_{0.5}Ti_{0.5}S_2$/LMR-NMO full-cell. This could be due the fact it takes multiple cycles to reach this capacity and the formation of an SEI layer counters the increased amount of lithium in the system. Capacity fade at 100 mAg^{-1} is roughly the same as seen for the $LiV_{0.5}Ti_{0.5}S_2$/LMR-NMO full-cell, but at the slower rate of 30 mAg^{-1} the fade seen for the $LiV_{0.5}Ti_{0.5}S_2$/LMR-NMCO system is considerably worse. This is possibly due to the issue with cycling efficiency discussed above. Given the superior performance of LMR-NMCO half-cells compared to LMR-NMO half-cells seen in Chapter 5 it is surprising that LMR-NMO shows the better performance in full 'rocking-chair' battery systems with $LiV_{0.5}Ti_{0.5}S_2$.

As stated above optimisation of full-cells is not the focus of this chapter, however, one factor that has been briefly explored is the upper voltage cut-off used for the $LiV_{0.5}Ti_{0.5}S_2$/LMR-NMCO full-cell. Figure 6.9 shows cycling data for the $LiV_{0.5}Ti_{0.5}S_2$/LMR-NMCO full-cell at various voltage cut-offs at a rate of 100 mAg^{-1}.

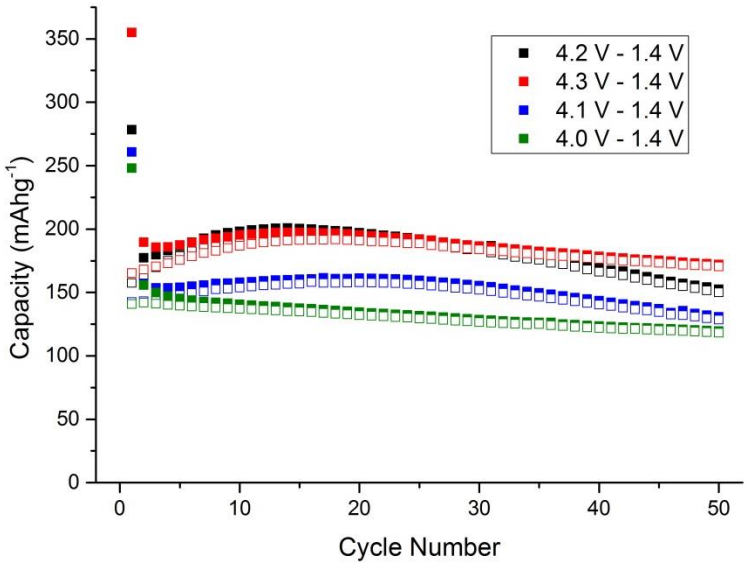

Figure 6.9: Variation of capacity with cycle number for $LiV_{0.5}Ti_{0.5}S_2$/LMR-NMCO full-cells at various voltage cut-offs at a rate of 100 mAg^{-1}. Closed squares correspond to intercalation and open squares to deintercalation.

Reducing the upper voltage cut-off to 4.1 V or 4.0 V reduces the reversible capacity of the system to ~ 150 $mAhg^{-1}$; however, it does appear to slightly improve capacity retention. The improvement in capacity retention could be due to a reduction in SEI layer formation on the surface of the anode material. Increasing the upper voltage cut off to 4.3 V leads to a significant increase in the irreversible capacity loss seen on the first cycle. This is consistent with increased electrolyte decomposition/SEI layer formation that exposing the $LiV_{0.5}Ti_{0.5}S_2$ anode to a relatively lower voltage would entail. On the whole the originally chosen voltage cut-off of 4.2 V demonstrates the best performance.

6.5 Conclusions and Future Work

It has been demonstrated that $LiV_{0.5}Ti_{0.5}S_2$ can be used as the anode in anode limited lithium-ion full cells with $LiCoO_2$, LMR-NMO and LMR-NMCO cathode materials.

$LiV_{0.5}Ti_{0.5}S_2/LiCoO_2$ full-cells produce a capacity of ~ 215 $mAhg^{-1}$, close to the theoretical capacity of $LiV_{0.5}Ti_{0.5}S_2$, though considerable capacity fade reduced this to 180 $mAhg^{-1}$ after 10 cycles. Cycling can be carried out over a small voltage window and polarisation is small.

$LiV_{0.5}Ti_{0.5}S_2$/LMR-NMO and $LiV_{0.5}Ti_{0.5}S_2$/LMR-NMCO full-cells require a large voltage window to cycle well and polarisation is relatively large, given the nature of the lithium-rich cathode materials these points are probably unavoidable. It is somewhat surprising that $LiV_{0.5}Ti_{0.5}S_2$ cycles so well when operating in such a large voltage window. Both $LiV_{0.5}Ti_{0.5}S_2$/LMR-NMO and $LiV_{0.5}Ti_{0.5}S_2$/LMR-NMCO full-cells display capacities of over 200 $mAhg^{-1}$ and capacity fade is less than seen for the $LiCoO_2$ system, but still more significant than the $LiV_{0.5}Ti_{0.5}S_2$ half-cells seen in Chapter 4. Surprisingly, the $LiV_{0.5}Ti_{0.5}S_2$/LMR-NMO full-cell performed better than the $LiV_{0.5}Ti_{0.5}S_2$/LMR-NMCO cell.

The work presented in this chapter is intended as a proof of concept and does not demonstrate the full abilities of $LiV_{0.5}Ti_{0.5}S_2$ as an anode material in full lithium-ion cells. There is significant work still to be carried out on optimisation of the systems present, for example, the voltage cut-offs used and the cell loadings. Additionally, all the work presented here was anode limited as the performance of $LiV_{0.5}Ti_{0.5}S_2$ was the primary concern, cathode limited work will be carried out in the future.

6.6 References

1 Shim, J. & Striebel, K. A. *J. Power Sources* **119**, 955-958 (2003).
2 Wu, H. M. *et al. J. Electrochem. Soc.* **156**, A1047-A1050 (2009).
3 Jansen, A. N. *et al. J. Power Sources* **81**, 902-905 (1999).
4 Xiang, H. F. *et al. J. Power Sources* **183**, 355-360 (2008).

Appendix A: XANES data for Chapter 4

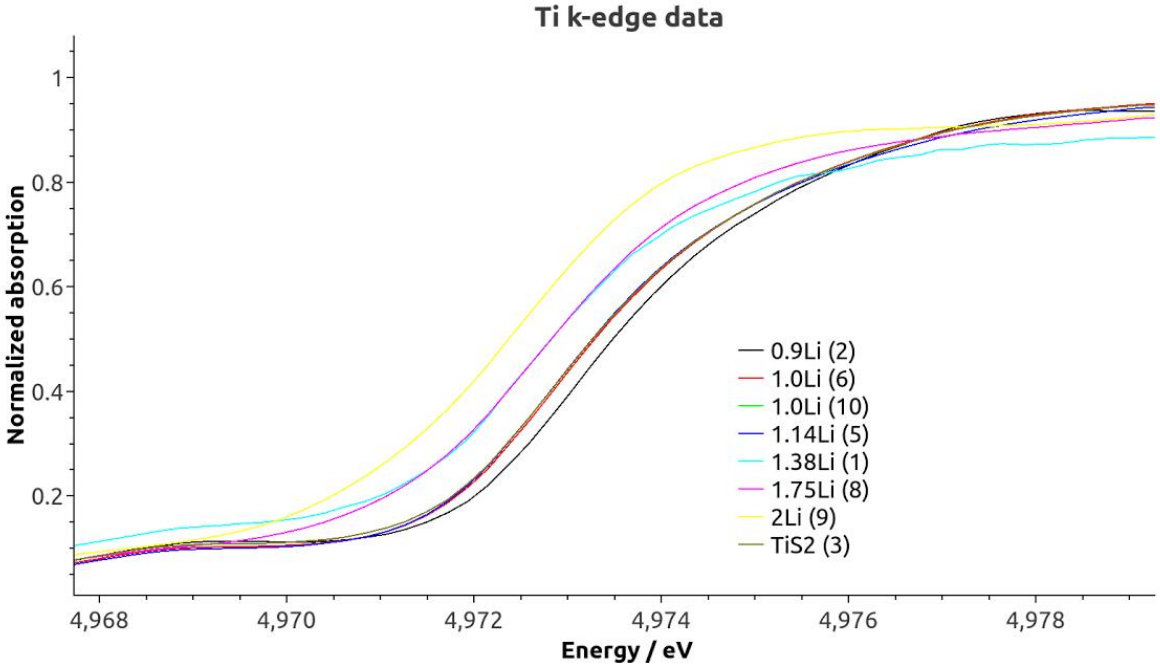

Figure A.1: K-edge XANES spectra for Ti

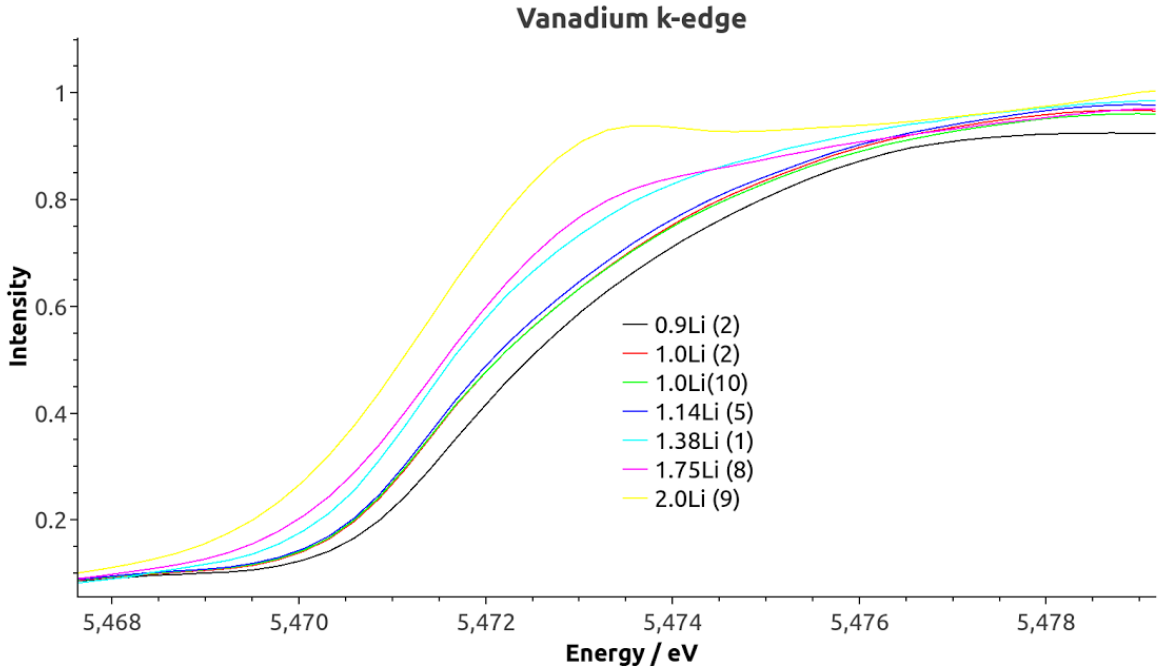

Figure A.2: K-edge XANES spectra for V

Appendix B: Neutron Refinement data for Chapter 5

Pristine Materials

LMR-NMO

LMR-NMO: Space Group		C2/m
Lattice Parameters -	**a**	4.9340(8) Å
	b	8.5711(13) Å
	c	5.0171(6) Å
	β	109.09(2)°
Refinement parameters -	R_{wp}	6.742 %
	R_{exp}	6.417 %
	R_p	7.990 %

Atom	X	Y	Z	Fractional Occupancy	B_{iso}
Li1	0	0	0.5	1	1.3(3)
Li2	0	0.667(2)	0.5	0.96(5)	1.09(14)
M1(Mn/Ni/Li)	0	0.5	0	0.33(8)/0.2/0.47	0.3(2)
M2(Mn/Ni/Li)	0	0.1715(11)	0	0.74/0.2/0.06	0.26(10)
O1	0.2168(12)	0	0.2253(13)	1	0.56(6)
O2	0.2438(8)	0.3432(3)	0.2237(5)	1	0.28(2)

Table B.1: Refinement parameters of neutron diffraction pattern for pristine LMR-NMO

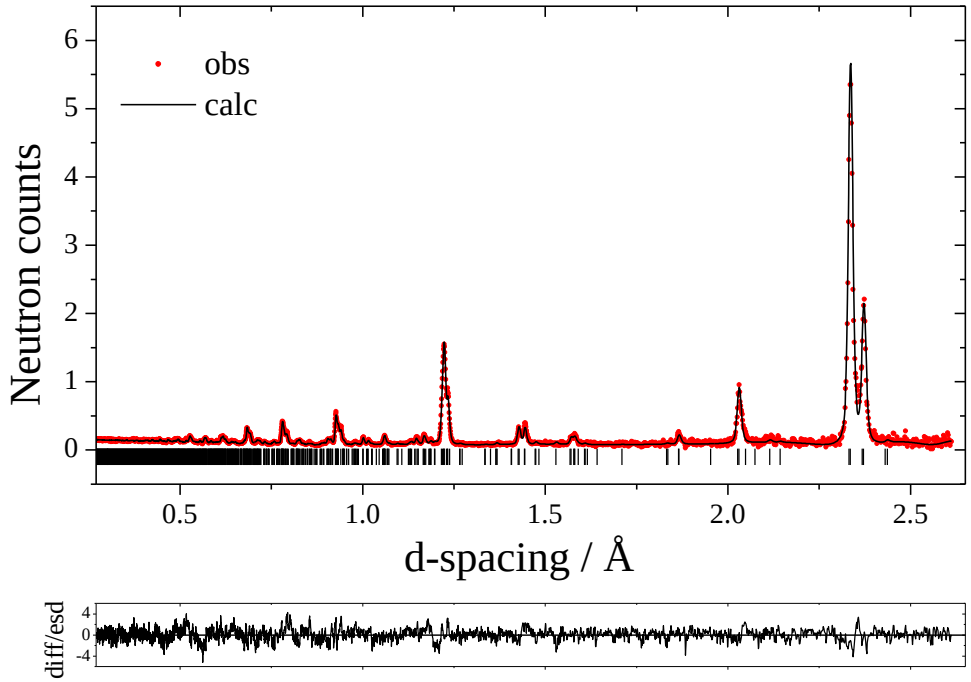

Figure B.1: Difference plot for Rietveld refinement of neutron diffraction pattern of pristine LMR-NMO

LMR-NMCO

LMR-NMCO: Space Group		C2/m
Lattice Parameters -	**a**	4.9279(8) Å
	b	8.5392(11) Å
	c	5.0078(4) Å
	β	109.00(2)°
Refinement parameters -	R_{wp}	7.478 %
	R_{exp}	8.407 %
	R_p	6.178 %

Atom	X	Y	Z	Fractional Occupancy	B_{iso}
Li1	0	0	0.5	1	0.6(3)
Li2	0	0.664(3)	0.5	0.99(3)	1.0(2)
M1(Mn/Ni/Co/Li)	0	0.5	0	0.30(7)/0.1/0.13/0.45	1.1(7)
M2(Mn/Ni/Co/Li)	0	0.1805(15)	0	0.67(3)/0.15/0.13/0.05	0.0(2)
O1	0.2214 (16)	0	0.2271(18)	1	0.63(10)
O2	0.2420(10)	0.3403(5)	0.2228(8)	1	0.41(4)

Table B.2: Refinement parameters of neutron diffraction pattern for pristine LMR-NMCO

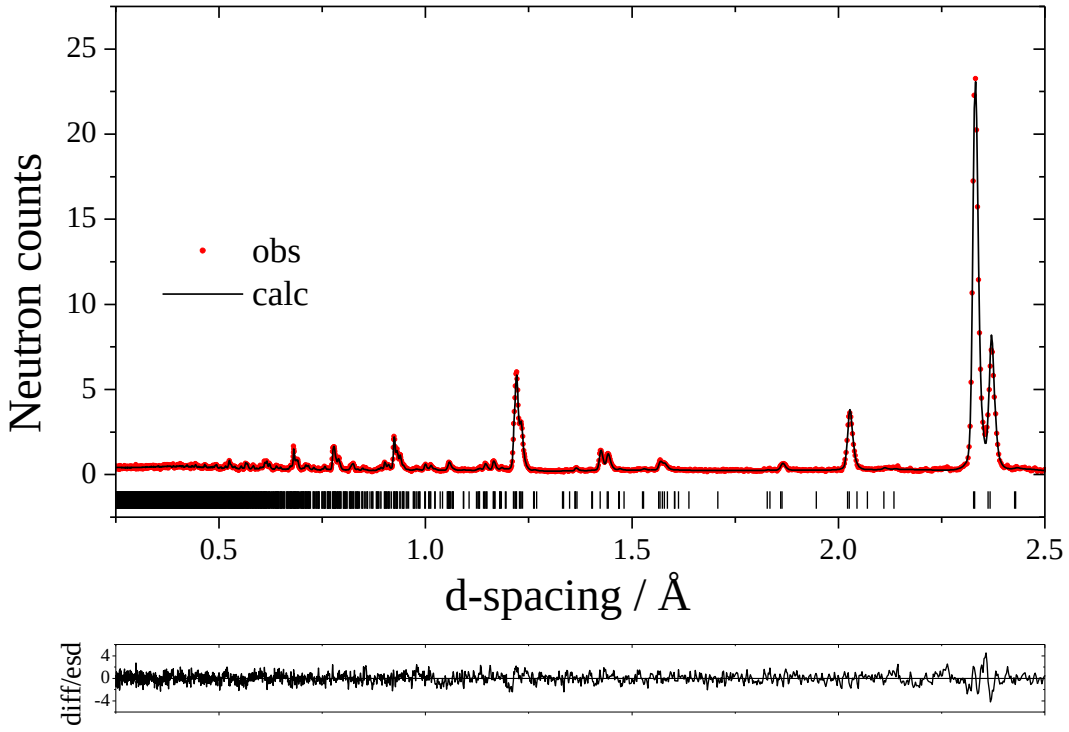

Figure B.2: Difference plot for Rietveld refinement of neutron diffraction pattern of pristine LMR-NMO

1st Cycle
LMR-NMO

LMR-NMO: Space Group		R-3m
Lattice Parameters -	**a**	2.8675(1) Å
	c	14.254(1) Å
Refinement parameters -	R_{wp}	4.077%
	R_{exp}	4.208%
	R_p	3.389%

Atom	X	Y	Z	Fractional Occupancy	B_{iso}
Li1	0	0	0.5	0.87(3)	1.9(2)
M1(Mn/Ni/Li)	0	0	0	0.715(12)/0.237(4)/0.048	0.66(11)
O1	0	0	0.2582(2)	1	0.83(2)

Table B.3: Refinement parameters of neutron diffraction pattern for LMR-NMO after 1 cycle

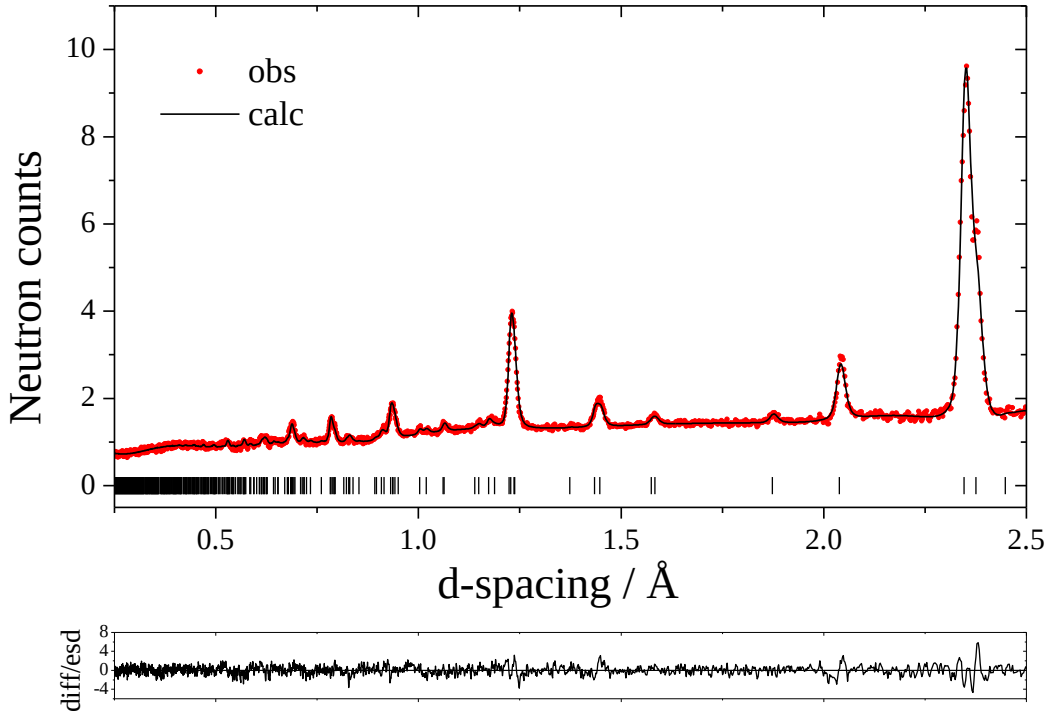

Figure B.3: Difference plot for Rietveld refinement of neutron diffraction pattern of LMR-NMO after 1 cycle

LMR-NMCO

LMR-NMCO: Space Group		R-3m
Lattice Parameters -	**a**	2.8638(1) Å
	c	14.2718 (13) Å
Refinement parameters -	R_{wp}	3.171%
	R_{exp}	3.567%
	R_p	2.627%

Atom	X	Y	Z	Fractional Occupancy	B_{iso}
Li1	0	0	0.5	0.93(2)	1.3(2)
M1(Mn/Ni/Co/Li)	0	0	0	0.67/0.12(1)/0.17/0.04	0.9(2)
O1	0	0	0.2578(2)	1	0.96(2)

Table B.4: Refinement parameters of neutron diffraction pattern for LMR-NMCO after 1 cycle

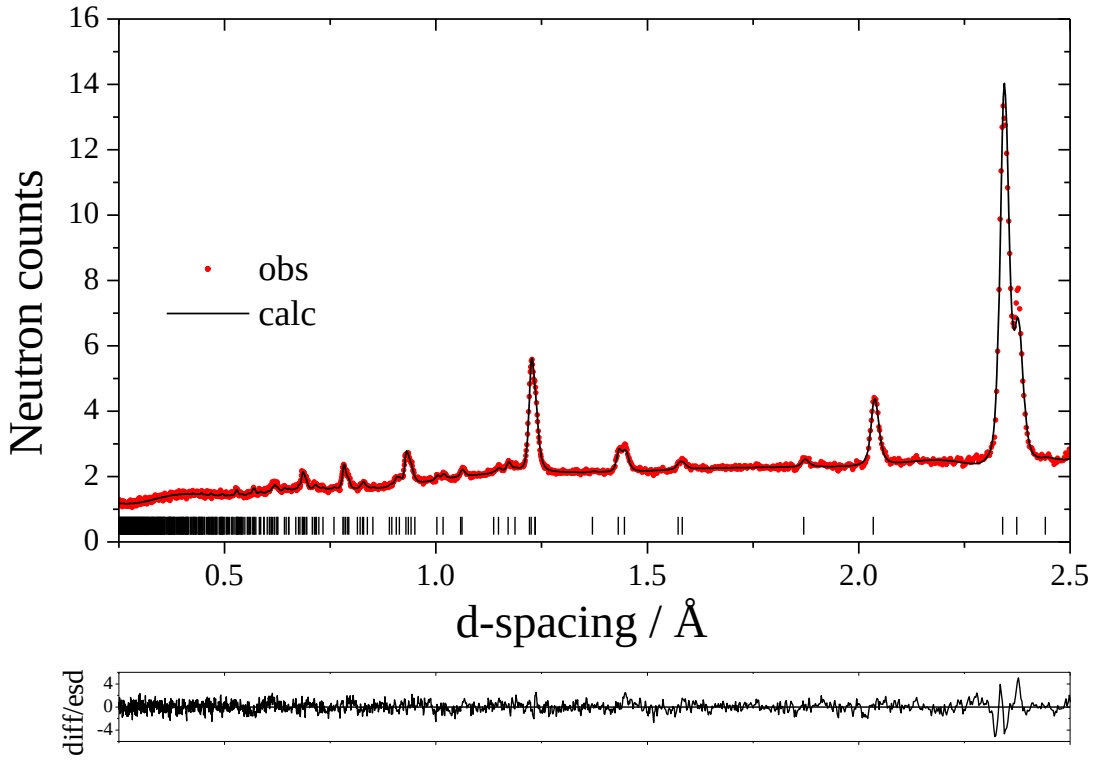

Figure B.4: Difference plot for Rietveld refinement of neutron diffraction pattern of LMR-NMCO after 1 cycle

2nd Cycle
LMR-NMO:

Phase 1 - 1st cycle like:

LMR-NMO: Space Group		R-3m
Lattice Parameters -	**a**	2.8800(3) Å
	c	14.247(3) Å
Refinement parameters -	R_{wp}	3.065%
	R_{exp}	3.86%
	R_p	2.55%

Atom	X	Y	Z	Fractional Occupancy	B_{iso}
Li1/Ni	0	0	0.5	0.95/0.05(1)	2.4(8)
M1(Mn/Ni/Li)	0	0	0	0.715(12)/0.237(4)/0.048	0.5
O1	0	0	0.2581(2)	1	1.18(6)

Table B.5: Refinement parameters of neutron diffraction pattern for LMR-NMO after 2 cycles

80% like 1st cycle: 20% like 5th cycle

Phase 2 – 5th cycle like: With only 20% of this phase, only lattice parameters can sensibly be presented.

LMR-NMO: Space Group		R-3m
Lattice Parameters -	**a**	2.8601(4) Å
	c	14.250(5) Å

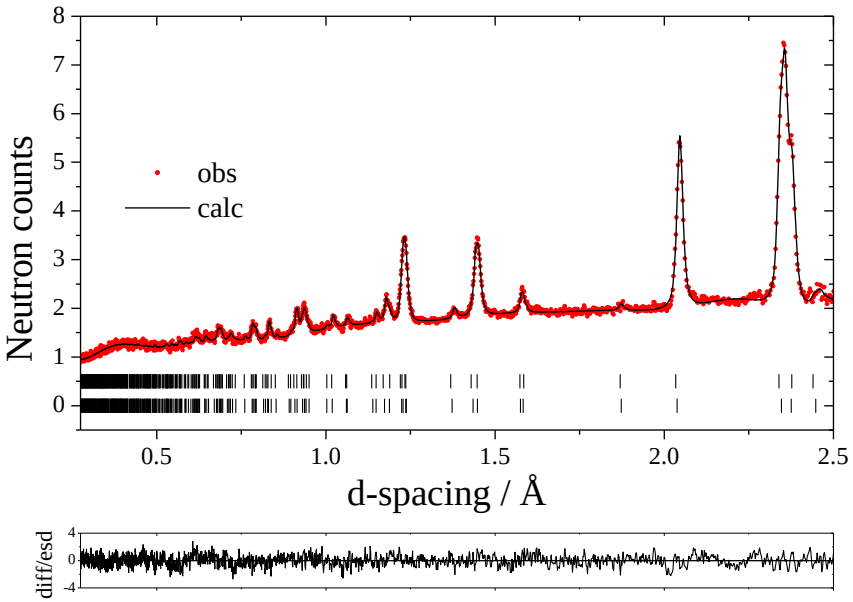

Figure B.5: Difference plot for Rietveld refinement of neutron diffraction pattern of LMR-NMO after 2 cycles

LMR-NMCO

LMR-NMCO: Space Group		R-3m
Lattice Parameters -	**a**	2.8773(3) Å
	c	14.259(4) Å
Refinement parameters -	R_{wp}	3.359 %
	R_{exp}	4.169 %
	R_p	2.810 %

Atom	X	Y	Z	Fractional Occupancy	B_{iso}
Li1	0	0	0.5	1.00(6)	2.0(4)
M1(Mn/Ni/Co/Li)	0	0	0	0.67/0.15(1)/0.17/0.01	0.5(3)
O1	0	0	0.2582(2)	1	0.95(4)

Table B.6: Refinement parameters of neutron diffraction pattern for LMR-NMCO after 2 cycles

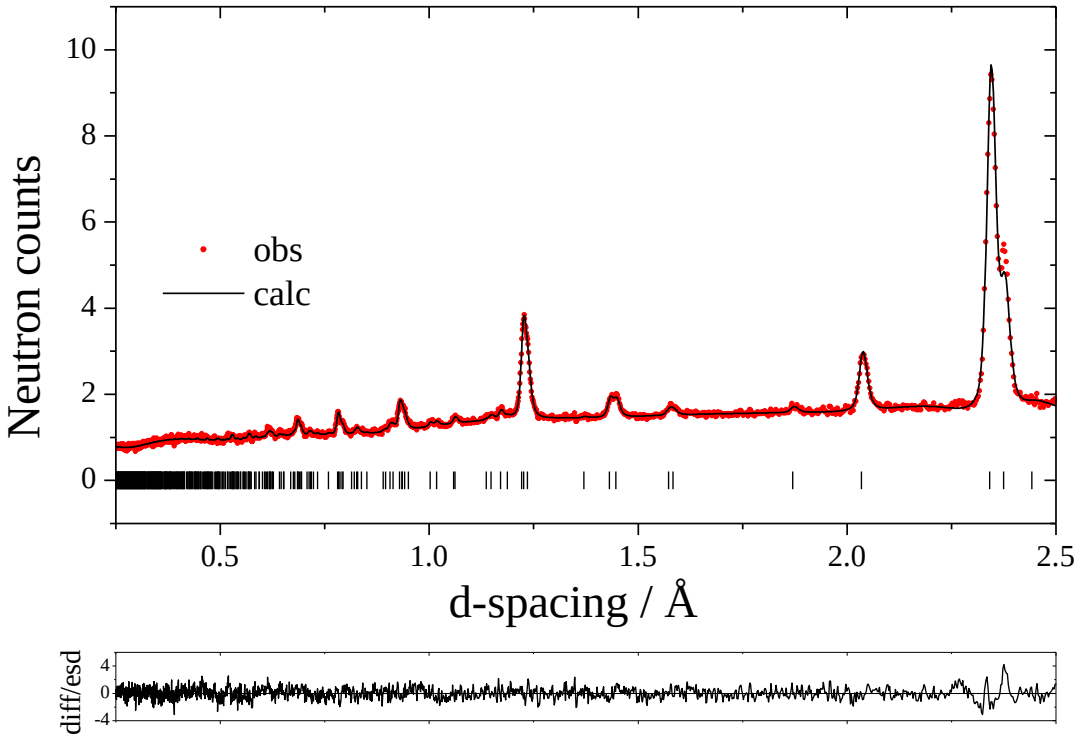

Figure B.6: Difference plot for Rietveld refinement of neutron diffraction pattern of LMR-NMCO after 2 cycles

5th Cycle
LMR-NMO

LMR-NMO: Space Group		R-3m
Lattice Parameters -	**a**	2.8592(2) Å
	c	14.261(2) Å
Refinement parameters -	R_{wp}	4.791 %
	R_{exp}	3.991 %
	R_p	4.575 %

Atom	X	Y	Z	Fractional Occupancy	B_{iso}
Li1/Ni	0	0	0.5	0.89(4)/0.012	0.7(2)
Li2	0	0	0.157(4)	0.07(2)	0.5
M1(Mn/Ni/Li)	0	0	0	0.75/0.238(5)/0.012	0.0(2)
O1	0	0	0.2588(2)	1	0.74(2)

Table B.7: Refinement parameters of neutron diffraction pattern for LMR-NMO after 5 cycles

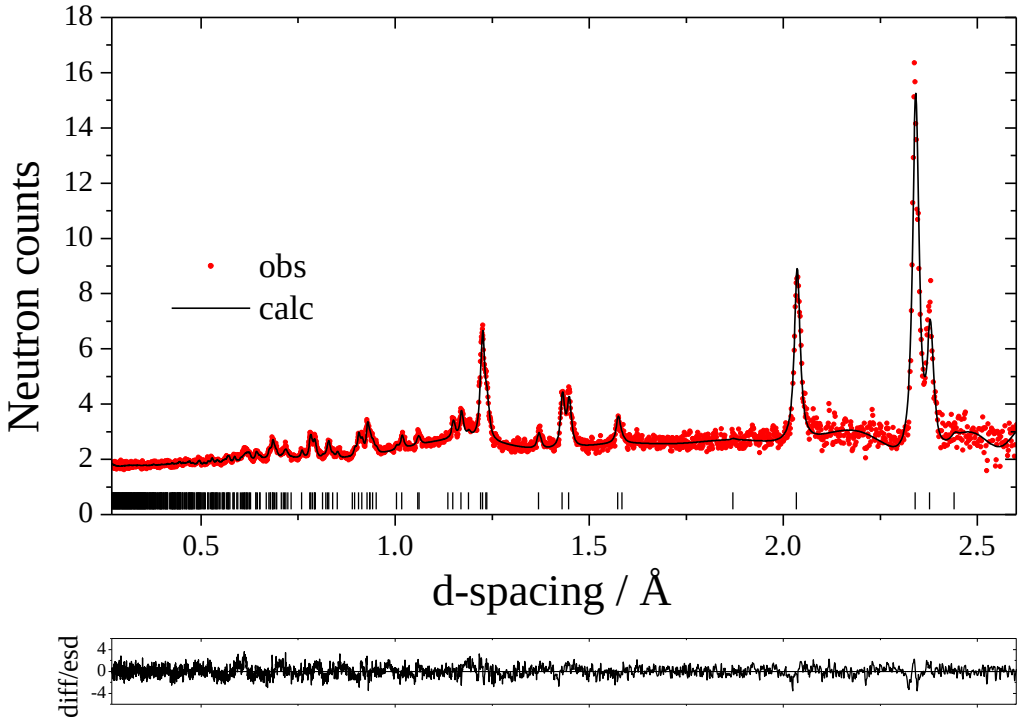

Figure B.7: Difference plot for Rietveld refinement of neutron diffraction pattern of LMR-NMO after 5 cycles

LMR-NMCO

LMR-NMO: Space Group		R-3m
Lattice Parameters -	**a**	2.8684(2) Å
	c	14.284(2) Å
Refinement parameters -	R_{wp}	3.676 %
	R_{exp}	4.163 %
	R_p	4.251 %

Atom	X	Y	Z	Fractional Occupancy	B_{iso}
Li1/Ni	0	0	0.5	0.89(3)/0.04	0.9(2)
Li2	0	0	0.151(3)	0.08(1)	0.5
M1(Mn/Ni/Co/Li)	0	0	0	0.67/0.126(5)/0.17/0.035	0.84(15)
O1	0	0	0.2593(2)	1	0.93(2)

Table B.8: Refinement parameters of neutron diffraction pattern for LMR-NMCO after 5 cycles

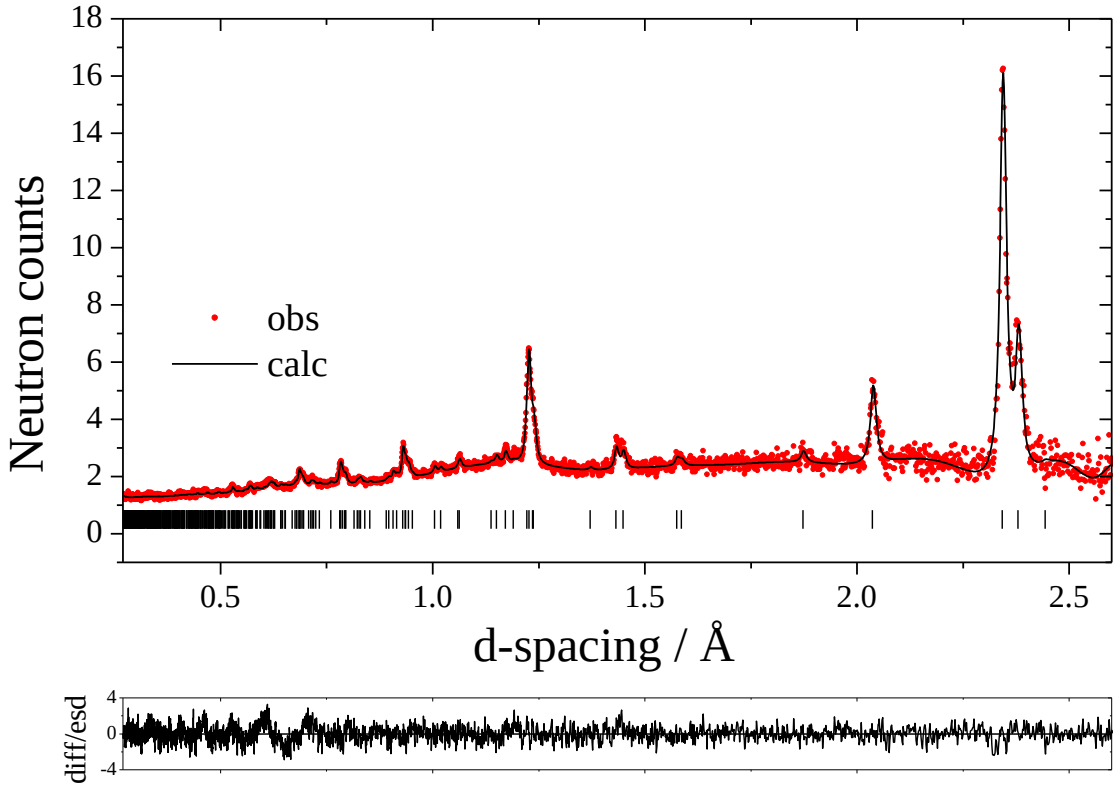

Figure B.8: Difference plot for Rietveld refinement of neutron diffraction pattern of LMR-NMCO after 5 cycles

50th Cycle
LMR-NMO

87%

LMR-NMO: Space Group		R-3m
Lattice Parameters -	**a**	2.8836(3) Å
	c	14.392(2) Å
Refinement parameters -	R_{wp}	3.11 %
	R_{exp}	3.70 %
	R_p	2.54 %

Atom	X	Y	Z	Fractional Occupancy	B_{iso}
Li1/Ni	0	0	0.5	0.89(3)/0.04	1.6(7)
Li2	0	0	0.141(10)	0.04(1)	0.5
M1(Mn/Ni)	0	0	0	0.73/0.27(1)	0.1(5)
O1	0	0	0.2589(3)	1	0.90(5)

Table B.9: Refinement parameters of neutron diffraction pattern for LMR-NMO after 50 cycles

13% spinel

a = 8.142(5) Å

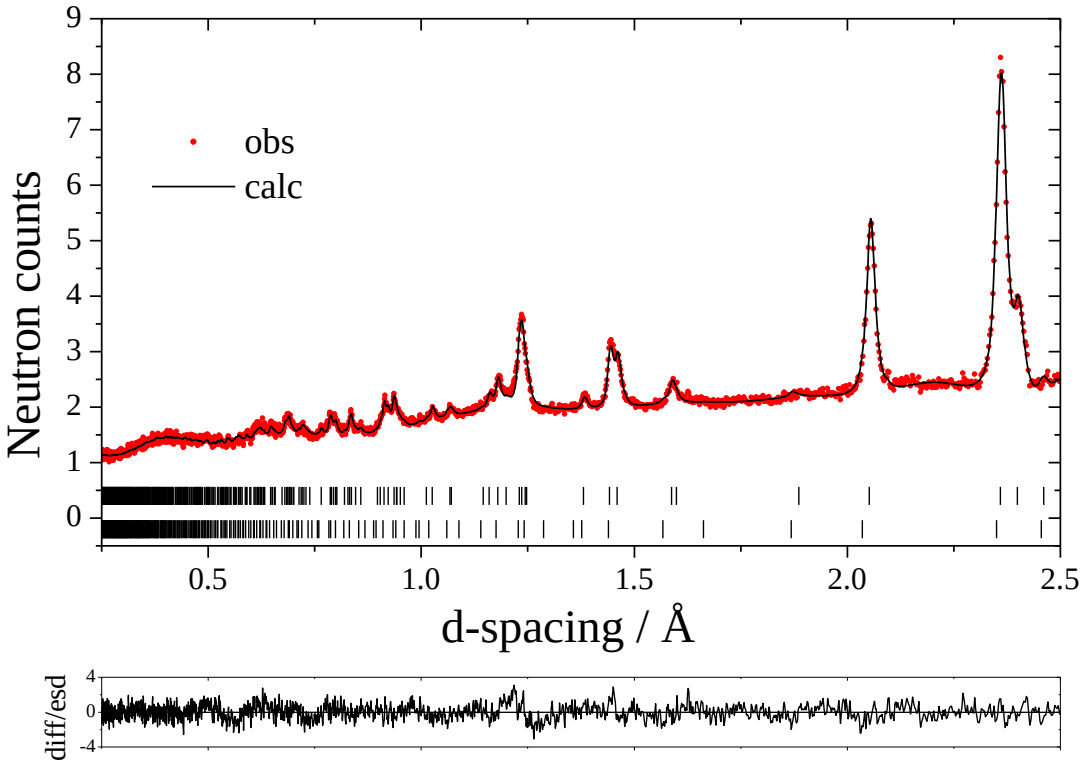

Figure B.9: Difference plot for Rietveld refinement of neutron diffraction pattern of LMR-NMO after 50 cycles

LMR-NMCO

90%

LMR-NMCO: Space Group		R-3m
Lattice Parameters -	**a**	2.8856(2) Å
	c	14.361(2) Å
Refinement parameters -	R_{wp}	2.30 %
	R_{exp}	2.60 %
	R_p	1.91 %

Atom	X	Y	Z	Fractional Occupancy	B_{iso}
Li1	0	0	0.5	0.84(8)	0.8(5)
Li2	0	0	0.141(10)	0.01(2)	0.5
M1(Mn/Ni/Co)	0	0	0	0.67/0.17/0.17	0.9(6)
O1	0	0	0.2581(3)	1	0.98(6)

Table B.10: Refinement parameters of neutron diffraction pattern for LMR-NMCO after 50 cycles

10% spinel

a = 8.053(1) Å

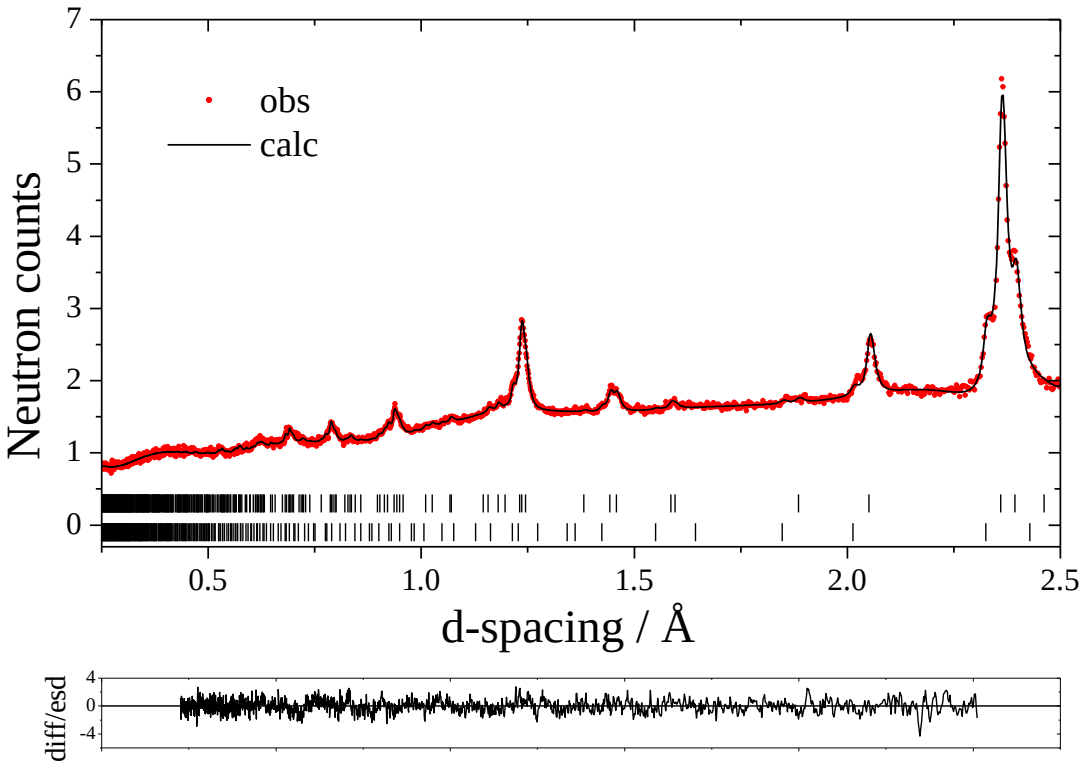

Figure B.10 Difference plot for Rietveld refinement of neutron diffraction pattern of LMR-NMO after 50 cycles